UNIVERSITY OF SOUTHAMPTON

DOCTORAL THESIS

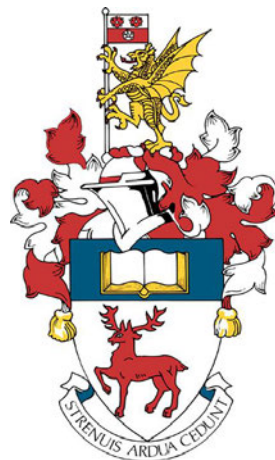# Optimisation and Power Scaling of Annular Transverse Laser Modes

by

THOMAS LEWIS JEFFERSON-BRAIN

A thesis submitted in fulfillment of the requirements
for the degree of Doctor of Philosophy

in the

Faculty of Engineering and Physical Sciences
Optoelectronics Research Centre

July 14, 2021

UNIVERSITY OF SOUTHAMPTON

Abstract

Faculty of Engineering and Physical Sciences
Optoelectronics Research Centre

Doctor of Philosophy

Optimisation and Power Scaling of Annular Transverse Laser Modes

by THOMAS LEWIS JEFFERSON-BRAIN

Laguerre-Gaussian transverse laser modes can have properties of a 'vortex' phase front that carries orbital angular momentum with each photon, or a spatially variant 'vector' polarisation state; both result in an annular intensity profile. These modes have been demonstrated to possess a range of advantages over those conventionally used in applications such as laser material processing, but generating high quality annular modes at significant output powers is difficult. To begin, vortex and vector annular modes are mathematically defined and their properties are described. Generation methods and applications of these annular modes are reviewed to date.

A radially polarised vector LG_{01} mode source and a vortex phase LG_{01} mode source were constructed using a combination of previously demonstrated techniques. These modes were optimised for modal purity for use in other experiments. The radially polarised source was measured to have a high polarisation extinction ratio of 100:1, with an output power of $5.9\,W$. The vortex mode source had an output power of $210\,mW$.

The lack of a quantified metric of beam quality suitable for higher-order transverse modes motivated the development of a convolutional neural network (named *BeamNet*) able to predict the modal composition of an intensity profile in real-time using only a camera and a computer. *BeamNet* was able to predict modal compositions in just $49\,\mu s$ per image with an error rate of 5.2% when trained on 9 possible modes. *BeamNet* was initially demonstrated as an alignment aid on a Yb:YAG laser, then used as part of an automated feedback loop to lock the otherwise variable modal composition of a Ho:YAG laser to a fundamental mode or radially polarised LG_{01} mode.

Spatially variant waveplates previously had optical losses that were too high for efficient intracavity generation of radially polarised modes. The demonstration of a refined low-loss waveplate in the cavity of a Nd:YVO$_4$ laser and the subsequent generation of a radially polarised mode is presented. The additional cavity loss of the spatially variant structure is measured as just 0.4%.

Finally, the amplification of the developed annular mode sources was explored in a thermally guiding fibre rod. This is a new hybrid amplifier architecture with excellent thermal handling and very large mode areas that shows promise for scaling the powers of annular modes. A radially polarised mode and a vortex phase LG_{01} mode are successfully amplified. The modes and their properties were well preserved after amplification, with a maximum achieved gain of $7.7\,dB$.

Contents

List of Figures

Declaration of Authorship

I, THOMAS LEWIS JEFFERSON-BRAIN, declare that this thesis titled, "Optimisation and Power Scaling of Annular Transverse Laser Modes" and the work presented in it are my own. I confirm that:

- This work was done wholly or mainly while in candidature for a research degree at this University.

- Where any part of this thesis has previously been submitted for a degree or any other qualification at this University or any other institution, this has been clearly stated.

- Where I have consulted the published work of others, this is always clearly attributed.

- Where I have quoted from the work of others, the source is always given. With the exception of such quotations, this thesis is entirely my own work.

- I have acknowledged all main sources of help.

- Where the thesis is based on work done by myself jointly with others, I have made clear exactly what was done by others and what I have contributed myself.

- Parts of this work have been published as journal papers and conference contributions listed in a publications appendix.

Signed:

_____

Date:

_____

Acknowledgements

First of all, I have endless gratitude to my parents and family. Without their constant and unwavering support and love this thesis would not exist. For my entire life they have given me everything I need to become a scientist. From the huge amount of books, dinosaur toys, magnet kits and help with my homework, to driving me to university, giving me bed and board, picking up after my mistakes and so much more besides, they deserve to be recognised as the best.

I owe my career to Dr Pearl John. I fully acknowledge her and the rest of the Light Express Roadshow as the origin of my fascination with lasers. Her passion and art is in my mind the highest motivator one could encounter for pursuing a career related to the study of light. Besides her remarkable professional dedication to light and education she is a shining beacon of a person. I am very proud to call her my friend and very thankful for all she has done for me.

My supervisors constantly astounded me with their genius, ideas, teachings and care throughout my PhD. Any student should be very happy to study under Professor Andy Clarkson, he is a veritable font of ideas and a master of virtually any topic you need to know about. It was his lecture course that inspired me to start this doctorate, and his supervision that enabled me to finish it. Dr Peter Shardlow was never my 'official' supervisor on paper, yet I would very much like to count myself as one of his doctoral students. Peter is one of those truly wonderful people that you can scarcely believe exist. I don't know how so many ideas and inventions, such care and dedication, and such fun and inspiration can come from one man. Thank you.

My friends, fellow students and colleagues were essential in getting me through the last four years, both academically and personally. Together Mark Burns and I made the important discovery of how to actually work in optics labs. I had a lot of fun working with Mark and I gained an excellent friend. Callum Smith, Robin Uren, Qiyao Liu, and Matthew Barber were a joy to work with and were always happy to give me time and teach me. Callum, your thesis was very useful as a fine example! Thank you also to the staff of the University of Southampton for their technical, pastoral and educational support. I am indebted to Simon Woods for his understanding and kind management over the last year.

Dr Azaria Coupe was a brighter light than any laser in the darkest places of the last few years. My partner, my inspiration, my undómiel.

Special thanks to BBAS for services rendered.

"All we have to decide is what to do with the time that is given us. "

J. R. R. Tolkien

Chapter 1

Introduction

Lasers have captivated the imagination of many since their inception, with the first optical laser being demonstrated by Maiman in 1960 [1]. Just four years later the concept of a laser was cemented in public knowledge, famously being featured in the 1964 James Bond movie *Goldfinger*. Since then, lasers have been used to achieve truly remarkable feats that sound like they belong in fiction; they have been used to recreate the conditions in the hearts of stars [2], cool matter to some of the lowest temperatures ever recorded [3], and detect gravitational waves from from the merging of distant black holes [4]. Lasers have become engrained in the bedrock of our technology, and perform key functions in a wide range of fields, from communication to manufacturing, and many more besides.

Many people will know of a laser as a device emitting a highly directional beam of intense light but give little thought to the transverse structure, with most depictions showing a beam of light possessing intensity that gradually decreases from a central maximum. This is the well-known fundamental Gaussian mode, but it is just one of an infinite number of possible transverse modes that a laser may operate on. Higher order transverse laser modes form geometrical patterns of nodes and antinodes similar to the modes encountered in simple harmonic motion. As a matter of opinion, building a laser and adjusting optics to see the output modal pattern shift and evolve is a very satisfying and beautiful demonstration of wave physics. Although fascinating, this is not the main motivation of this thesis.

Growing interest has been placed on a set of solutions known as Laguerre-Gaussian modes, easily recognized by their annular intensity distributions. In particular, Laguerre-Gaussian modes that have the properties of a helical phase front (vortex modes), or a spatially variant polarization state (vector modes) are in the spotlight. The spatially variant properties of these modes are valued for a diverse range of applications beyond the already impressive feats that lasers are capable of, such as: more efficient laser material processing, sub-diffraction limit microscopy, communication, microscopic manipulation, and many more as reviewed in chapter 2.

At present, Laguerre-Gaussian vortex or vector modes are difficult to generate, typically have low output power, and lack quantitative characterization methods. The overarching aims of this doctoral research project were therefore to obtain Laguerre-Gaussian modes of high quality, purity, and power, with eventual hopes

that the advances from this work would be used in laser processing. The main novel contributions of this thesis are summarised as follows:

- The development of a machine learning algorithm for real-time transverse modal composition analysis.

- The generation of Laguerre-Gaussian modes through the use of an intracavity spatially variant waveplate.

- The amplification of radially polarized and vortex phase Laguerre-Gaussian mode in a thermally guiding fibre-rod.

These contributions are fully expounded by five main chapters of content. The first of which, chapter 2, is a background chapter to providing context to the rest of the thesis. It begins with a simple model of a laser resonator that is used to derive theoretical expressions relating to the laser power and the behaviour of beams within a free-space laser cavity. Expressions for the electric fields of higher-order laser modes, including Hermite-Gaussian and Laguerre-Gaussian solutions, are derived from the scalar Helmholtz equation and used to describe the properties of interest in vortex and vector Laguerre-Gaussian modes. Formalisms of the beam radius and quality of a higher-order mode are then discussed that are important in proceeding chapters. The applications of annular modes are reviewed, highlighting important contributions to the field, followed by a review on the methods used to generate these modes so far. The background chapter ends with a discussion on the current limitations facing the development of high power annular mode sources and links to how the chapters of this thesis attempt to address these problems.

Chapter 3 reports the construction of two sources, operating on a vortex and a vector mode respectively, that were used in other experiments recorded in this thesis. These sources were constructed using tried and tested generation techniques, with some refinements, to attempt to produce annular modes of the highest possible purity from each source. The chapter first describes a 1030 *nm* Yb:YAG laser and explains how an annular pump distribution and thermally induced bifocussing were used to ensure operation on a high quality first order radially polarized mode. The second half of chapter 3 reports on the development of a 1030 *nm* Yb:YAG laser operating on a first order Hermite-Gaussian mode and how the use of dual pump spots was used in a robust configuration to achieve this. The replication of a recent experiment is then reported showing the conversion of the Hermite-Gaussian source to a first-order vortex Laguerre-Gaussian mode using a pair of spherical mirrors.

Chapter 4 is records the details and implementation of *BeamNet*, a machine learning algorithm able to make accurate predictions on the relative transverse modal composition of a given intensity profile with computation speeds three orders of magnitude faster than previous algorithms. *BeamNet* is a convolutional neural network, the the theory of which forms the beginning of Chaper 4. The training process, data and the evaluation of the performance of *BeamNet* compared to alternative

methods of modal decomposition is then discussed. This performance evaluation includes a benchmark against synthetic intensity profiles of a range of transverse modes, and real-time analysis of transverse laser modes from the radially polarized source discussed in chapter 3. The final part of chapter 4 refers to experiments performed to stabilize the transverse modal composition of a 2090 *nm* Ho:YAG laser using *BeamNet* as a diagnostic element in a feedback loop. The Ho:YAG laser demonstrated variation in the transverse mode composition with pump power without the stabilization, but by using *BeamNet* it was robustly stabilized to either a fundamental mode or a radially polarized Laguerre-Gaussian mode.

The next chapter is on the intracavity use of a refined spatially variant waveplate (S-waveplate), designed for low transmission loss, in a 1064 *nm* Nd:YVO$_4$ laser to obtain a radially polarized mode. The concept, and the fabrication by femtosecond laser writing, of the S-waveplate is briefly discussed. The experimental configuration of the Nd:YVO$_4$ laser is detailed next, where the chosen 'L' shaped configuration had two outputs in order to study the beam either side of the S-waveplate. The characterization of the outputs, one of which was a first order radially polarized mode, followed by transmission loss measurements of the S-waveplate using the Findlay-Clay method complete the chapter.

The application of a novel amplifier geometry, the thermally guiding fibre-rod, on the vortex and vector annular mode sources from chapter 3 is the subject of chapter 6. The thermal guidance model developed by C. R. Smith is adapted for higher-order modes and included in the start of the chapter. The implementation of the thermally guiding fibre-rod device using commercial Yb-doped extra large mode-area fibre is shown next. The next two-thirds of the chapter are a report and discussion of the successful amplification of a radially polarized mode and a vortex Laguerre-Gaussian mode, noting the discovered limitations and potential of the amplifier geometry.

The thesis is then concluded with a summary of the key results and suggestions for future work. As the product of four years of research, it is hoped that this work provides the field with additional tools to enable annular mode laser sources of higher quality and power. In addition, this thesis was partially written with a tutorial in mind; the aggregation of definitions, citations, and methods should prove useful to future students.

Chapter 2

Background

This chapter aims to introduce background concepts useful to understanding the operating and design principles of solid-state lasers and the annular modes that are the focus of this thesis. It also aims to collate terminology and define the transverse modes of interest according to their properties. The latest methods of generating the modes of interest and their applications are reviewed. Finally, the state of the field and the main problems that the work in this thesis attempts to address are discussed.

2.1 Fundamentals of Laser Resonators

In order to understand the design, construction and performance of lasers in general it is useful to think of a simple model of a free-space laser. This is to be considered a 'perfect' laser, and a large number of factors and effects that must be considered for real lasers are omitted for the sake of brevity. For a more detailed treatment, the reader is encouraged to consult excellent textbooks such as those by Koechner [5], Siegman [6] or Svelto [7]. Much of the content in this section is adapted from these textbooks and notes from W. A. Clarkson's lecture series [8].
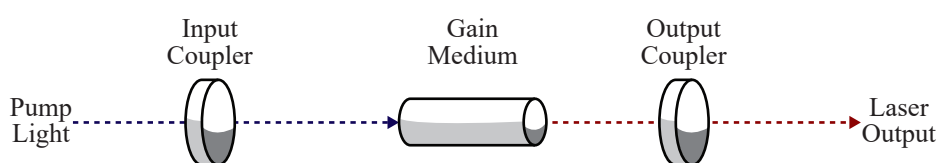
FIGURE 2.1: A simple free-space solid-state laser.

Two key processes occur in a laser resonator - feedback and amplification. Figure 2.1 is a schematic of a laser resonator with just three components: two mirrors and a gain medium. The mirrors in this example provide the feedback; light is confined between them in well defined standing wave patterns known as laser modes. Photons in the cavity may make many round-trips, and on each pass they will experience amplification in the gain medium. Energy is supplied to this gain medium through the pump; this example is end-pumped by pump light transmitted through one of the cavity mirrors that is transmissive at the pump wavelength and reflective at the lasing wavelength, denoted as the input coupler. The laser output is extracted

through the output coupler, the other cavity mirror that is partially transmissive at the lasing wavelength.

The gain medium is a material with discrete energy levels able to absorb and emit light. Another requirement is that the gain medium must have a long-lived metastable energy state that can decay by stimulated emission. Commonly used gain media can include doped crystalline and amorphous dielectrics, semiconductors, dyes and gasses to name a few. While a surprisingly wide variety of materials can be used as gain media [9], this example laser uses a rare-earth ion-doped crystal.

2.1.1 Laser Performance
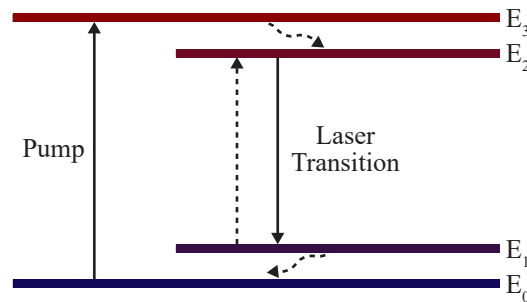
FIGURE 2.2: Energy transitions in a four-level system.

A simplified representative illustration of the energy levels of ions in the gain medium is shown in figure 2.2. We assume four discrete energy levels as indicated by E_0, E_1, E_2, E_3; this is therefore known as a four-level laser. The lowest energy level, E_0, is considered the ground state. The energy supplied from the pump light excites ions in the medium from the ground state to the E_3 energy state, a transition represented by the arrow labelled 'pump'. The majority of pumped ions quickly decay by lattice phonon emission to the upper lasing level E_2 with the difference in energy eventually being observed as heat. The transition from E_2 and E_1 is via spontaneous or stimulated emission of a photon at the lasing wavelength. Photons at the lasing wavelength may also be absorbed, promoting ions in the E_1 level to the E_2 upper lasing level. Ions in the E_1 state may return to the ground state again by phonon emission.

The four optical transitions in this process are therefore spontaneous emission, stimulated emission, pump absorption, and signal absorption. We can define ion populations at the E_i level as n_i. Calculating the rate of change of the upper laser level population density, n_2, in our simple laser resonator will allow for the derivation of an analytical model of the laser output power, threshold pump power and efficiency. We further define the transition cross-section between levels i and j as σ_{ij}, and a photon density in the gain medium as s. Assuming the population of E_3 is negligible due to the speed of decay to E_2, the rate of change of the n_2 population

density from pump absorption is represented by a pumping rate density r_p:

$$\left(\frac{dn_2}{dt}\right)_{pump} = r_p. \tag{2.1}$$

The E_2 upper lasing level has a long fluorescence lifetime, τ_f, allowing accumulation of a large ion population in this state compared to the ground level. The rate of decay per unit area through spontaneous emission from the E_2 upper lasing level to the E_1 level is therefore

$$\left(\frac{dn_2}{dt}\right)_{spont} = -\frac{n_2}{\tau_f}. \tag{2.2}$$

The ions in the E_2 level will also decay through stimulated emission to the E_1 level. This is the key process that defines lasers as having well defined phase and emission frequency. The rate of change of the upper lasing level population density due to stimulated emission is

$$\left(\frac{dn_2}{dt}\right)_{stim} = -c_n \sigma_{21} n_2 s \tag{2.3}$$

where c_n is the speed of light in the medium. Photons at the lasing wavelength present within the gain medium may also be absorbed, giving an absorption term per unit area

$$\left(\frac{dn_2}{dt}\right)_{absn} = -c_n \sigma_{12} n_1 s. \tag{2.4}$$

Combining these contributions to the rate of change of the upper lasing level population density and assuming steady state conditions, one obtains

$$\begin{aligned}
\frac{dn_2}{dt} &= \left(\frac{dn_2}{dt}\right)_{pump} + \left(\frac{dn_2}{dt}\right)_{spont} + \left(\frac{dn_2}{dt}\right)_{stim} + \left(\frac{dn_2}{dt}\right)_{absn} \\
&= r_p - \frac{n_2}{\tau_f} - c_n \sigma_{21} n_2 s - c_n \sigma_{12} n_1 s \\
&= 0.
\end{aligned} \tag{2.5}$$

In order for lasing to occur, the medium needs to have a net positive gain. Stimulated emission must dominate over absorption, and therefore n_2 must be greater than n_1, which represents the necessary population inversion. In this simple four-level laser this is easy to achieve, as the rate of decay from E_1 to E_0 is such that the population of n_1 is negligible. It should be noted that in real gain media, such as the Yb:YAG used frequently in the experiments detailed in this thesis, the conditions for population inversion are not always as trivial to achieve; the energy level diagram must be modelled as a so-called quasi-three-level system. In the quasi-three-level system the lower lasing level and ground state are close in energy in a thermally populated manifold, therefore the population in these levels is no longer negligible relative to the upper lasing level.

We can now form an additional rate equation by evaluating the rate of change of photons in the laser cavity. We make the assumption that spontaneous emission

is a negligible source of photons compared to stimulated emission, and that there is simply a sufficient number of photons initially present in the cavity for stimulated emission to begin. We also assume in our four-level system that $n_1 = 0$, therefore absorption at the lasing wavelength is negligible. The cavity photon lifetime is now defined as τ_c and is a result of the rate of change of photons in the cavity due to useful losses from the output and detrimental losses such as scattering, diffraction and and absorption. Combining the cavity photon lifetime with the rate of stimulated emission integrated over the cavity one obtains the second rate equation for the number of photons in the cavity, S, under steady state conditions.

$$\frac{dS}{dt} = \int_{cavity} c_n \sigma_{21} n_2 s \, dV - \frac{S}{\tau_c} = 0 \tag{2.6}$$

Now we define normalised pump rate density and normalised photon density as $r_0(x, y, z)$ and $s_0(x, y, z)$ respectively.

$$r_0(x, y, z) = \frac{r_p(x, y, z)}{R_p} \tag{2.7}$$

$$s_0(x, y, z) = \frac{s(x, y, z)}{S} \tag{2.8}$$

Note that integration has been performed over the volume of the cavity in arbitrary (Cartesian) coordinates here to introduce R_p as the total pump rate, and S as the total photon number:

$$R_p = \int_{cavity} r_p(x, y, z) \, dV \tag{2.9}$$

$$S = \int_{cavity} s(x, y, z) \, dV. \tag{2.10}$$

The rate equations, 2.5 and 2.6 can now be rewritten as

$$\frac{dn_2}{dt} = R_p r_0 - \frac{n_2}{\tau_f} - c_n \sigma_{21} n_2 S s_0 = 0 \tag{2.11}$$

$$\frac{dS}{dt} = \int_{cavity} n_2 c_n \sigma_{21} S s_0 \, dV - \frac{S}{\tau_c} = 0. \tag{2.12}$$

By rearranging equation 2.11 to give an expression for n_2 and substituting the result into equation 2.12 we obtain

$$\int_{cavity} \frac{c_n s_0 r_0}{1 + c_n \sigma_{21} \tau_f S s_0} \, dV = \frac{1}{R_p \sigma_{21} \tau_f \tau_c}. \tag{2.13}$$

The total pump rate, R_p, can be cast in terms of the pump power P_p, the fraction of absorbed pump power η_{abs}, the pumping quantum efficiency (the fraction of absorbed photons exciting ions to the upper laser level) η_q, Planck's constant and the

pump frequency ν_p

$$R_p = \frac{P_p \eta_{abs} \eta_q}{h\nu_p}. \tag{2.14}$$

The laser output power can also be related to the total photon number for a cavity of length l_c and output coupler of transmission T:

$$P_{out} = S h\nu_L T \left(\frac{c_n}{2l_c}\right). \tag{2.15}$$

The relations of equations 2.14 and 2.15 allow for an equation relating the pump power to the laser output power

$$\int_{cavity} \frac{s_0 r_0}{1 + \frac{2P_{out} l_c \sigma_{21} \tau_f s_0}{h\nu_L T}} \, dV = \frac{h\nu_p}{P_p \eta_{abs} \eta_q c_n \sigma_{21} \tau_f \tau_c} \tag{2.16}$$

where ν_L is the lasing frequency. This is now a generalised expression that can be used to find the pump power at which lasing begins, known as the laser threshold, and if the relationship is approximated as linear, the slope efficiency as the gradient of the laser output power with respect to the pump power. To find the threshold, we set $P_{out} = 0$ and rearrange for P_p.

$$P_{pth} = \frac{h\nu_p}{c_n \sigma_{21} \tau_f \tau_c \eta_{abs} \eta_q} \left[\int_{cavity} s_0 r_0 \, dV\right]^{-1} \tag{2.17}$$

Assuming a pump power significantly above threshold, the slope efficiency η_{sl} may be found by rearranging equation 2.16:

$$\eta_{sl} = \frac{dP_{out}}{dP_p} = \left(\frac{T c_n \tau_c}{2l_c}\right)\left(\frac{\nu_L}{\nu_p}\right) \eta_{abs} \eta_q \eta_{PL} \tag{2.18}$$

where η_{PL} is a spatially dependent pump/signal overlap factor arising from the integration of $s_0 r_0$. A useful substitution can be made for τ_c can be made to express it in terms of the measurable quantities of cavity length l_c, output coupler transmission T and excess loss L.

$$\tau_c = -\frac{2l_c}{c_n \left[\ln(1-L) + \ln(1-T)\right]} \approx \frac{2l_c}{c_n(L+T)} \tag{2.19}$$

Now the laser output power can be approximated as a linear expression of pump power, slope efficiency and threshold pump power.

$$P_{out} \approx \left(P_p - P_{pth}\right) \eta_{sl} \tag{2.20}$$

While a number of approximations have been made in this derivation, it is reasonably accurate for a well-behaved four-level laser, and more importantly it introduces key characteristics of lasers that will be measured in all of the experiments in this thesis. It also provides a valuable relation between quantities that can be used to aid in

design and optimisation of laser sources.

2.1.2   Laser Cavities

With the gain medium discussed and modelled, the next aspect of the example laser to consider is the feedback provided by the cavity mirrors. Barring advanced geometries and 'unstable' resonators from discussion for now, we require that the path the light takes through the cavity forms stable patterns that are recreated after multiple round-trips, allowing for the signal to build up inside the laser. The choice of the cavity mirrors, their alignment, and their separation are a set of variables that are therefore of key importance to the construction of a laser. The mirrors and the propagation of light in the cavity can be modelled by a simple geometric optics argument. This model was well described by Kogelnik and Li [10], with key elements replicated here.

Consider a ray propagating at a small angle to the optical axis (z). This two-dimensional ray can be described by its distance x_1 from the z axis and its positive angle to the z axis given by the derivative x_1'. After transformation by an optical element the ray will have a new position and angle x_2 and x_2'. This transformation can be represented by a matrix termed 'ABCD' such that

$$\begin{pmatrix} x_2 \\ x_2' \end{pmatrix} = \begin{pmatrix} A & B \\ C & D \end{pmatrix} \begin{pmatrix} x_1 \\ x_1' \end{pmatrix}. \tag{2.21}$$

Successive transforms of a ray in the cavity can be represented by a single matrix that is simply the result of multiplication of the 'ABCD' matrices of each element. For example, the focussing of a ray by a thin lens of focal length f followed by propagation in the z axis by a distance d is represented by the product

$$\begin{pmatrix} 1 - \frac{d}{f} & d \\ -\frac{1}{f} & 1 \end{pmatrix} = \begin{pmatrix} 1 & d \\ 0 & 1 \end{pmatrix} \begin{pmatrix} 1 & 0 \\ -\frac{1}{f} & 1 \end{pmatrix}. \tag{2.22}$$

The cavity mirrors in our example laser have a spherical surfaces with radii of curvature R_1 and R_2. The transformation applied to a ray reflecting from such a mirror is equivalent to the transformation of a thin lens with focal length $f = R/2$, less a change in direction that is neglected here. Therefore, the laser cavity can be considered to be a sequence of mirror-distance-mirror-distance, repeating n times as the ray makes n round-trips of the cavity. The total ABCD matrix of this repeated sequence of transformations is therefore

$$\begin{pmatrix} A & B \\ C & D \end{pmatrix}^n = \left[\begin{pmatrix} 1 & 0 \\ -\frac{2}{R_1} & 1 \end{pmatrix} \begin{pmatrix} 1 & d \\ 0 & 1 \end{pmatrix} \begin{pmatrix} 1 & 0 \\ -\frac{2}{R_2} & 1 \end{pmatrix} \begin{pmatrix} 1 & d \\ 0 & 1 \end{pmatrix} \right]^n. \tag{2.23}$$

This sequence is stable, such that the ray has the same position and angle after a round trip, when the trace of the total matrix obeys the inequality

$$-1 < \frac{1}{2}(A+D) < 1. \tag{2.24}$$

For the cavity round trip matrix in 2.23 this means that the laser resonator is stable when

$$0 < \left(1 - \frac{d}{R_1}\right)\left(1 - \frac{d}{R_2}\right) < 1. \tag{2.25}$$

This inequality therefore places limits on the curvature and separation of the cavity mirrors that will allow for repeated feedback through the gain medium in a stable mode. If one were to choose, say two planar mirrors, the cavity would not satisfy the inequality, as there would be no converging elements present. While a useful mathematical aid, this is not claimed to represent all scenarios and effects encountered in solid-state lasers. It will be seen in later chapters in this thesis that this formalism can be used to inform the build of a laser stable for a desired regime of operation and to model the propagation of a beam through a medium with a strong thermal lensing effect.

2.1.3 Laser Modes

So far the description of the example laser has treated the light in the cavity as a ray or a distribution of photons of density 's'. In fact, in a steady-state the light in the cavity forms optical eigenmodes that replicate after a round-trip. These eigenmodes have both longitudinal and transverse components. The transverse modes manifest as spatial electric field patterns containing nodes and anti-nodes. The longitudinal modes arise from the requirement of the field in a laser cavity to have an integer multiple of 2π round-trip phase shift. These modes are analogous to the patterns observed in, for example, a string instrument or the antique physics demonstration known as Rubens' tube [11]. Fox and Li originally modelled the modes in a laser resonator through an iterative numerical solution [12]. Boyd and Gordon [13], and Boyd and Kogelnik [14] later developed an approximate wave-based analytical solution for the modes in a cavity of spherical mirrors, which was well summarised by Kogelnik and Li in [10] together with other useful results for the theory of laser resonators. This section heavily relies on the collated mathematical descriptions in [10] and [15] and some are recanted here to aid in explaining the origin and mathematical descriptions of a selection of possible cavity modes that will be explored throughout this thesis.

We begin with the scalar Helmholtz equation. The spatial wave-like behaviour of light may be described by solving

$$\left(\nabla^2 + k^2\right)E = 0 \tag{2.26}$$

where $k = 2\pi/\lambda$ is the wavenumber and E is the complex electric field of the light. The paraxial approximation is used to create a general form of the electric field in cartesian coordinates as

$$E(x,y,z) = u(x,y,z)\exp(-ikz) \tag{2.27}$$

where $u(x,y,z)$ is a slowly varying function such that

$$\frac{\partial^2 u}{\partial z^2} \ll k^2 u, \quad \frac{\partial^2 u}{\partial z^2} \ll k\frac{\partial u}{\partial z}.$$

By using this slowly varying envelope approximation, equation 2.26 becomes

$$\frac{\partial^2 u}{\partial x} + \frac{\partial^2 u}{\partial y^2} - 2ik\frac{\partial u}{\partial z} = 0. \tag{2.28}$$

A beam-like solution has a form

$$u = \exp\left[-i\left(P + \frac{k}{2q}r^2\right)\right] \tag{2.29}$$

where $r = x^2 + y^2$, and P is a complex phase shift associated with propagation of the beam. q is known as the complex beam parameter, and it is a function of the wave curvature and amplitude. The electric field decays according to a Gaussian function with increasing distance from the z axis. A beam radius, w, can be defined as in multiple ways, but was historically defined as the distance from the axis where the amplitude falls to $1/e$ of the on-axis value. The wave-fronts have a curvature that is represented by the radius of curvature R. The complex beam parameter is therefore defined as

$$\frac{1}{q} = \frac{1}{R} - i\frac{\lambda}{\pi w^2}. \tag{2.30}$$

By substituting equation 2.29 into 2.28, one can obtain

$$\frac{dq}{dz} = 1, \quad \frac{dP}{dz} = -\frac{i}{q}. \tag{2.31}$$

Integrating the derivative of q with respect to z between two arbitrary planes q_1 and q_2 separated by a distance z gives

$$q_2 = q_1 + z. \tag{2.32}$$

The q parameter can become purely imaginary if the curvature of the beam becomes planar ($R = \infty$), this is known as the beam waist and is defined using the notation w_0 such that

$$q_0 = i\frac{\pi w_0^2}{\lambda}. \tag{2.33}$$

It is often useful to use a beam waist as a reference point, therefore we can define the evolution of the beam radius at a distance z from the beam waist by first using the

relation in 2.32 on equation 2.33

$$q = q_0 + z = i\frac{\pi w_0^2}{\lambda} + z. \tag{2.34}$$

The real and imaginary parts can be equated to obtain equations for $w(z)$ and $R(z)$ that will be used extensively in this work:

$$w^2(z) = w_0^2 \left[1 + \left(\frac{\lambda z}{\pi w_0^2} \right)^2 \right] \tag{2.35}$$

$$R(z) = z \left[1 + \left(\frac{\pi w_0^2}{\lambda z} \right)^2 \right]. \tag{2.36}$$

The final component to examine in this beam-like solution is the evolution and behaviour of P. The phase shift at a distance z from the beam waist is given by using the relation between P and q written in 2.31, on equation 2.34 and then integrating over z to obtain

$$P(z) = -i \ln \sqrt{1 + \left(\frac{\lambda z}{\pi w_0^2} \right)^2} - \arctan \left(\frac{\lambda z}{\pi w_0^2} \right). \tag{2.37}$$

The imaginary term in this expression represents an amplitude factor that can be shown to be equal to $-\ln(w_0/w)$ by rearranging equation 2.35. The real part of this expression represents the accumulated phase difference between a propagating Gaussian beam and a plane wave and is known as the Gouy phase shift. The Gouy phase shift is therefore defined as

$$\psi(z) = \arctan \left(\frac{\lambda z}{\pi w_0^2} \right) = \arctan \left(\frac{z}{z_R} \right) \tag{2.38}$$

where the Rayleigh range has been defined as z_R. Equation 2.29 can now be written in full with a scaling coefficient, C, introduced to encompass constant amplitude factors.

$$u(r,z) = \frac{1}{w(z)} C \exp \left(\frac{-r^2}{w(z)^2} \right) \exp \left(\frac{-ikr^2}{2R(z)} \right) \exp(-i\psi(z)) \tag{2.39}$$

This solution is known as the fundamental Gaussian mode, and is comprised of a single spot with maximum intensity in the centre that falls off gradually with increasing r.

2.1.4 Higher-Order Laser Modes

The fundamental Guassian mode is just one of an infinite number of solutions to the scalar Helmholtz equation. Higher-order modes can arise in a variety of sets of functions depending on the boundary conditions present in a laser cavity. For example, in a laser with favouring rectangular geometry one can use a trial solution

based in Cartesian coordinates to solve equation 2.28:

$$u(x,y,z) = g\left(\frac{x}{w}\right) h\left(\frac{y}{w}\right) \exp\left\{-i\left[P + \frac{k}{2q}\left(x^2 + y^2\right)\right]\right\} \qquad (2.40)$$

This solution is valid if

$$g \cdot h = H_m\left(\frac{\sqrt{2}x}{w}\right) H_n\left(\frac{\sqrt{2}y}{w}\right). \qquad (2.41)$$

$H_m(x)$ represents the physicists' Hermite polynomial of order m. These Hermite functions up to third order evaluate as

$$
\begin{aligned}
H_0(x) &= 1, \\
H_1(x) &= 2x, \\
H_2(x) &= 4x^2 - 2, \\
H_3(x) &= 8x^3 - 12x.
\end{aligned}
$$

Equation 2.29 can now be cast as a *Hermite-Gaussian* solution of orders n and m, as the product of these Hermite functions and the Gaussian mode:

$$
\begin{aligned}
u_{nm}^{HG}(x,y,z) =\ & \frac{1}{w(z)} C_{nm}^{HG} H_n\left(\frac{x\sqrt{2}}{w(z)}\right) H_m\left(\frac{y\sqrt{2}}{w(z)}\right) \exp\left(\frac{-(x^2+y^2)}{w(z)^2}\right) \\
& \cdot \exp\left(\frac{-ik(x^2+y^2)}{2R(z)}\right) \exp\left(-i(n+m+1)\psi(z)\right)
\end{aligned}
\qquad (2.42)
$$

The keen-eyed reader will have identified that besides the two Hermite functions, two terms in equation 2.42 are now themselves dependent on the orders n, m. The solutions have been normalised in amplitude such that $\int |u|^2 \, dx \, dy = 1$ by setting the scaling factor C to

$$C_{nm}^{HG} = \left(\frac{2}{\pi n! m!}\right)^{1/2} 2^{-(n+m)/2}. \qquad (2.43)$$

In addition, the Gouy phase shift ψ varies with n and m. By following the same approach used to obtain the expression in 2.37 but instead substituting the Hermite-Gaussian solutions we find an extra factor of $(n + m + 1)$ accompanies $\psi(z)$ in equation 2.42. This dependence of the Gouy phase shift on mode order means that transverse modes of different orders are unlikely to share longitudinal mode frequencies due to a difference in phase velocity.

The intensities, $|u_{nm}^{HG}|^2$, of the Hermite-Gaussian solutions up to third-order are shown in figure 2.3 where HG_{nm} represents the Hermite-Gaussian mode of order n, m. Rectangular symmetry is apparent in these images, and roughly, the order m corresponds to the number of x axis aligned nulls in the modal pattern, likewise with n in the y axis. When $n = m = 0$ the fundamental Gaussian solution is recovered as expected. The higher-order Hermite-Gaussian modes are often encountered

in free-space solid-state lasers targeting a fundamental mode a result of misalignment on one axis. These solutions are also often referred to as TEM_{nm} (transverse electromagnetic) modes in the literature; this nomenclature is abandoned here due to possible confusion with modal solutions derived from other symmetries that are also well described as transverse electromagnetic.

Modes deriving from cylindrical symmetry are the main topic of this work. *Laguerre-Gaussian* modal solutions to 2.28 can be found by substituting in a trial solution of the form

$$u(r, \phi, z) = g\left(\frac{r}{w}\right) \exp\left[-i\left(P + \frac{k}{2q}r^2 + l\phi\right)\right] \tag{2.44}$$

where r and ϕ are the radial and azimuthal coordinates respectively and l is a positive or negative integer representing an azimuthal order. g evaluates in this case after substitution to

$$g = \left(\frac{\sqrt{2}r}{w}\right)^l L_p^l\left(\frac{2r^2}{w^2}\right). \tag{2.45}$$

L_p^l is the associated Laguerre polynomial of order l, p, which respectively are the azimuthal and radial modal orders. L_p^l evaluates up to the third order in p to

$$
\begin{aligned}
L_0^l(x) =& 1, \\
L_1^l(x) =& -x + l + 1, \\
L_2^l(x) =& \frac{x^2}{2} - (l+2)x + \frac{(l+2)(l+1)}{2}, \\
L_3^l(x) =& \frac{-x^3}{6} + \frac{(l+3)x^2}{2} - \frac{(l+2)(l+3)x}{2} + \frac{(l+1)(l+2)(l+3)}{6}.
\end{aligned}
$$

Using the same approach as before, the Laguerre-Gaussian solutions are therefore

$$
\begin{aligned}
u_{pl}^{LG}(r, \phi, z) =& \frac{1}{w(z)} C_{pl}^{LG} \left(\frac{r\sqrt{2}}{w(z)}\right)^l L_p^l\left(\frac{2r^2}{w(z)^2}\right) \exp\left(\frac{-r^2}{w(z)^2}\right) \\
& \cdot \exp\left(\frac{-ikr^2}{2R(z)}\right) \exp\left(-i(2p+l+1)\psi(z)\right) \exp\left(-il\phi\right)
\end{aligned}
\tag{2.46}
$$

where

$$C_{pl}^{LG} = \left(\frac{2p!}{\pi (p+|l|)!}\right)^{1/2} \tag{2.47}$$

is again a normalisation constant. Important terms to note are again the mode-order varying Gouy phase shift, and an additional phase component $\exp(-il\phi)$ that represents the phase of these modes varying with the azimuthal coordinate in a vortex fashion. These solutions are shown graphically in figure 2.4. Again for $p = l = 0$ the solution reduces to the same fundamental Gaussian solution. For all other orders the modes form annular rings, with the number of null rings in the amplitude being roughly equivalent to the radial mode order p.
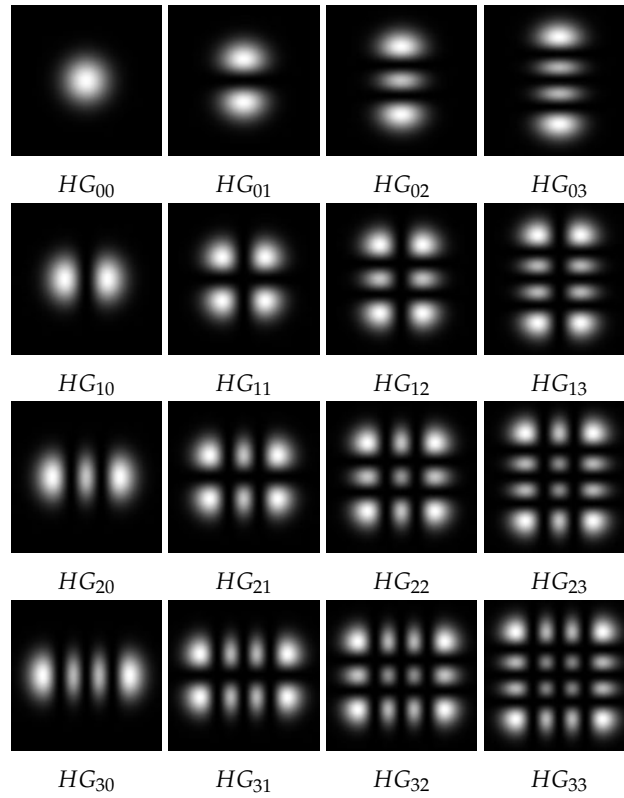
FIGURE 2.3: Hermite-Gaussian (HG_{nm}) transverse laser modes up to third-order.
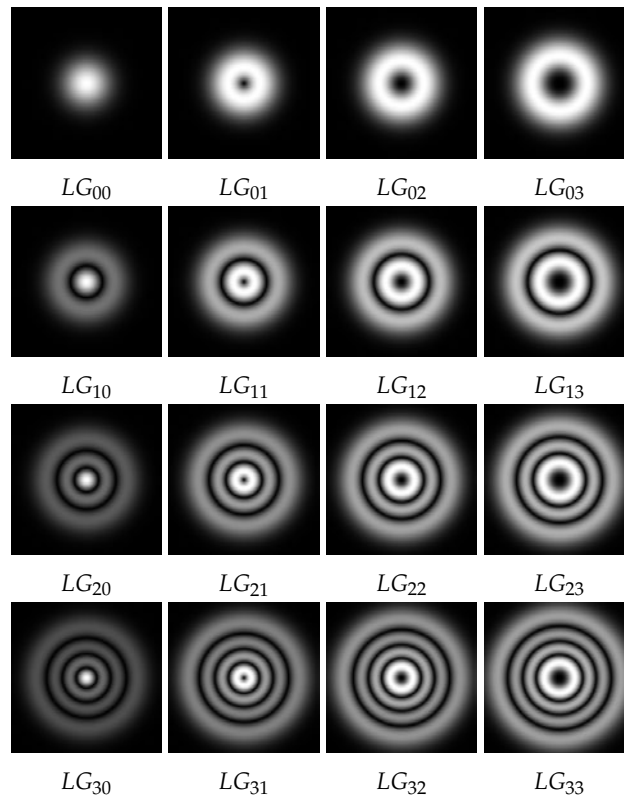
FIGURE 2.4: Laguerre-Gaussian (LG_{pl}) transverse laser modes up to third-order.

2.1.5   Beam Radius and 'Quality' of Higher-Order Modes

The images of both the Hermite and Laguerre families of Gaussian modes have all been generated with the same value of w in figures 2.3 and 2.4. This shows an important consideration to those working with these higher order modes: the mode size increases with increasing mode order. In its usage so far in this thesis, w specifically refers to the radius of the fundamental mode and its definition of the distance from the central maximum at which the intensity falls to $1/e^2$ of the maximum loses some meaning when the centre of the beam is a minimum. Siegman described an alternative in a tutorial [16] where the generalised mode radius W^2 is defined as twice the variance, found by evaluating the second moment of the beam intensity $I(x,y)$ in an arbitrary transverse axis:

$$W_x^2 = 2\sigma_x^2 = \frac{\int_{-\infty}^{\infty} \int_{-\infty}^{\infty} I(x,y)(x-\bar{x})^2 \, dx \, dy}{\int_{-\infty}^{\infty} \int_{-\infty}^{\infty} I(x,y) \, dx \, dy}. \tag{2.48}$$

Here $\bar{x}$ represents the on-axis 'centre of mass' of the intensity distribution given by

$$\bar{x} = \frac{\int_{-\infty}^{\infty} \int_{-\infty}^{\infty} I(x,y)x \, dx \, dy}{\int_{-\infty}^{\infty} \int_{-\infty}^{\infty} I(x,y) \, dx \, dy} \tag{2.49}$$

The product of the near-field waist W_0 and far-field radius $W(z)$ for this generalised beam radius is defined as

$$W_0 W(z) \approx M^2 \cdot \frac{z\lambda}{\pi}. \tag{2.50}$$

The M^2 term is known as the beam quality parameter and represents a measure of deviation from a diffraction limited fundamental mode, which has the smallest possible M^2 of 1. The radius of a higher-order mode can be represented by an 'embedded Gaussian' fundamental mode with radius $w(z)$ and the M^2 of the higher-order mode:

$$W(z) = \sqrt{M^2} \, w(z). \tag{2.51}$$

The values of M^2 for a Hermite-Gaussian mode of order m, n are given by Siegman [17] as

$$M_x^2 = 2n+1, \quad M_y^2 = 2m+1 \tag{2.52}$$

and for a Laguerre-Gaussian mode of order p, l the M^2 is

$$M_r^2 = 2p + l + 1. \tag{2.53}$$

This is a useful result for those designing lasers and optical systems operating on higher-order modes; mathematical operations can be performed using the embedded fundamental Gaussian mode radius and then adapted using the actual beam radius. For an explicit example that is used frequently in this thesis, the beam radius of a LG_{01} mode is a factor of $\sqrt{2}$ greater than the fundamental mode radius.

2.2   Vortex and Vector Modes

Due to their appearance Laguerre-Gaussian modes have been referred to in the literature as 'doughnut' or 'donut' modes, particularly referring to the LG_{01} mode which shares its shape with a ring doughnut. In this thesis the terminology 'annular' is used to describe the more generalised ring-like appearance of their intensity profiles. Modes bearing a Laguerre-Gaussian intensity profile are the main topic of study in this thesis due to their interesting properties. One possible property can be identified from equation 2.46 recalling the $\exp(-il\phi)$ phase term. This term physically manifests as a so-called 'vortex' phase; for a pure Laguerre-Gaussian mode of well defined l the phase varies azimuthally, so that a point of constant phase in the field of such a mode traces a helical vortex path when propagating in the z axis. The direction of the vortex phase rotation can take so-called left-handed or right-handed paths, therefore a pure vortex mode is often described as having a *handedness* property. The phase of a vortex LG_{01} mode is plotted in r and ϕ for constant z in figure 2.5 for a single handedness. This vortex phase is the origin for the central minimum in Laguerre-Gaussian modes with $|l| > 0$; the phase singularity results in a null in intensity. The vortex phase of these Laguerre-Gaussian modes means that
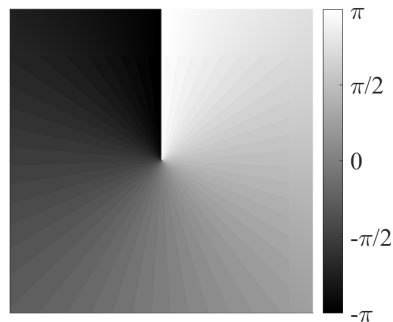
FIGURE 2.5: Phase of an LG_{01} mode at constant z

they carry orbital angular momentum (OAM) in addition to the linear momentum carried by all photons and the spin angular momentum carried by circular polarisations. For this reason the descriptor 'OAM mode' also appears frequently in the literature. Allen *et al.* [18] reasoned that higher-order Laguerre-Gaussian modes imparted an orbital angular momentum of $l\hbar$ per photon, explaining observations by Beth [19] on the torque experienced by a suspended birefringent plate or a suspended cylindrical lens. In their paper, Allen *et al.* discussed the relations between Hermite and Laguerre polynomials of general order and how Hermite-Gaussian modes could be converted to Laguerre-Gaussian modes and vice versa. Tamm and Weiss first achieved this conversion for low order Laguerre-Gaussian modes [20] before their results were reproduced and explained for arbitrary orders by Beijersbergen *et al.* [21]. As an example, an LG_{01} vortex mode can be produced by the coherent addition of a HG_{01} and a HG_{10} mode with a $\pi/2$ phase difference between the Hermite-Gaussian modes to produce the required amplitude, curvature, and the

phase:

$$u_{01}^{LG} = \frac{1}{\sqrt{2}} u_{10}^{HG} + \frac{i}{\sqrt{2}} u_{01}^{HG}. \tag{2.54}$$

This relationship is used extensively in section 3.2 of this thesis to produce vortex Laguerre-Gaussian modes. A similar relationship can be used to demonstrate that not all modes with a Laguerre-Gaussian intensity distribution possess a vortex phase and OAM, but do possess other interesting properties. For example, the coherent addition of a HG_{01} mode linearly polarised in the y axis with a HG_{10} mode linearly polarised in the x axis with no relative phase difference produces a mode with a spatially varying polarisation state aligned with the radial axis:

$$\vec{u}_r = \frac{1}{\sqrt{2}} u_{10}^{HG} \hat{x} + \frac{1}{\sqrt{2}} u_{01}^{HG} \hat{y}. \tag{2.55}$$

In equation 2.55 $\hat{x}$ and $\hat{y}$ represent the unit vectors in the x and y axes respectively. This solution is known as a first-order radially polarised mode and is an example of a set of solutions with spatially variant polarisation that can be achieved in a similar way with other combinations of Hermite-Gaussian modes and polarisation states, known collectively as cylindrical vector modes. A derivation of this solution that can be obtained by solving the full vector wave equation for the electric field can be found in [22, 15] but is not reproduced here for the purpose of brevity and clarity of definitions. A similar solution can also be obtained by combining a HG_{10} and HG_{01} mode but with the HG_{01} mode linearly polarised in the x axis and the HG_{10} in the y. This produces a mode with the intensity profile of a LG_{01} mode with spatially variant polarisation aligned with the azimuthal axis and is known as a first-order azimuthally polarised mode. A representation of the orientation of the electric field vector for first-order radial and azimuthally polarised cylindrical vector modes is shown in figure 2.6. An azimuthally polarized mode can be easily converted to a radially polarized mode or vice versa, or superposition with polarisation components of both states, through the use of a 90° optical rotator formed from two half-waveplates [23].
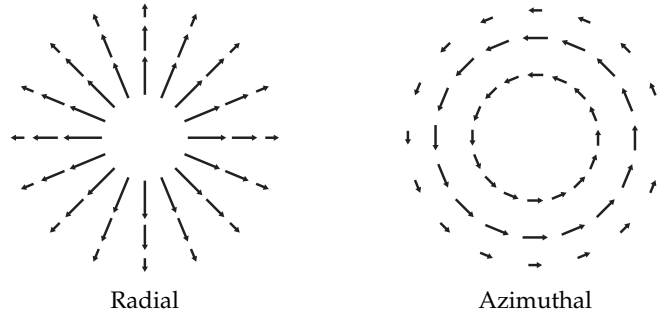
Radial   Azimuthal

FIGURE 2.6: Representative vector structure of the electric field for radially and azimuthally polarised cylindrical vector modes.

In the case of these cylindrical vector modes the central minimum is formed due to the polarisation singularity, in contrast to the phase singularity of the vortex

modes. It is worth mentioning (although beyond the scope of this thesis) that it is possible to form modes with superpositions of vortex and vector properties. These are sometimes known as Poincaré sphere beams, which were recently reviewed by Rosales-Guzmán *et al.* [24]. Equally, it is also possible to form the intensity profiles of Laguerre-Gaussian modes through the incoherent combination of Hermite-Gaussian modes so that the product has neither vortex nor vector properties. Therefore, experiments should be performed using, for example, interferometry or polarisation analysis to measure the properties of a generated mode with an annular intensity distribution.

The modes of direct interest in this thesis are the radially polarised vector LG_{01} and the vortex phase LG_{01} modes. These modes are of growing interest for a wide range of applications and there has been an increasing amount of effort dedicated by researchers to effectively generate these modes at appropriate power levels.

2.3   Applications

The spatially variant properties of vortex and vector modes have found a wealth of potential and demonstrated applications in recent years, particularly in fields such as communication, sensing, measurement, microscopy, quantum physics and manufacturing. Some results from these fields are reviewed here in order to provide a motivation for the pursuit of higher quality and higher power annular beams reported in this thesis. The applications are reported separately for annular modes with vortex and vector properties, although in some cases the intensity distribution is of interest, which is common for modes with either property in the case of the LG_{01} distribution.

2.3.1   Applications of Vortex Modes

Laguerre-Gaussian modes carrying OAM are of interest in optical communications, as discussed by Willner *et al.* [25]. Coaxially propagating vortex beams with different handedness and orders are mutually orthogonal; crosstalk between beams can therefore be minimised by an additional degree. This orthogonality means that multiple vortex modes can be effectively spatially multiplexed in combination with conventional wavelength based multiplexing. Overall, these factors were identified to potentially provide significantly increased data transmission capacity to a system. In 2018 Zhu *et al.* experimentally demonstrated an $8.4\,Tb/s$ data transmission rate over an $18\,km$ fibre [26]. They achieved this result by spatial and wavelength multiplexing of high order (LG_{p4} and LG_{p5}) vortex modes for a 224 channel low-crosstalk system. It is expected that future advances will be made through the application of vortex Laguerre-Gaussian modes to fully exploit the additional spatial dimension they provide for communication channels.

The OAM state of a vortex Laguerre-Gaussian mode also opens new applications for quantum information tasks, as reviewed by Erhard *et al.* [27]. A quantum

particle composed of a photon carrying OAM has more than just two states - it can have an additional number of states only bounded by the ability to generate arbitrarily high azimuthal orders. These additional degrees of freedom create enhanced resilience against hacking attempts and noise for use in quantum cryptography [28]. Photon pairs have been successfully produced with entangled OAM states [29]. This entanglement process has been used to transmit encrypted quantum keys via vortex modes over free space, and through atmospheric turbulence, over distances of $3\,km$ in Vienna [30] and $300\,m$ in Ottawa [31].

Vortex Laguerre-Gaussian modes have been examined for their suitability for free space propagation applications, as multiple numerical studies have indicated that these modes are particularly resilient to atmospheric turbulence and scintillation [32, 33]. However, recent experimental work returned the conclusion that a carefully selected subset of Hermite-Gaussian modes were more resilient to atmospheric turbulence than Laguerre-Gaussian modes [34], therefore this potential application remains in dispute subject to further research.

Vortex modes have demonstrated advantages in the optical trapping of particles [35]. Fundamental Gaussian modes are the norm for these trapping applications, in which transparent particles can be trapped in the central maximum of the beam due to a gradient force experienced proportional to the displacement from the centre, however absorbing particles can be scattered due to absorption. Laguerre-Gaussian modes also offer the proportional gradient force that can be used to trap particles, but the central minimum for modes with OAM greatly decreases destabilising scattering [36]. The OAM can be used to manipulate even non-birefringent particles, adding an additional tool to the repertoire of the atomic or quantum scientist. The ability of the OAM of vortex modes to exert a (small) torque has also been applied to driving micromachines [37, 38] and micropumps [39, 40]. Vortex Laguerre-Gaussian modes have also found application in particle acceleration, with some experiments noting a reduction in particle beam angles and higher maximum particle energies when compared to the use of fundamental modes [41, 42].

Other applications of vortex modes focussed on the small-scale have included imaging techniques in microscopy [43, 44]. Laguerre-Gaussian modes have been shown to allow for sub-diffraction limit resolution in combination with a fundamental Gaussian beam in stimulated emission depletion microscopy. The fundamental mode is used to excite the fluorophores in a sample. The annular intensity profile of the Laguerre-Gaussian mode is then used to deplete regions of the sample, leaving a region smaller than the diffraction limited spot size of the fundamental mode to emit by fluorescence.

OAM carrying vortex modes have found some use in metrology, as it has been reported that the backscatter of such a mode from a rotating object produces a rotational doppler shift proportional to the OAM state of the light [45]. This may mean that vortex Laguerre-Gaussian modes find use in remote rotation sensing in the future.

Finally, Laguerre-Gaussian modes have shown promise for use in laser processing and machining [46]. This application was the primary motivation for the developments recorded in this thesis. Both the intensity distribution and the OAM state are relevant properties here. The intensity minimum in the centre of the beam has been simulated to reduce the maximum stress experienced when applying lasers to glass bending processes [47]. The intensity distribution of Laguerre-Gaussian modes also has a high gradient; there is a small area of a beam that may be above a given intensity threshold. This has been modelled to be of use in materials where localised threshold intensity or temperature is preferable to a wide areas of a material close to a threshold [48]. Multiple studies on the effects of processing of silicon with pulsed Laguerre-Gaussian modes have revealed the fabrication of nano-needles inheriting some interesting helical structure from the incident vortex modes [49, 50] with needle heights of $\approx 70\,\mu m$ and $14\,\mu m$ respectively. The helicity of these nano-needles was simulated to have been caused by the rotational motion of molten material by OAM transferral from the laser pulse before the material re-solidified.

2.3.2   Applications of Vector Modes

A further property of a radially polarised vector mode is the localised longitudinal electric field component that arises under strong focussing conditions. This longitudinal component is not present in azimuthally polarized modes. This property has been widely reported on and confirmed by direct experimental measurement, for example in [51, 52, 53]. When focussed by a very high numerical aperture lens this longitudinal component can form a large contribution to the total electric field, leading to a reduction in the spot size that could be achieved by a radially polarised mode when compared to, for example, linear polarisation. A thorough review on the applications of the longitudinal field and the associated tight focussing under high NA conditions was provided by Zhan *et al.* in [15] with a recent update on the latest advances in [54]. Spot sizes as low as $0.161\lambda^2$ have been achieved for radial polarisation, whereas the spot size for linear polarisation under the same condition was 0.26λ [55].

This property has lead to radially polarised modes finding use in high resolution imaging [56, 57, 58, 59], although there have been some theoretical studies to suggest that azimuthally polarised modes could also provide comparatively high resolution imaging [60]. Image subtraction utilising illumination from both azimuthal and radially polarised modes has been shown to achieve resolutions below $100\,nm$ [61, 62]. A beam with a polarisation state with both radial and azimuthal components can be used to achieve control over sharpness and depth of field of a focus without additional complicated setups; the polarisation state can simply be tuned by rotating a waveplate pair [63, 64]. Interestingly, this flexibility in the focal point of cylindrical vector modes has been shown to allow for the precise orientation of gold nano-rods, with the ultimate goal of polarisation based encryption [65].

The manipulation of particles and optical trapping is another well studied application of cylindrical vector beams, with the intensity profile and longitudinal field under a tight focus again being key beneficial properties of radially polarised modes. The state of polarisation for optical trapping experiments has been identified as important in a number of studies [66, 67, 68, 69]. Michihata *et al.* showed that the use of a radially polarised beam enhanced trapping efficiencies in the longitudinal axis by a factor of 1.84 compared to a linearly polarised beam, however, found that the transverse efficiency was reduced by a factor of 0.58 compared to the that of a linearly polarised beam [66]. Kozawa and Sato agreed with these findings, and showed that azimuthally polarised beams exhibited a higher transverse trapping efficiency than radially polarised beams [67]. The ability to easily control the components of radial and azimuthal polarisation present in a cylindrical vector beam has also found application within optical trapping, where multiple groups have demonstrated the control of a trapping volume by varying relative polarisation components [69, 70]. A significant advantage of using radially polarised beams in optical trapping is that the dominant longitudinal component found in tight focussing does not contribute to destabilising forces in the case of metallic particles [71]. Metallic particles are usually more difficult to trap than optically transparent particles due to the strong destabilising forces arising from absorption. Radially polarised beams were used to trap gold nano-particles by Huang *et al.* [72] and were found to have a higher trapping efficiency than azimuthally or linearly polarised beams.

Metrology is another field in which cylindrical vector modes have been applied. A radially polarised beam was used by Novotny *et al.* to measure the orientation of a molecular absorption dipole moment in three dimensions [73], with the key property of use here again being the longitudinal electric field at the focal point. Another example of position sensing on the Angstrom scale was demonstrated by Neugebauer *et al.* who excited silicon nano-antennae with a tightly focussed radially polarised beam [74]. The directional emission from the antennae was proportional to the position of the antenna relative to the focal point of the beam. Fatemi demonstrated the single shot measurement of polarisation dependent spin in rubidium vapour, and used higher powers to induce position dependent atomic spin [75]. Radially polarised beams have been used for real-time, high resolution kinematic sensing [76]. The position of an object within a cylindrical vector beam can be measured by measuring the polarisation state of the beam after interaction with the object. As the polarisation is spatially variant the global average polarisation state change can be used to measure and track the particle within the beam.

In plasmon resonance sensing, the sensitivity of phase sensitive surface plasmon resonance refractive index biosensors is proportional to the phase difference in a small region in a plasmon resonance dip. A differential phase between applied azimuthally and radially polarised beams has been shown to enable surface plasmon resonance sensors with a dynamic range seven times higher than previous implementations of the technique while still maintaining a high sensitivity [77].

Laser processing is an area where vector Laguerre-Gaussian modes are of significant interest, with proven benefits over the linearly, circularly or randomly polarised beams that are currently used in industry. In general, laser processing provides key advantages over conventional machining techniques such as high productivity, quality of finish, low material waste, and high flexibility [78]. In a very simplified view of laser processing sharply focussed beams are absorbed by the work-piece material which heats a localised volume resulting in melting or vaporisation. The types of achievable laser processing are widely varied, and can include cutting, drilling, engraving and welding to name a few. One such interaction of a focussed laser beam with a material is shown in figure 2.7 where the beam is cutting a metallic sheet in a direction indicated as the processing direction. The laser melts material at a cut-front, before the melted material is removed by a gas jet (not illustrated) leaving a cut path known as a kerf. This example is often referred to as laser fusion cutting or melt-shear cutting.
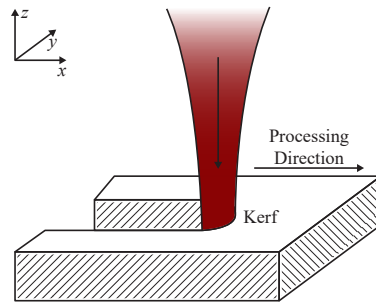
FIGURE 2.7: Illustration of a laser-material interaction typical of laser fusion cutting. Figure adapted from [79].

The intensity distribution and polarisation are important properties in processing of this type. For high speed, uniform and efficient cutting a sharp (high gradient) intensity distribution is desired, with beam shaping to 'top-hat' intensity distributions recently trending in the field. As previously mentioned, modes with higher-order Laguerre-Gaussian intensity profiles have steep intensity gradients compared to the fundamental mode, making them desirable for laser processing. The polarisation of a beam greatly affects its absorption by a material in a given configuration, and therefore directly affects the efficiency of processing. Laser-material interaction occurs on the walls of the material, as illustrated by a beam grazing the material wall at an angle of incidence shown in figure 2.8.

This is relevant because the absorption of of metals varies with the angle of incidence and the incident polarisation. The absorption is normally maximised for polarisations parallel to the plane of incidence, denoted as P-polarisation to represent parallel. The polarisation perpendicular to this is denoted as S-polarisation, with the S derived from the German word *senkrecht*, meaning perpendicular.
A graph of the absorptivity of iron as a function of angle of incidence for S- and P-polarisation is provided in the left side of figure 2.9, where the absorptivity has been calculated using Fresnel equations with the appropriate optical constants [81]. There
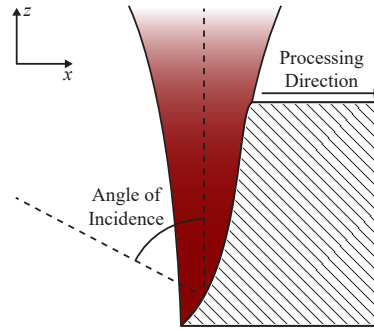
FIGURE 2.8: Cross-sectional view of laser cutting and the angle of incidence on the cut-front. Figure adapted from [80].

is a large difference between the absorptivity of the orthogonal polarisations, which the ratio of the absorptivity P-polarisation to S-polarisation plotted in the graph on the right of figure 2.9 shows can be very large at high angles.
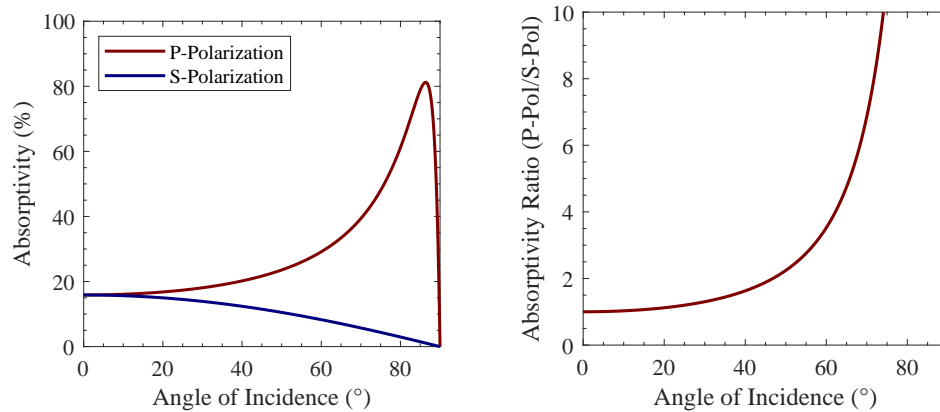
FIGURE 2.9: Left: Fresnel absorptivity of iron for S- and P-polarisation as a function of angle of incidence. Right: Ratio of P-polarisation to S-polarisation Fresnel absorptivity as a function of angle of incidence. Optical constants of elemental iron obtained from [81].

The angle of incidence in this kind of processing usually exceeds $70°$ [80], meaning that the use of P-polarisation relative to the cut-front over S-polarisation is preferred to maximise the absorption. If a linearly polarised beam is used the efficiency of the cut will depend on the orientation of the polarisation with respect to the cutting direction. For this reason, circularly polarised lasers find use over linearly polarised lasers, although the absorptivity of a circularly polarised beam incident on a material is simply the time average of S- and P-polarisations. Due to the cylindrically symmetric spatially variant nature of radial polarisation, a radially polarised beam presents P-polarisation to the material surface regardless of the beam orientation, meaning that the absorption is always maximised.

A top-down comparison between linear polarisation and radial polarisation is given in figure 2.10. The linearly polarised beam pictured on the left of figure 2.10 is orientated so that it presents P-polarisation to the cut-front in the processing direction.
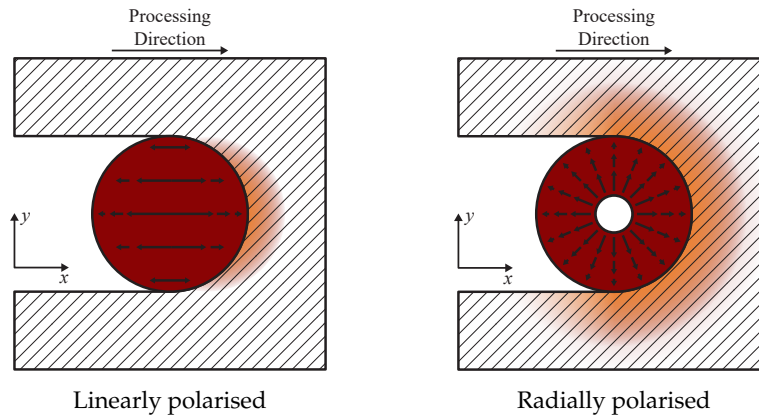
FIGURE 2.10: Top view of laser cutting with an illustration of absorption distribution in the material for P-polarised and radially polarised beams. Figure adapted from [79].

The colour shading on the material very roughly represents the heat distribution from absorption, inspired by the mathematical modelling of Niziev and Nesterov [79]. The P-polarised beam has very directional absorption, maximised at the leading edge of the cut front. In contrast, the scenario of cutting with a radially polarised beam that presents P-polarisation to the entire surface on which it is incident shows higher and more uniform absorption, leading to increased efficiency and a more isotropic kerf. This is one of the reasons used by Niziev and Nesterov to explain their theoretical findings that the laser cutting efficiency was a factor of 1.5 to 2 times higher for a radially polarised beam than for linear P-polarised and circularly polarised beams [79]. Experimentally, Weber *et al.* measured a 40% increase in cutting speed when using a radially polarised beam over a similar circularly polarised beam when cutting $2\,mm$ thick sheet steel with a CO_2 laser [80].

In laser welding, particularly with high power sources, the amount of spatter has been shown to be strongly dependent on the state of polarisation of the beam used [82]. The spatter is a detriment to the strength of a weld as it displaces material from the seam. Weber *et al.* also examined the effect of polarisation on laser welding by comparing the results from the use of a randomly polarised, radially polarised and azimuthally polarised beams at a range of feed rates [80]. They found that radially polarised beams produced noticeably less spatter, but stated that the physical mechanism behind this was at the time unknown.

Ultrafast pulsed lasers enable high precision micro drilling and their application has been well studied in metals. The geometry of boreholes drilled in this way is highly dependent on the polarisation used, with linear polarisation producing elliptical distorted holes [83]. Circular polarisation can be used to produce boreholes with improved circular profiles over those produced with linear polarisation [84]. This can also be achieved with radially and azimuthally polarised beams, with indications that there are advantages in achievable hole diameter and aspect ratio associated with their use over circularly polarised beams [85]. Meier *et al.* performed experiments comparing drilling using radially and azimuthally polarised modes,

but were not able to prove the superiority of one polarisation over another, as in different experiments the radial or azimuthal polarisations had a higher efficiency depending on the depth of the borehole and the material properties in question [86]. Meier *et al.* did however note that azimuthal polarisation had a drilling efficiency 1.5 to 4 times higher than that of radial polarisation (dependent on depth) in mild steel. A recent study by Matsusaka *et al.* investigated drilling using cylindrical vector and linearly polarised beams [87]. They found that the time required to pierce metallic samples for an azimuthally polarised beam was 2.4 to 3.2 times shorter than for the same tests with a linearly polarised beam. Their radially polarised beam had longer piercing times than the linear and azimuthal beams for all samples, and in some cases failed to pierce through at all. Significantly, they noted that azimuthal polarisation was a factor of 7.7 times faster at piercing copper than linear polarisation, providing the explanation that the number of reflections on the hole wall may be a significant factor in this performance.

2.4 Generation Methods

Despite the many and varied benefits and applications of annular modes, generating a mode of sufficient purity and power for study or use is non-trivial. The spatially variant nature of vortex and vector Laguerre-Gaussian modes normally requires the use of advanced techniques and optical components to achieve these properties. A review of some of the reported generation methods for these Laguerre-Gaussian modes is included here, but is by no means a complete survey. The methods are separated into intracavity and extracavity categories for clarity, where intracavity methods normally use a method to force a laser to operate on a desired mode, while extracavity methods may use conversion techniques to obtain the desired mode from a more easily obtainable source. Intracavity techniques often have the benefit of simplicity, as they may not require the bespoke optical components of comparable extracavity techniques. The cavity losses resulting from additional intracavity components can, however, significantly increase laser thresholds and reduce slope efficiencies.

2.4.1 Generation of Vortex Modes

Intracavity Methods

One of the most basic methods of obtaining annular Laguerre-Gaussian modes is through loss-shaping. In this approach, the thresholds of modes with intensity profiles significantly different than the desired mode is increased by introducing transverse varying loss to a cavity. An easy way to do this is to use a spot defect on a cavity optic to increase the loss to all modes without a central intensity minimum, as used by Ito *et al.* [88] and Vyas *et al.* [89]. Hu *et al.* performed a numerical investigation into spatial loss shaping to iteratively determine optimum mask geometries

for generating higher-order Laguerre-Gaussian modes [90]. Another notable use of intracavity loss for mode selection was the generation of vortex modes in a fibre laser with an external polarisation selective cavity by Lin *et al.* [91]. In this paper the authors explain that they were able to exploit birefringence from anisotropies in the fibre (possibly arising from fabrication) in combination with the polarisation selective cavity to achieve a low threshold for the desired vortex modes relative to other competing modes. While introducing additional loss in the cavity is an easy method of obtaining outputs with annular Laguerre-Gaussian profiles it has the disadvantage of reducing laser efficiency.

Gain shaping is similar in concept, but here high gain is available to modes with the desired intensity profile. This is most easily achieved in end-pumped lasers, where the pump distribution is matched to the intensity distribution of the desired mode, so that the overlap factor (given by the overlap integral in equation 2.17) is high. Multiple demonstrations of the generation of Laguerre-Gaussian modes have been published, most of which use pump light that has been converted to an annular shape. This can be achieved using spatial light modulators [92], defocussed multi-mode fibre output [93], diffracted pump beams [94], and capillary pump-delivery fibres [95]. An interesting use of gain competition was developed by Kim and Kim [96]; they used a double resonator with fundamental mode operation in a secondary cavity depleting gain from the centre of the pumped region in the gain medium, so that the primary cavity was forced to operate on the vortex LG_{01} mode.

Gain and loss shaping alone do not guarantee a particular output mode, as several modes may share an intensity profile. In particular, vortex Laguerre-Gaussian modes of the same order with opposite handedness are unfortunately degenerate in all other properties. Explicitly, two modes with azimuthal index $\pm l$ respectively, have the same beam radius, curvature and Gouy phase shift. Without control of the handedness a laser may operate on either or both at the same time. A laser operating on two Laguerre-Gaussian vortex modes of opposite handedness may form coherent superpositions of both modes, resulting in 'petal' like structures, or incoherent superpositions with intensity distributions indistinguishable from a pure vortex mode as observed by Litvin *et al.* [97]. Therefore, a laser that appears to operate on a Laguerre-Gaussian mode may not carry a clear charge of OAM. The presence or lack of spiral phase should be therefore be confirmed using a measurement such as interferometry.

Several methods have been demonstrated that appear to allow for handedness selection for intracavity generation of vortex modes. Nanoscale aluminium stripes were used in a laser cavity by Lin *et al.* to introduce additional loss to one handedness by aligning the stripes so that they overlapped with the instantaneous maxima of one handedness and the minima of the other [98]. The desired handedness could be switched by repositioning the nanoscale stripes. Kim *et al.* reported that an angled etalon inserted into a cavity could introduce differential loss to the opposite handedness vortex modes [99]. Their paper states that due to the Poynting vector

skew angle dependence on the value and sign of l, a tilted intracavity glass plate can introduce a reflection loss that is different for left and right handed vortex beams. Liu *et al.* obtained similar results through the use of an intracavity black phosphorous plate [100]. Zhou *et al.* constructed a hybrid free-space and fibre ring resonator with intracavity conversion of the fundamental Gaussian mode to a vortex Laguerre-Gaussian using spatial light modulators [101]. By changing the phase pattern loaded to the spatial light modulator they could directly select the handedness and mode order up to $|l| = 10$.

Extracavity Methods

One of the earliest extracavity methods of generating vortex modes was reported in the seminal papers of Allen *et al.* [18, 21]. In these papers they suggested, then demonstrated, that higher-order Hermite-Gaussian modes could be converted to vortex Laguerre-Gaussian modes with very high efficiency through the use of the astigmatic Gouy phase shift introduced by a cylindrical lens pair. This concept was advanced by Uren *et al.* [102] through the use of spherical mirrors and is used to generate vortex Laguerre-Gaussian modes in section 3.2.2 of this thesis.

Spiral phase plates are another tried and tested method of generating vortex Laguerre-Gaussian modes with a wide range of papers over a number of years demonstrating their use [103, 104, 105, 106, 107, 108]. A spiral phase plate retards the phase front of an incident beam by having an optical path length that varies azimuthally, with one or more modulus steps depending on the desired output mode order. This allows for convenient extra cavity generation of a vortex mode with good conversion efficiency. The difficulty of fabricating spiral phase plates has classically been a primary drawback, although they are now commercially available for an appropriate premium price. Advances in fabrication techniques have enabled more efficient spiral phase plates with continuous phase variation though the use of techniques such as electron beam writing [109], direct laser writing [110], and focussed ion beam milling [111]. Particularly impressive is the fabrication of micro-scale spiral phase plates directly onto a VECSEL [112] and the tip of an optical fibre [113].

Holographic optical elements are a class of techniques that have been used to generate optical vortices, though it should be noted that they do not generally produce a single pure mode, but fourier components with multiple modal orders that form a superposition of Laguerre-Gaussian modes in the far-field [114]. The generation efficiency of a single mode order is therefore low. Examples of holographic optical elements for generating vortex modes include fork gratings [115, 116, 117, 118, 119], and spiral Fresnel plates [116, 120, 121, 122]. Spatial light modulators have been used to generate holographic amplitude masks [123] in addition to direct phase modulation [124], with the significant advantage that they can be rapidly reprogrammed. Digital micromirror devices are an alternative adjustable device offering faster switching than spatial light modulators with lower device cost. They

have also been used to form fork gratings for generating vortex beams [125]. Digital micromirror devices cannot directly adjust the phase of an incident beam, but in conjunction with suitable experimental setups they allow for the necessary phase and amplitude modulation to generate vortex modes [114, 126], albeit with poor efficiency compared to the use of a spatial light modulator.

Extracavity conversion by means of coupling to annular vortex modes in fibres is currently a popular topic of research due to the widespread adoption of optical fibres in communication and the desire to utilise vortex modes for this purpose. A fundamental mode was selectively coupled to annular modes by Ismaeel *et al.* [127], although these were not pure vortex modes due to the aforementioned degeneracy of modes with the same azimuthal order but opposite handedness. Various fibre-based methods have since been demonstrated that attempt to break this degeneracy [128, 129, 130].

Some of the more novel extracavity techniques to generate vortex modes published in the last few years include metamaterials. Devlin *et al.* presented a meta-material surface able to convert incident planar waves with spin angular momentum into vortex waves possessing orbital angular momentum [131]. Ren *et al.* also recently published a meta-holographic surface designed to produce a multiplexed range of vortex modes for communication applications [132].

Coherent beam combining is a research topic that shows promise for overcoming the limits of single lasers where multiple sources are coherently combined to form a single beam with brightness well exceeding that of its component elements. Hou *et al.* recently presented a theoretical discussion that a coherently combined phased array may be able to form a vortex beam in the far-field when assisted by a machine learning algorithm [133].

2.4.2   Generation of Vector Modes

Intracavity Methods

The earliest demonstration of a laser operating on cylindrical vector modes was performed by D. Pohl in 1972 [134]. Direct generation of a first order azimuthally polarised mode in a ruby laser was achieved through the use of a loss-inducing aperture and central stop, and a birefringent calcite crystal inside a telescope. The central stop was included to discriminate against the fundamental mode and the aperture had the same purpose for higher order modes. The birefringence of the calcite crystal caused light with radially aligned polarisation to experience a higher magnification from the telescope and therefore higher loss from the aperture. The birefringence was necessary to provide polarisation based selection between radial and azimuthal modes that are otherwise degenerate in other properties. This intracavity polarisation selection technique was refined in more recent years to utilise thermally induced bifocussing in laser crystals, negating the need for the inclusion

of separate birefringent optical elements [135, 136, 137]. The use of thermally induced bifocussing is discussed extensively in section 3.1 of this thesis, where it was used to create a radially polarised source.

The generation of a radially polarised output has previously been accomplished by Bisson *et al.* through the inclusion of an intracavity Brewster-angled conical axicon [138]. As the conical axicon satisfies the Brewster condition at any azimuthal coordinate it forces the laser to operate on radially polarised modes. The output beams in [138] were composed of a superposition of high order modes (of tenth order and higher) and took the forms of ring and arc-like beams due to high divergence arising from uncompensated refraction from the conical axicon. Kozawa *et al.* constructed a source operating on a first-order radially polarised mode that eliminated the occurrence of high intracavity divergence angles by using a Brewster-angled convex and concave conical prism pair with an index matching immersion liquid filling the space between them [139].

Another possible method of producing cylindrical vector modes is through the use of bespoke feedback elements. Erdogan *et al.* proposed and demonstrated concentric circle gratings as a Bragg reflector on a semiconductor laser in [140]. In this paper the authors used electron beam lithography to fabricate a concentric circle grating into the upper AlGaAs layer of a AlGaAs/GaAs semiconductor laser. The use of the concentric circle grating in a Bragg resonator caused the laser to operate on a superposition of multiple azimuthally polarised modes, with some superpositions being cylindrically symmetrical in the far-field. A circular grating structure was later integrated into a multilayer dielectric mirror by Ahmed *et al.* to create an optic with a reflection coefficient for radial polarisation of 99.6% and as low as 76% for azimuthal polarisation when measured at a wavelength of 1030 nm [141]. In the same paper, Ahmed *et al.* used this grating mirror as a high-reflector in the cavity of a disk laser, achieving a high quality first-order radially polarised mode source with an output power of 10 W. The same group later used this concept to directly generate azimuthally polarised modes from a disk laser [142], a 3 kW radially polarised CO_2 laser [143], a 1 kW continuous-wave radially polarised thin-disk laser [144], and a picosecond pulsed radially polarised thin-disk laser with 1.6 μJ pulse energy and 125 W average power [145].

Extracavity Methods

Extracavity methods of generating cylindrical vector modes mostly rely on the conversion or combination of modes with readily obtainable homogeneous polarisation states. Radial analysers based on birefringence [146] and dichroism [147] have been previously used to convert light with circular polarisation to radial and azimuthal polarisations, however this transformation also results in an associated geometric phase shift that imparts a vortex phase (creating a so-called vortex-vector or Poincaré sphere beam) onto the output beam that must be compensated for to produce a pure cylindrical vector mode.

The interferometric combination of in-phase linearly polarised Hermite-Gaussian modes (as described by equation 2.55 in the case of a radially polarised LG_{01}) is a relatively simple method for generating cylindrical vector modes [148, 149, 150]. The use of interferometry to generate vector modes does, however, require good coherence and stability in the component beams.

Spatially variant polarisation rotation can be achieved through a number of methods. In this approach, light with a homogeneous polarisation is used in an input and locally retarded so that the desired spatially variant output polarisation distribution is created. The use of twisted nematic liquid crystals sandwiched between a linearly-rubbed and circularly-rubbed plate is one such method [151, 152]. Alternatively, liquid crystals can be photo-aligned to gain spatially variant retardance [153]. Spatial light modulators can achieve the same effects in conjunction with a quarter waveplate while having the advantage of flexibility. Spatially variant subwavelength metal stripe gratings produced via photolithography were able to operate in a similar way to convert incident circular polarisation from a CO_2 laser to a radially polarised mode (with an additional spiral phase factor) [154], although it should be noted that this approach would be difficult to achieve for shorter wavelengths.

Spatially variant waveplates, sometimes known as S-waveplates or q-plates, achieve the necessary anisotropic retardance by having a fast axis that varies with azimuthal position on the plate. The first demonstrations of such a device were segmented waveplates. The operating principle of one such device is shown in figure 2.11.
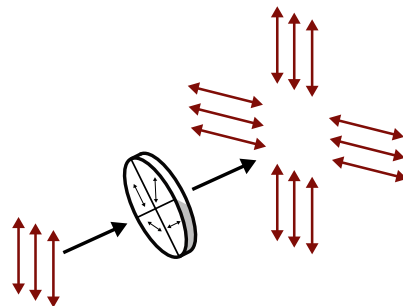
FIGURE 2.11: The operating principle of a spatially variant waveplate.

In this example, linearly polarised light is transmitted through a spatially variant waveplate comprised of four bonded half-waveplate segments with fast axes alignment indicated by arrows on each quadrant. The transmitted light is approximately radially polarised. Machavariani *et al.* constructed an eight-segment waveplate able to convert a linearly polarised mode to either a radially or azimuthally polarised mode [155]. The use of trifold symmetrical mechanical stress on the circumference of a cylindrical window has been shown to produce spatially variant birefringence in finite element modelling and experiments on BK7, that when illuminated with linearly polarised light produces a spatially variant counter-rotating polarisation distribution with azimuthal and radial components [156]. This polarisation state could

be rotated to a radial or azimuthal state by propagation though a half-waveplate rotated to the appropriate angle. A more robust way of creating a spatially variant waveplate is through femtosecond laser writing of anisotropic nanogratings in glass, pioneered by Beresna et al. [157, 158]. These femtosecond laser written S-waveplates have been used quite successfully, for example, to produce high quality radially polarised modes from a Yb-doped fibre laser [159] and as part of a high power pulsed Yb-doped fibre amplifier chain to ensure a radially polarised output [160]. Until recently the single-pass loss of these femtosecond laser written S-waveplates discouraged intracavity use; the demonstration and loss characterisation of a new generation through intracavity use is the subject of chapter 5 in this thesis.

The creation of custom anisotropy with arbitrary distribution in transmissive metasurfaces has seen advances in control and a reduction in the optical loss in recent years. Arabi *et al.* fabricated arrays of elliptical amorphous silicon posts on a silica substrate [161]. The elliptical cross-section of the amorphous silicon posts created local birefringence aligned with the major and minor axes. The ability to orientate each amorphous silicon post allowed the authors to create a metamaterial waveplate for the conversion of linearly polarised laser modes to first-order radially and azimuthally polarised modes of high quality with a noted single-pass transmission of 96%. Similar in concept, a paper published by Yue *et al.* presented the fabrication and use of a metasurface with rectangular nanorods varying in orientation over the surface to create a spatially varying anisotropy [162].

A step-index cylindrical waveguide such as an optical fibre can support annular modes in some cases, such as the TE_{01} and TM_{01} modes which have radial and azimuthal polarisation respectively. It is possible to transfer energy to these modes from other transverse modes through careful misalignment, exemplified by Grosjean *et al.* by misaligning the cores of a single-mode fibre (fundamental) with a few-mode fibre (fundamental, TE_{01}, and TM_{01}) [163]. The conversion efficiency using this approach is low (less than 10%) and sensitive to small perturbations. The efficiency of coupling to cylindrical vector waveguide modes can be improved somewhat (to around 30% to 50%) by using higher order modes such as a non-vector LG_{01} [164] or HG_{01} [165] as an input, though generating these modes is a challenging and low efficiency process when compared to the fundamental mode anyway. Narrow linewidth fibre lasers have more recently made use of fibre Bragg gratings as a mode selective element in conjunction with offset fibre coupling [166, 167]. The narrow reflection band of the fibre Bragg grating allows for selective reflection of the fundamental mode while allowing the higher-order vector modes to be coupled out of the fibre laser.

2.5 Current Limitations of Annular Mode Sources

The applications reviewed in section 2.3 require high quality vortex or vector modes with well defined OAM or polarisation states respectively, and at high powers for

laser processing.

The quality of higher-order transverse modes is a poorly defined topic at present; a survey of the intensity profiles presented in all the publications reviewed as generation methods in section 2.4 would reveal high variation in appearance. Some of the published modes are barely indistinguishable from theoretical intensity distributions, while others have significant defects or impurities. The most popular quantitative measure of beam quality, M^2, can be fooled while measuring a higher-order mode through the inclusion of impurities of other mode orders, as described in section 2.1.5. A poor quality LG_{01} mode, for example, can be measured as having a 'perfect' M^2 of 2.0. Unfortunately this means that it is difficult to directly compare the merits of generation methods of annular modes based on beam quality due to lack of a suitable quantitative metric. Chapter 4 of this thesis describes experiments on modal decomposition using modern machine learning techniques as a potential tool to help better quantify higher-order modes. Furthermore, the properties of vortex and vector modes are often confused in the literature, particularly with regards to mislabelling vector modes as OAM/vortex modes. Sometimes the presence of an annular intensity profile is enough to mislead authors to claim vortex or vector properties, despite the possibility of such an intensity profile being the result of neither [97]. Chapter 3 documents the construction and characterisation of a radially polarised laser and and a vortex Laguerre-Gaussian mode source with an emphasis on producing high quality beams with well defined properties for use in subsequent studies.

The output powers of annular modes for the most part remain low compared to the multiple kilowatts achieved for fundamental Gaussian modes. The majority of the vortex Laguerre-Gaussian modes published in the last decade had maximum output powers lower than $10\,W$, although there have been some high peak power femtosecond demonstrations at large laser facilities in the past three years using refined and novel generation methods such as plasma fork gratings [168], plasma mirrors [169], and spiral phase mirrors [170]. The optical elements used to generate vortex modes often prove a limiting factor in power scaling, having low optical damage thresholds, small apertures, low efficiencies and high losses. Vector Laguerre-Gaussian modes have achieved somewhat higher power with circular grating mirrors allowing for the aforementioned kW level continuous wave radially polarised lasers [143, 144]. An S-waveplate produced using a refined femtosecond laser writing technique to reduce the transmission loss is trialled as an intracavity element and reported on in chapter 5, showing promising results for the future generation of annular modes using these elements.

In an effort to generate higher power annular modes while dealing with the limitations and difficulties posed by the various generation methods there have been a number of researchers examining amplification of annular modes in several different gain media geometries, such as rods [171], slabs [172], fibres [173], and thin-disks

[174]. While amplifying a low power mode separates the problems of power scaling and generation, optical amplification is itself limited by a range of problems like thermal effects, non-linear phenomena, and damage thresholds. Rod-based gain media geometries tend to suffer in particular from thermal effects due to a relatively low surface area to volume ratio. Slab geometries have improved thermal management, but do have astigmatic thermal lensing that has to be accounted for. Disk geometries have good thermal handling with a high surface area and primarily longitudinal temperature gradient, and have produced the highest continuous and average power annular modes so far. However, it has been noted that the low single-pass gain necessitating multi-pass configurations can lead to complex set-ups and instability. Fibre amplifiers have proved successful in scaling annular modes past the $100 \, W$ average power level [160], however the small mode areas and long interaction lengths seen in fibres leads to low thresholds for deleterious non-linear effects, particularly in pulsed regimes of operation. In addition, the coupling to other waveguide modes in fibres can degrade the purity of a propagated vortex or vector mode.

The desire to mitigate against the multiple limiting effects in amplifier geometries for the scaling of annular modes, and laser sources in general, has inspired the development of novel or hybrid geometries. For example, photonic crystal fibres [175], and single crystal fibres [176] have found use in amplifying radially polarised modes due to the ability to tailor supported fibre modes, with the latter citation containing a useful review on the recent highest peak powers and pulse energies obtained for radially polarised modes. The successful amplification of both a vortex, and a radially polarised Laguerre-Gaussian mode in a hybrid thermally guiding fibre-rod geometry presented in chapter 6 is one such potential new avenue to advance the obtainable powers of annular modes.

While the development and use of annular mode lasers is not yet a mature field, recent progress is very encouraging. This thesis attempts to address several aspects of limitations affecting the modes of interest, and it is hoped to advance the understanding, quality, and obtainable output powers of vortex and vector Laguerre-Gaussian modes.

Chapter 3

Annular Mode Solid-State Sources

3.1 Radially Polarised Source

This section details the development of a radially polarised source primarily designed for optimised beam quality, polarisation, and modal purity. A high quality radially polarised seed source was deemed necessary for the amplification experiments details in chapter 6 in order to isolate and understand any undesirable characteristics arising from the amplification process. The radially polarised source that was constructed achieved the desired properties by using a combination of the previously used techniques of thermally induced bifocussing and pump beam conditioning.

3.1.1 Annular Pump Distribution

A common problem encountered with directly generating radially polarised modes inside a laser cavity is that of other modes competing for gain. Compared to fundamental modes, where simple apertures and 'top-hat' pump beam profiles usually suffice to suppress higher-order modes, more care must be taken to obtain a pure higher-order mode. If an inappropriate spatial distribution of the pump light is chosen a laser resonator may operate above threshold on a number of undesired transverse modes that overlap the pumped region of a gain medium. An expression for the threshold pump power of a four-level laser can be obtained by substituting equation 2.19 into equation 2.17 and assuming $(L + T) \ll 1$ [177].

$$P_{pth} = \frac{h\nu_p A_{eff}(L+T)}{2\sigma_{21}\tau_f \eta_{abs}\eta_q}$$

(3.1)

Here h is Planck's constant, ν_p is the pump frequency, L is the round-trip resonator loss, T is the transmission of the output coupler, σ_{21} is the emission cross-section, τ_f is the upper-state fluorescence lifetime, η_q is the pump quantum efficiency, and η_{abs} is the pump absorption efficiency. A_{eff} is a term that represents the effective area overlap between the pump and cavity photon distributions, defined as

$$A_{eff} = \left(l_c \int_{cavity} r_0(r,z)s_0(r,z)dV \right)^{-1}$$

(3.2)

where l_c is the cavity length, and r_0 and s_0 are the normalised spatial distributions for pump rate per unit volume and laser photon density respectively. A_{eff} therefore has a great effect on the transverse spatial modes that will be operating above threshold in a given laser cavity. In order to directly excite a targeted radially polarised annular profiled transverse mode, the pump distribution can be altered to match the targeted mode. J.W. Kim *et al.* showed in [178] that pump light from a commercial diode laser could be reconditioned into an annular profile by coupling the pump into the glass region of a capillary fibre in order to directly excite annular profiled LG_{0n} modes in a Nd:YAG laser. They showed that by assuming that the pump beam has an annular step profile with inner radius a and outer radius b, and is absorbed with a coefficient α_p, the pump rate density can be given as

$$r_0(r,z) = \begin{cases} \frac{\alpha_p exp(-\alpha_p z)}{\pi(b^2-a^2)\eta_{abs}} & (a \leq r \leq b); \\ 0 & \text{elsewhere} \end{cases} \tag{3.3}$$

The normalised photon density of a Laguerre-Gaussian mode of azimuthal order l and (fundamental) spot size $w(z)$ is given by [179]

$$s_0(r,z) = \frac{2}{l!\pi w^2(z)l_c} \left(\frac{2r^2}{w^2(z)} \right) exp \left(\frac{-2r^2}{w^2(z)} \right) \tag{3.4}$$

From these expressions, it can be shown after assuming negligible beam divergence within the gain medium that

$$A_{eff} = \frac{\pi(b^2-a^2)}{\eta_{PL}} \tag{3.5}$$

where η_{PL} is the overlap factor of the pump with the laser mode:

$$\eta_{PL} = \sum_{m=0}^{n} \frac{1}{(n-m)!} \left[\left(\frac{2a^2}{w_0^2} \right)^{n-m} exp \left(-\frac{2a^2}{w_0^2} \right) - \left(\frac{2b^2}{w_0^2} \right)^{n-m} exp \left(-\frac{2b^2}{w_0^2} \right) \right]. \tag{3.6}$$

Using these expressions, one is able to calculate the threshold of a given azimuthal order of annular transverse mode given the dimensions of the pump profile. This led to the selection of a capillary fibre that could be used to create an annular pump profile with the distribution indicated in equation 3.3 with appropriate inner and outer diameters. The capillary fibre used in the experiments in this thesis was chosen to have an inner radius, a, of 50 μm and outer radius, b, of 100 μm. Figure 3.1a shows a magnified cleaved end-facet view of the capillary fibre used in these experiments. In order to couple the light from a commercial fibre-coupled laser diode into the capillary fibre for use in generating annular transverse modes the capillary fibre was tapered by Gooch and Housego PLC. The tapering process involves drawing the heated capillary fibre such that the central air-hole collapses. This tapered capillary is then spliced to the multi-mode pump-delivery fibre of the selected diode laser pump source.
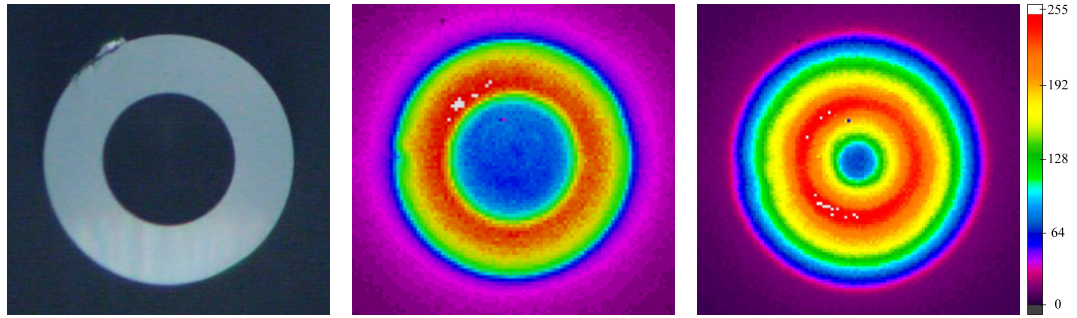
(A) End-facet view of a capillary fibre with a 100 μm diameter central air hole and 200 μm diameter silica light-guiding ring.

(B) Focus of the the pump spot from a multimode diode laser after guidance through a section of capillary fibre.

(C) Near-field image of the pump spot from a multimode diode laser after guidance through a section of capillary fibre.

FIGURE 3.1: Capillary fibre used to condition pump light to form an annular near-field profile

Figure 3.1b is a CCD camera image of the focussed output of the same capillary fibre as shown in figure 3.1a when spliced to a commercial 940 nm fibre-coupled diode laser. It is evident that the focussed spot obtained from propagating and imaging pump light through a capillary fibre does not exactly match up to the idealisation presented in equation 3.3 due to the presence of non-zero intensity in the central hole. However, this method of pump conditioning has been used to successfully generate high quality annular modes [180]. This approach was therefore selected for use in the design and construction of a radially polarised source for use in further experiments.

During the construction of the sources utilising these capillary fibres experimental optimisation revealed that positioning the focus of the light from the capillary fibre directly on the laser crystal was not the ideal configuration for the short crystals used in these experiments. In practice it was found that sharply focussing the capillary pump spot into a laser crystal in an effort to obtain a first order annular mode led to an increase in the fundamental mode content of the obtained transverse mode. Instead, a slightly defocussing the pump beam by offsetting the pump focus with respect to the laser crystal was found to be optimal. The same output from the capillary fibre shown in figures 3.1a and 3.1b is again imaged in figure 3.1c at an axial position 5 mm before the focal point imaged in figure 3.1b, showing a closer visual match to the targeted annular mode. It is important to note that this slight change of pump focal point position with respect to the gain medium will only be valid for gain media that are short compared to the Rayleigh range of the pump beam, as was the case with the constructed radially polarised source. To analyse why this slight defocussing of the light from a capillary fibre was beneficial in obtaining a radially polarised mode, intensity in a horizontal cross-section of the centre of figure 3.1b was compared to the targeted LG_{01} intensity profile in figure 3.2. In this graph, the overlap integral between the transverse pump intensity distribution and the intensity distribution of an LG_{01} mode is maximised by scaling the cavity mode radius
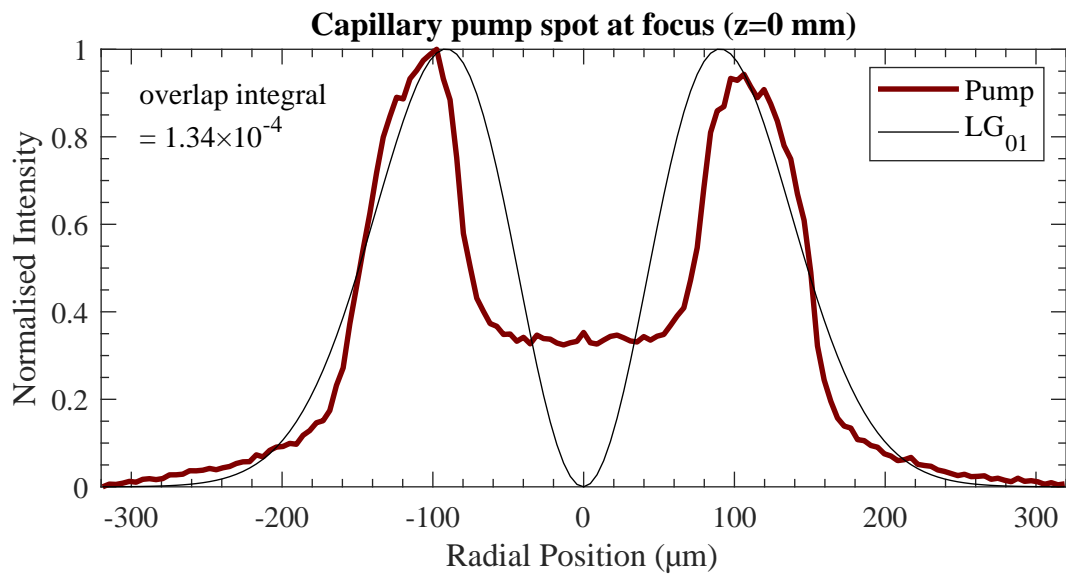
FIGURE 3.2: Transverse pump distribution of sharply focussed light
from a capillary pump-delivery fibre compared to a theoretical LG_{01}
mode.
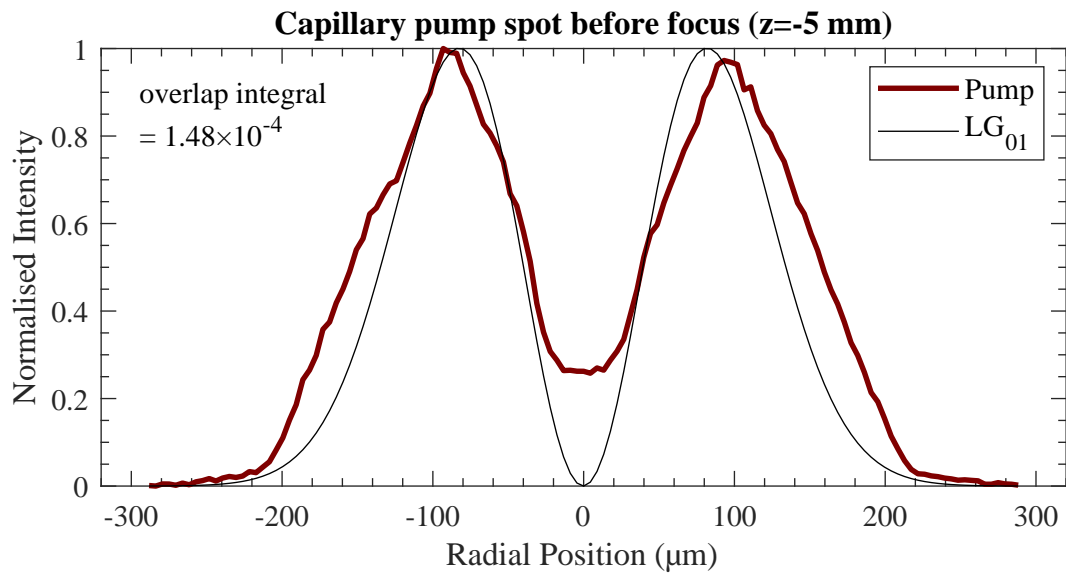
FIGURE 3.3: Transverse pump distribution 5 *mm* from the focus of
light from a capillary pump-delivery fibre compared to a theoretical
LG_{01} mode.

relative to the pump spot. While the pump distribution shown in figure 3.2 is a good fit to the first order LG_{01} mode, it is certainly not the form we modelled in equation 3.3, and there is some intensity present in the centre of the pump beam that could cause the presence of undesired fundamental cavity modes.

For comparison, a similar graph for the slightly defocussed pump light is given in figure 3.3. Due to an increased overlap integral over that of the tightly focussed pump beam, one can quantitatively see why this change of pump spot position relative to a gain medium would ensure a higher quality first-order annular mode.

3.1.2 Thermally Induced Birefringence

While shaping the pump light for directly exciting annular modes within a cavity has been previously successful, it is necessary to engineer a laser cavity designed to output on a radially polarised mode with some mechanism to discriminate against degenerate modes. Specifically, the intensity profile of a LG_{01} mode is shared across a number of annular modes with different properties, such as vortex phase modes, cylindrical vector modes and incoherent superpositions of modes. For the purpose of constructing a radially polarised source with excellent polarisation and mode purity, a previously published technique exploiting thermally induced birefringence was used [137]. This method was chosen in order to avoid using bespoke optical components and arrangements while avoiding the losses associated with extra-cavity methods. In this method, a laser resonator is designed such that there is a difference in the cavity stability between the degenerate transverse modes. This is achievable in laser crystals that exhibit thermally induced bifocussing, where azimuthal and radial polarisations experience different refractive indices due to stresses in the material arising from a non-uniform temperature distribution. This birefringence can cause the focal lengths of the thermal lens in the laser crystal to differ between these polarisations, which can be exploited when designing a laser cavity. Koechner provides the following mathematical description of this effect which was used to aid the design of the resonator geometry used in these experiments [5].

We will assume that the gain medium in this description is a cubic crystal with cylindrical rod geometry with flat, free ends, is in thermal contact with a coolant on the cylindrical surface, and that heat-flow is strictly radial. The key crystal properties are heat generated per unit volume, Q, whose the exact form depends on the pump light distribution, radius r_0, and thermal conductivity K. This heat generation, arising from effects such as quantum defect heating, causes a non-uniform temperature distribution in the crystal. In the case of end-pumping this distribution has a maximum in the centre of the crystal and a temperature which decreases with radial position. The temperature distribution in a cylindrical laser crystal with the stated

assumptions can be expressed as

$$T(r) = T(r_0) + \left(\frac{Q}{4K}\right)(r_0^2 - r^2). \tag{3.7}$$

In designing the radially polarised source, the heat generated per unit volume is assumed to be uniform and is given by

$$Q = \frac{P_h}{\pi r_0^2 l_c} \tag{3.8}$$

where P_h is the pump power deposited as heat. It is worth noting that the annular pump spot from a capillary fibre will give a different form to the heat density, and a better approximation of an expression for the heat density may be found in the work of Kim *et al.* [181]. However, the assumption of a uniform pump deposition density is a sufficient approximation for the purpose of experimental design [182].

Temperature gradients of the form in equation 3.7 cause mechanical stress within a laser crystal as the inner area is limited from thermal expansion by the cooler exterior regions. The laser crystal will experience the following stresses in the radial σ_r, tangential σ_ϕ, and axial σ_z coordinates.

$$\sigma_r(r) = QS(r^2 - r_0^2) \tag{3.9}$$

$$\sigma_\phi(r) = QS(3r^2 - r_0^2) \tag{3.10}$$

$$\sigma_z(r) = QS(4r^2 - 2r_0^2) \tag{3.11}$$

Where $S = \alpha E[16K(1-\nu)]^{-1}$ with α being the thermal expansion coefficient, ν Poisson's ratio, and E the Young's modulus of the material. These stresses result in radial and tangential refractive index variation due to the photoelastic effect, which are given by Koechner [5] as

$$\Delta n_r = -\frac{1}{2} n_0^3 \frac{\alpha Q}{K} C_r r^2 \tag{3.12}$$

$$\Delta n_\phi = -\frac{1}{2} n_0^3 \frac{\alpha Q}{K} C_\phi r^2 \tag{3.13}$$

Here n_0 is the intrinsic material refractive index and the constants C_r and C_ϕ are calculated from the elasto-optical coefficients of the material. For a YAG crystal along the [111] direction, $C_r = 0.017$ and $C_\phi = -0.0025$ [5]. The different values of these constants explains the birefringence between the two states of polarisation.

The photo-elastic refractive index contributions are not the only changes of refractive index that occur from the heat generated in a gain medium. The total refractive index as a function of radial position can be expressed by combining the intrinsic material refractive index, n_0, the temperature contribution, $\Delta n_T(r)$ and the stress contribution $\Delta n_\sigma(r)$. Contributions from end-face curvature due to differential expansion are neglected here due to their small magnitude relative to the other

terms [5].

$$n(r) = n_0 + \Delta n_T(r) + \Delta n_\sigma(r) \tag{3.14}$$

We can obtain the temperature contribution by using the temperature dependent change of refractive index:

$$\Delta n_T(r) = \frac{dn}{dT}[T(r) - T(0)] = -\frac{Q}{4K}\frac{dn}{dT}r^2 \tag{3.15}$$

Combining these contributions, the refractive index profile in the laser crystal is

$$n(r) = n_0 \left[1 - \frac{Q}{2K}\left(\frac{1}{2n_0}\frac{dn}{dT} + n_0^2\alpha C_{r,\phi}\right)r^2\right] \tag{3.16}$$

with $C_{r,\phi}$ denoting the use of one of these constants to give the refractive index profile for radial or azimuthal light respectively. If we now treat the laser crystal as a gradient index lens, we can find an expression for the thermal focal lengths of the laser crystal for the different polarisations of light. Under the assumption that the thermal lens focal length will be long compared to the crystal, a gradient index medium of length l_g with a refractive index of the form

$$n(r) = n_0 \left(1 - \frac{2r^2}{q^2}\right) \tag{3.17}$$

has an approximate focal length of

$$f \approx \frac{q^2}{4n_0 l_g}. \tag{3.18}$$

By comparison with equation 3.16 we can now give an expressions for the focal lengths of radial and azimuthal polarisations in a thermally lensing crystal that can be used to help design a laser cavity to obtain a radially polarised mode:

$$f_r = \frac{K}{Ql_g}\left(\frac{1}{2}\frac{dn}{dT} + \alpha C_r n_0^3\right)^{-1} \tag{3.19}$$

$$f_\phi = \frac{K}{Ql_g}\left(\frac{1}{2}\frac{dn}{dT} + \alpha C_\phi n_0^3\right)^{-1}. \tag{3.20}$$

Recall that the constants C_r and C_ϕ have opposite signs in a YAG crystal. This means that radially polarised light experiences a stronger lensing effect due to the positive contribution from the thermally induced stresses in the laser crystal, while azimuthally polarised light experiences weaker lensing by comparison. By designing a laser cavity such that the geometric path of the light is stable on a round-trip between the cavity mirrors for radially polarised light but not azimuthally polarised light, we can discriminate against unwanted degenerate modes and obtain a pure radially polarised mode.

3.1.3 Experimental Configuration
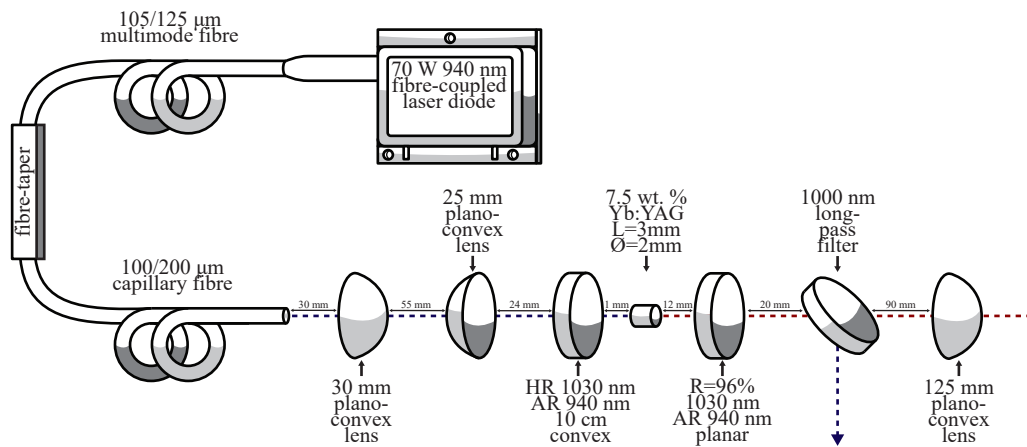
FIGURE 3.4: Schematic of the end-pumped 1030 nm radially polarised Yb:YAG laser

The constructed radially polarised source employed a simple two-mirror resonator, as shown in figure 3.4. The first cavity mirror was a convex pump input-coupler mirror with a 100 *mm* radius of curvature, a high reflectivity ($> 99.8\%$) at the lasing wavelength of 1030 *nm* and high transmission ($> 98\%$) at the 940 *nm* pump wavelength. The other cavity mirror was a planar output-coupler mirror with a reflectivity of 96% at 1030 *nm* and a high transmission at the pump wavelength. The chosen gain medium was a cylindrical rod Yb:YAG laser crystal with a diameter of 2 *mm*, a length of 3 *mm* and a Yb^{3+} ion doping concentration of 7.5 *wt.%*. The Yb:YAG crystal was mounted in a water-cooled copper heat-sink to aid in temperature control. The crystal was positioned approximately 1 *mm* from the convex input-coupler. The separation between the cavity mirrors was chosen to be 15 *mm*. The choice of a convex-plane laser cavity was influenced by equations 3.19 and 3.20 and the desire to keep the laser cavity short for benefits to possible pulsed operation. This convex-plane cavity is an intentionally unstable resonator for azimuthally polarised modes, while the thermal lensing experienced by the radially polarised mode is strong enough to compensate for the curvature of the input coupler.

A commercial fibre-coupled laser diode (nLight Inc.) with a central wavelength of 940 *nm* and a maximum output power of 70 *W* was used as the pump source. The pump delivery fibre was multi-mode with a 105 *µm* diameter core with a numerical aperture (NA) of 0.22 and a 125 *µm* outer cladding diameter. This pump delivery fibre was spliced to fibre of the same type which was tapered to a capillary fibre (referenced in section 3.1.1) with a 200 *µm* outer diameter and a 105 *µm* diameter inner air-hole. The capillary fibre tapering was performed by Gooch & Housego PLC. The output from the laser diode was conditioned by propagation through the capillary

fibre to have an annular transverse profile in the near-field. The pump light was imaged into the laser crystal using a plano-convex lens pair with focal lengths 30 *mm* and a 25 *mm* in a '4f' configuration; the first lens is positioned by its focal length from the object, the lenses are separated by the sum of their focal lengths, and finally the image is formed at a distance from the second lens equal to its focal length. This ensures a well defined magnification factor of 0.8$\dot{3}$ and flexibility in focus position through slight adjustments of the position of the second lens. The magnified pump spot therefore has an outer diameter of 169 *μm* and a 72 *μm* diameter central hole. These pump spot dimensions were chosen to provide a good overlap with the calculated mode size of a first-order radially polarised mode within the laser crystal. The short, highly doped laser crystal was chosen due to the poor beam quality ($M^2 \approx 50$) of such a multi-mode and conditioned pump spot, as well as the consideration that the pump beam is only annular in profile in the near-field, which should help suppress the onset of lasing on the fundamental mode.

After absorption in the laser crystal and transmission through the cavity optics, the unabsorbed 940 *nm* pump light is separated from the 1030 *nm* signal light with the aid of a 1000 *nm* long-pass reflective filter. The laser output is then collimated for further experiments and characterisation using a plano-convex lens with a focal length of 125 *mm*.

3.1.4 Characterisation

Beam Images

(A) Radially polarised mode. (B) Radially polarised mode after linear polariser, 0 degree orientation. (C) Radially polarised mode after linear polariser, 90 degree orientation.
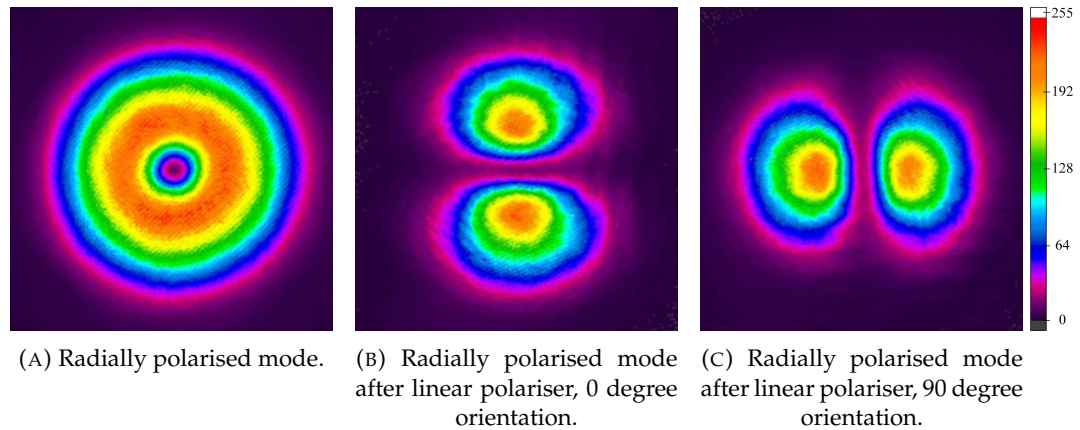
FIGURE 3.5: Intensity profile of the output radially polarised mode.

A CCD camera (Ophir Spiricon SP620U) was used to obtain images of the output mode of the radially polarised source. A false colour image of the output mode is shown in figure 3.5a. The mode is of very high quality to simple visual inspection, with a very prominent low central intensity, clear annular profile and very little discernable difference from the theoretical transverse intensity profile of a first-order radially polarised mode. Some slight imperfections in the image can be attributed to

artifacts from the CCD camera, a small amount of interference fringes due to reflections in the optical arrangement, and some airy rings from dust present in the optical path. Figure 3.5b is an image of the same mode after transmission through a linear polariser. A first-order radially polarised mode can be considered a coherent superposition of orthogonal linearly polarised HG_{01} modes. Therefore, the transmission of a perfect first-order radially polarised mode through a linear polariser should resemble the two-lobe structure of a HG_{01} mode in transverse intensity profile. Figure 3.5b shows the expected intensity profile, and is a very good visual match to a HG_{01} mode. Figure 3.5c is provided to show the same mode transmitted through a linear polariser with the polariser being rotated by 90 degrees with respect to figure 3.5b. The images of the mode were captured for an absorbed pump power of 26.5 W and an output power of 5.8 W. At absorbed pump powers below 25 W the fundamental mode became prevalent due to the weak thermal lensing strength leading to an increase in the cavity mode size, and at absorbed pump powers above 33 W the cavity became stable for the azimuthally polarised modes, which degraded the radial polarisation purity.

Polarisation Purity Measurements

Polarisation extinction ratio is easily measured for a linearly polarised mode. One simply has to use a linear polariser and a power meter, measure the power transmitted through the linear polariser as a function of polariser angle and take the ratio between the maximum and minimum power transmitted. For radially polarised beams the measurement is not quite so simple, as the same measurement would reveal that the power transmitted was invariant with polariser angle. A method to quantify the radial polarisation extinction ratio (RPER) was proposed by Smith *et al.* which is represented in figure 3.6 [172]. An image of the radially polarised mode
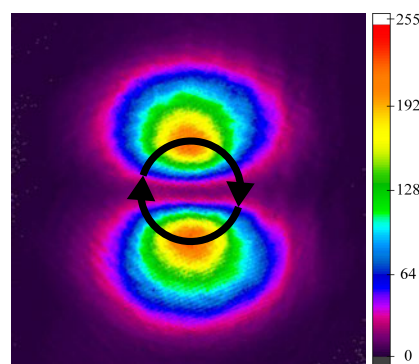
FIGURE 3.6: Representation of sampling path for the calculation of
radial polarisation extinction ratio.

is taken after transmission through a linear polariser. A computer program is then used to find the two peaks and the centre of the resulting mode. Using these, data is sampled in a circular path which is centred on the mode with a radius equal to the

average separation between the modal centre and the intensity peaks. An illustration of the circular path is shown in figure 3.6. This intensity data is then plotted as a function of azimuthal angle in figure 3.7. The data plotted in figure 3.7 shows two
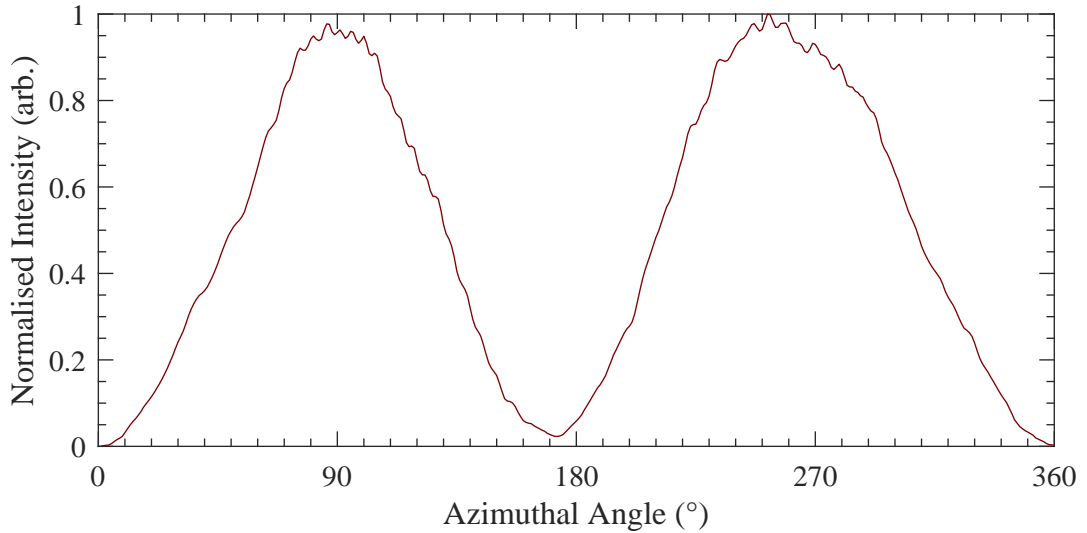
FIGURE 3.7: Normalised intensity of a radially polarised mode after transmission through a linear polariser as a function of azimuthal angle.

very clear peaks and minima which approach zero. The RPER is calculated from this data by dividing the maximum intensity by the minimum intensity. To ensure that the measurement of the RPER is accurate, this process is repeated for 36 orientations of the linear polariser, with each producing an image which was analysed by the computer program. The final RPER is obtained after averaging over all polariser orientation angles, and was measured to be 100 : 1. For a sense of scale, an experiment performed by C.R. Smith using a similar source and identical measurement technique obtained an RPER of 31 : 1 [172].

Output Power

The output power of the radially polarised source was measured as a function of absorbed pump power in order to characterise the behaviour and efficiency of the source. Figure 3.8 is a graph of the measured output power plotted against the absorbed pump power. It is clear that the radially polarised source does not have the typical power characteristics expected of a more simple solid-state laser. One might expect that after a certain pump power the laser would reach threshold, then the output power should increase linearly with respect to absorbed pump power. However, the radially polarised source has a very small band of operation for the radially polarised mode. Due to the laser cavity being designed to use thermal lensing in order to achieve stability, the slope efficiency of the laser changes with pump power. From 10 to 15 *W* of absorbed pump power we see that the laser operates with a low efficiency due to high losses in the cavity caused by a large cavity mode as the
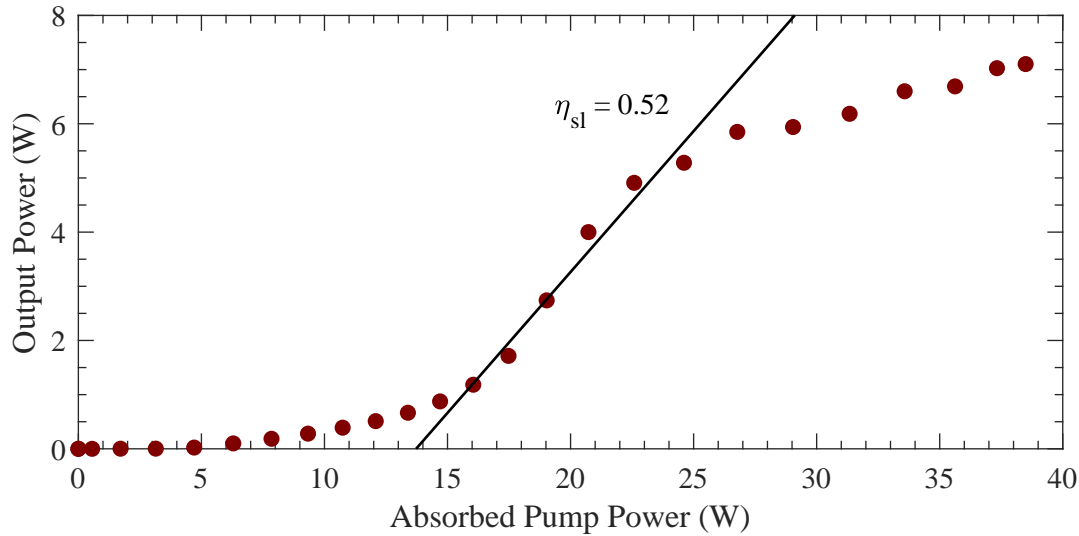
FIGURE 3.8: Output power of the radially polarised source plotted against absorbed pump power.

result of weak thermal lensing. From around 15 to 25 *W* the laser operates on the fundamental mode. This is caused by the thermal lens in the laser crystal growing strong enough to ensure that the fundamental cavity mode becomes small enough to overlap well with the pump spot. Within this region of operation we see the highest obtained slope efficiency from this source of approximately 52%. From 25 to 33 *W* of absorbed pump power the radially polarised mode dominates as the thermal lensing further decreases the cavity mode size. From 33 *W* to the maximum output of the pump source the output was a combination of first order radially and azimuthally polarised modes.

The strange power characteristics of this radially polarised mode are less than ideal, however it is important to remember that the objective for this source was to construct a radially polarised source with optimised transverse modal and polarisation purity for use in further experiments.

Beam Quality Measurements

To further quantify the radially polarised source the beam quality parameter (M^2) was measured. This measurement was performed to the ISO 11146-1:2005 standard [183]. The input pump power was set to 51.3 *W*, corresponding to an absorbed pump power of 26.8 *W*. At this pump power the radially polarised source had an output power of 5.9 *W*, which was deemed to be the optimal operating power to obtain the highest polarisation purity. The laser was allowed to operate at this power for one hour in order to reach thermal equilibrium before the M^2 measurement was attempted. A 100 *mm* plano-convex lens was used to focus the collimated and attenuated beam from the radially polarised source. Measurements of the beam diameter were taken either side of the beam waist up to three Rayleigh ranges away. The beam diameter is defined here for a higher-order mode as the second-moment width, $D4\sigma$,

where σ is the standard deviation of the intensity distribution on a given axis.

$$D4\sigma_x = 4\sigma_x = 4\sqrt{\frac{\int_{-\infty}^{\infty}\int_{-\infty}^{\infty} I(x,y)(x-\bar{x})^2 \, dx \, dy}{\int_{-\infty}^{\infty}\int_{-\infty}^{\infty} I(x,y) \, dx \, dy}} \tag{3.21}$$

where

$$\bar{x} = \frac{\int_{-\infty}^{\infty}\int_{-\infty}^{\infty} I(x,y)x \, dx \, dy}{\int_{-\infty}^{\infty}\int_{-\infty}^{\infty} I(x,y) \, dx \, dy} \tag{3.22}$$

The beam diameter was computed at each axial position using an Ophir Spiricon SP620U CCD camera and the BeamGage software published by Spiricon. The integration area was set to three times the beam radius using an iterative auto-aperture in the software. Finally, the background of the CCD camera image was substracted using the built-in software feature. The beam diameter in the x and y axes was then plotted against axial position in figures 3.9a and 3.9b. The M^2 parameter is cal-

(A) Sagittal axis.
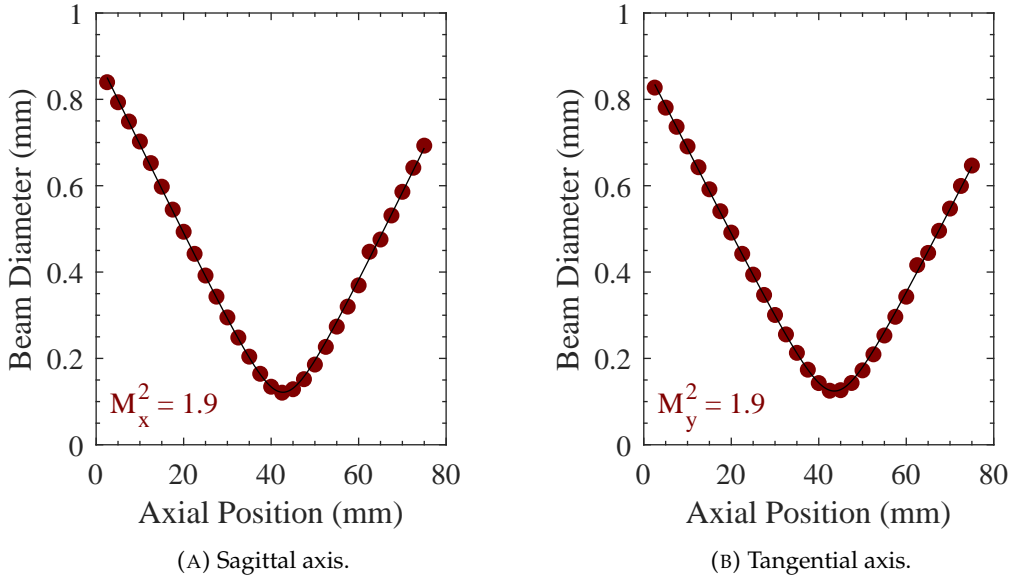
(B) Tangential axis.

FIGURE 3.9: Beam quality parameter measurements for the radially polarised source in sagittal (x) and tangential (y) axes.

culated for each beam axis by fitting the following polynomial to the data using a least-squares regression algorithm.

$$D4\sigma(z) = \sqrt{az^2 + bz + c} \tag{3.23}$$

Finally, the M^2 values may be calculated using the polynomial coefficients

$$M^2 = \frac{\pi}{8\lambda}\sqrt{4ac - b^2} \tag{3.24}$$

where λ is the central laser wavelength. The beam quality parameters were measured as $M_x^2 = 1.9 \pm 0.1$ and $M_y^2 = 1.9 \pm 0.1$, which are a quantification of the excellent purity and quality of the radially polarised mode. The theoretical minimum

M^2 of the targeted first-order radially polarised mode is 2.0. Although it may seem strange that the M^2 measured for the radially polarised source is below 2.0, it is possible that this is due to the presence of some component of the fundamental mode, which distorts the values towards 1.0. A more likely explanation is experimental uncertainty, as the measured value is within error bounds of the theoretical minimum M^2.

3.1.5 Summary

A 1030 *nm* Yb:YAG radially polarised source was constructed which utilised a capillary pump delivery fibre and thermally induced birefringence to output a mode which was optimised for quality and polarisation purity. The modal output was optimal at an output power of 5.9 *W*, which was deemed sufficient to use as a seed source for further experiments investigating the amplification of a radially polarised mode. While the power characteristics of the radially polarised source were less than desirable, this was not the purpose of the source. The quantitative highlights of the radially polarised source were the measured M_x^2 and M_y^2 of 1.9 and the radial polarisation extinction ratio of 100:1.

3.2 Laguerre-Gaussian Vortex Mode Source

This section reports on the design, construction and results from a Laguerre-Gaussian vortex mode source based on a first order Hermite-Gaussian mode laser with a double pump source and a spherical mirror mode converter. The aim of this source was to create an end-pumped solid-state laser with optimised mode quality for the LG_{01} mode which possesses both a 'vortex phase' and orbital angular momentum (OAM), to use as a seed source in order to investigate possible amplification methods. This section first begins with the design of a 1030 *nm* linearly polarised HG_{01} Yb:YAG laser which was pumped with two fibre-coupled diode lasers where the pump delivery fibres are placed and imaged in such a way to optimise the overlap with the desired transverse mode. The theoretical understanding behind a spherical mirror mode converter first developed by R. Uren [184] is explained and results are included for its use in converting the HG_{01} mode into a LG_{01} mode with OAM.

3.2.1 Double Pump-Spot Hermite-Gaussian Laser

In order to generate an LG_{01} mode using the mode converter method one must first generate a high-purity HG_{01} mode. This has not been an active area of research, as the uses of such modes are limited, however previous approaches to obtain the HG_{01} mode have used intra-cavity thin wires [21, 185], off-axis pumping [186, 187] or even deliberate misalignment of the cavity mirrors in a fundamental mode laser. These approaches have the significant drawbacks of low efficiency, mode impurities, and the use of loss inducing elements. In this work a design introduced by Uren and Liu

[102, 188] which uses two pump spots from fibre-coupled diode lasers in order to shape the gain is used in order to produce a HG_{01} mode. Modal purity is obtained by virtue of the overlap between the pump and cavity mode distributions being high for the HG_{01} mode and low for other modes that might otherwise contribute to impurities. This work is slightly different from this previous work in the approach used to position the pump beams, although the main aim was to create a robust, high purity source in order to trial amplification methods.
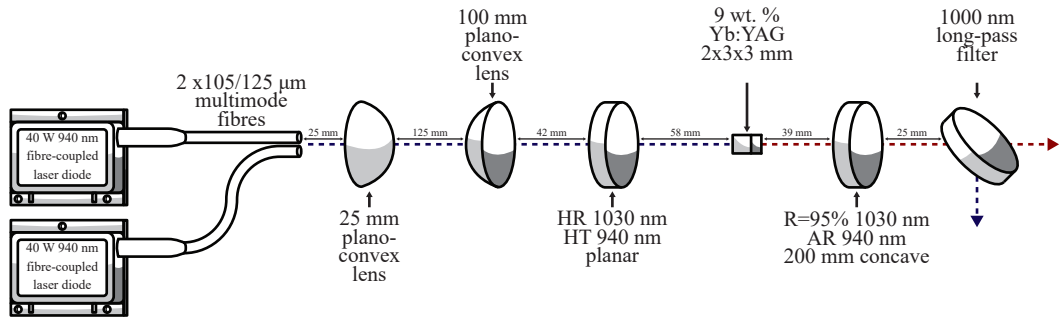
FIGURE 3.10: Schematic of the double pump-spot 1030 nm HG_{01} Yb:YAG laser

The experimental configuration of the HG_{01} mode source is shown in figure 3.10. The source is built using a simple two-mirror plano-concave cavity. The planar input coupler is highly reflective at the laser wavelength (1030 *nm*) and highly transmissive at the pump wavelength (940 *nm*). The output coupler is concave with a 200 *mm* radius of curvature; it has a reflectivity of 95% at 1030 *nm* and is highly transmissive at the pump wavelength. The cavity length was 100 *mm*. The gain medium was a cuboid 9 *wt*.% Yb:YAG crystal with dimensions of $2 \times 3 \times 3$ *mm*. This crystal was used due to availability; a more optimal crystal would have a lower dopant concentration and greater length in order to mitigate thermal effects. The Yb:YAG crystal was positioned such that the separation from the input coupler was 58 *mm*.

The pump sources used for this laser were two 40 *W* 940 *nm* commercial fibre-coupled laser diodes (nLight Inc.). The pump-delivery fibres from these diodes were multimode with core diameters of 105 *μm*, cladding diameters of 125 *μm* and an NA of 0.22. Using the core diameters of 105 *μm* and assuming imaging with a magnification of 1.0, R. Uren *et al.* found experimentally that in order to ensure the optimum overlap between the two pump-spots and the HG_{01} mode that the separation between the pump spot centres should be approximately 200 *μm* to give the correct ratio between the spot diameter and separation [102]. In their experiment the pump beams were imaged onto opposite faces of a knife-edge prism in order to obtain co-linear pump beams. The individual pump spots could be moved with the aid of kinematic opto-mechanics. After this ratio had been experimentally obtained the requirement to have the separation between the pump spots be adjustable was no longer necessary, allowing for a more simple design with fewer components and moving parts. Q. Liu recreated the experiment by bonding the cleaved ends

of the pump delivery fibres to an anti-reflection coated silica substrate by using a CO_2 laser to heat the substrate before pushing the fibres onto the hot surface. The co-linear pump beams were then imaged into the laser crystal with the required magnification in a normal end-pumping approach. This had the benefit of having no moving parts and a more simple set-up. However, successfully bonding two fibres with the required separation and implementing the fragile result into a laser proved non-trivial.

A much easier way of implementing the double pump-delivery fibre method was to exploit the conveniently dimensioned polymer coating on the outside of the fibres. The outer diameter of the polymer coating on most $105/125\mu m$ pump delivery fibres is approximately 250 μm and in modern commercial fibre is well-toleranced and uniform. The thickness of this polymer layer is therefore approximately 62.5 μm from the edge of the outer cladding to the surface of the polymer layer. Fortunately, the required optimal separation between the edges of the outer claddings in the two pump delivery fibres is approximately 60 μm. Put simply, if one strips the polymer coating from only one of the pump delivery fibres, then aligns the two fibres such that they are co-linear and touching, the fibre ends will be positioned with approximately the optimal separation between the centres of 200 μm. Experimentally this was achieved by stripping the polymer from the majority of the length of one pump delivery fibre, and only the very tip of the other fibre, then placing both fibres in a v-groove. Figure 3.11 is an optical microscope image of the pump delivery fibres from two diode lasers positioned in this way. The end-view of the two fibres positioned in this way is shown in figure 3.12. The outputs from the two pump delivery
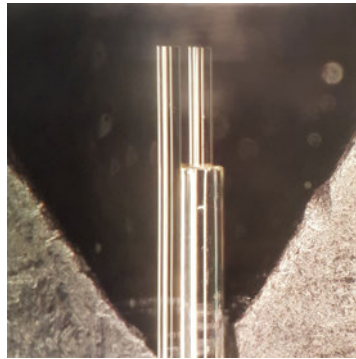
FIGURE 3.11: Microscope image of the two pump-delivery fibres used in the HG_{01} source, illustrating the use of polymer cladding as a separation aid.

fibres were imaged into the centre of the laser crystal using a 25 mm and a 100 mm plano-convex lens in a 4f telescope arrangement. This gave a magnification factor of 4, meaning that the two pump spots each had an imaged diameter of 420 μm and their centres were separated by approximately 800 μm. This large pump-spot size was chosen to mitigate against the severe thermal lensing effects that were present in the laser crystal.
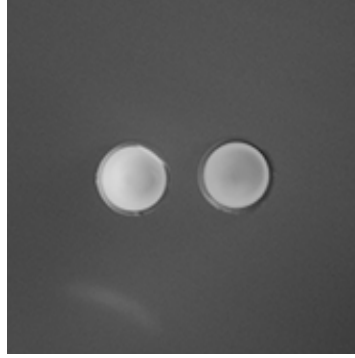
FIGURE 3.12: End-face view of two 105/125 μm pump delivery fibres positioned with a separation of 60 μm between the outer surfaces. Image courtesy of Q. Liu.

CCD camera images of the transverse intensity profile of the output of the HG_{01} source are shown in figure 3.13a and 3.13b for low and high power operation respectively. At 210 mW output power the result is a high quality HG_{01} mode that

(A) 210 mW

(B) 2.5 W
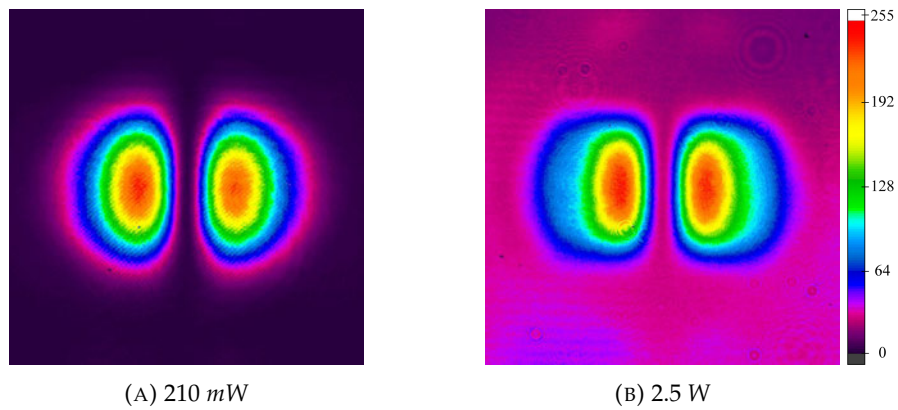
FIGURE 3.13: Intensity profile of the output HG_{01} mode at low and high power.

very strongly resembles the theoretical intensity distribution. However, at an output power of 2.5 W the mode shown in figure 3.13b exhibits clear distortions. This was due to the significant thermal lens present in the cuboid laser crystal. This geometry manifests both as a distortion of the output to a more rectangular profile, and as the introduction of modal impurities.

3.2.2 Spherical Mirror Mode Converter

The output from the HG_{01} source can be converted to an LG_{01} mode with the aid of a mode converter. This concept relies on the use of optical elements to introduce specific phase delays between constituent modes in order to coherently combine them into other transverse modes [20]. This approach was first used by Beijersbergen *et al.* to generate an LG_{01} mode with spiral phase and OAM from a HG_{01} mode [21]. The paper showed that in general, a HG_{nm} mode may be converted to an LG_{pl} mode

of the same order, N where N is defined as

$$N = m + n = 2p + l \tag{3.25}$$

and the mode orders in an LG mode relative to those in a HG mode are

$$p = min(m,n), \quad l = n - m. \tag{3.26}$$

The amplitude of a HG_{nm} mode and LG_{nm} are given as

$$
\begin{aligned}
u_{nm}^{HG}(x,y,z) = &\frac{1}{w} C_{nm}^{HG} H_n \left(\frac{x\sqrt{2}}{w} \right) H_m \left(\frac{y\sqrt{2}}{w} \right) \exp \left(\frac{-ik(x^2 + y^2)}{2R} \right) \\
&\cdot \exp \left(\frac{-(x^2 + y^2)}{w^2} \right) e^{-i(n+m+1)\psi}
\end{aligned}
\tag{3.27}
$$

$$
\begin{aligned}
u_{nm}^{LG}(r,\phi,z) = &\frac{1}{w} C_{nm}^{LG} (-1)^{min(n,m)} \left(\frac{r\sqrt{2}}{w} \right)^{|n-m|} L_{min(n,m)}^{|n-m|} \left(\frac{2r^2}{w^2} \right) \\
&\cdot \exp \left(\frac{-ikr^2}{2R} \right) \exp \left(\frac{-r^2}{w^2} \right) e^{-i(n+m+1)\psi} e^{-i(n-m)\phi}.
\end{aligned}
\tag{3.28}
$$

In these expressions, $H_n(x)$ is the nth order Hermite polynomial, L_p^l the generalised Laguerre polynomial, k, w and R are the wavenumber, beam radius and wavefront radius of curvature respectively, which are all functions of z. C_{nm}^{HG} and C_{nm}^{LG} are normalisation constants given by

$$C_{nm}^{HG} = \left(\frac{2}{\pi n! m!} \right)^{1/2} 2^{-N/2}, \quad C_{nm}^{LG} = \left(\frac{2}{\pi n! m!} \right)^{1/2} min(n,m). \tag{3.29}$$

The final parameter to define in these expressions is of special importance in these experiments. The Gouy phase shift, ψ, in terms of the Rayleigh range z_R is

$$\psi(z) = \arctan \left(\frac{z}{z_R} \right). \tag{3.30}$$

LG modes may be expressed as being composed of HG modes of the same order N:

$$u_{nm}^{LG}(x,y,z) = \sum_{k=0}^{N} i^k b(n,m,k) u_{N-k,k}^{HG}(x,y,z) \tag{3.31}$$

where b is a real coefficient given by [184]

$$b(n,m,k) = \left(\frac{(-2)^k (-1)^k}{2^k k!} \right) \frac{d^k}{dt^k} [(1-t)^n (1+t)^m]_{t=0} \tag{3.32}$$

The interesting effect which can be exploited by an astigmatic mode converter is the inclusion of the i^k term in the decomposition of an LG mode which is not present in

the same decomposition of a *HG* mode aligned at 45° to the *x* and *y* axes.

$$u_{nm}^{HG}\left(\frac{x+y}{\sqrt{2}},\frac{x-y}{\sqrt{2}},z\right) = \sum_{k=0}^{N} b(n,m,k)u_{N-k,k}^{HG}(x,y,z) \qquad (3.33)$$

This i^k terms equates to a $\pi/2$ phase difference between successive components in the decomposition of the mode for the *LG* case. Figure 3.14 shows this relationship pictorially. In the converse case to the decomposition, the coherent combination of
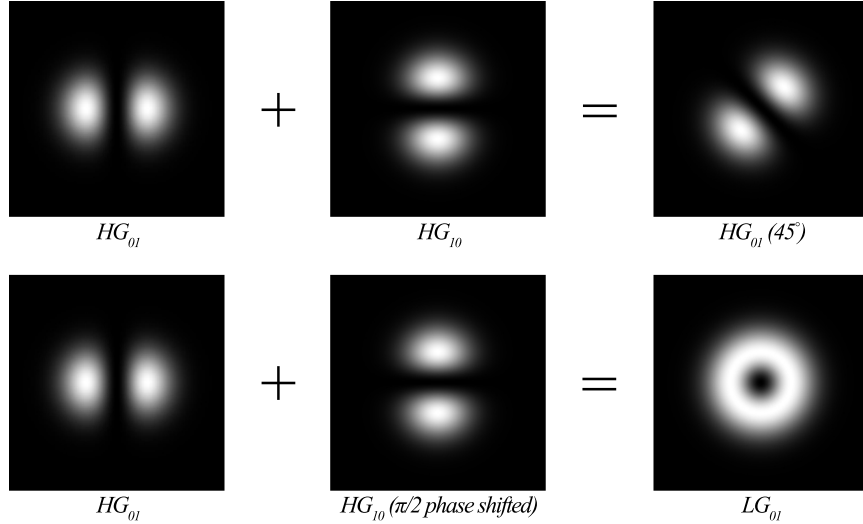
FIGURE 3.14: The coherent combinations of HG_{01} and HG_{10} modes in phase and again with a $\pi/2$ phase shift between the modes.

a HG_{01} and a HG_{10} mode with no phase difference is a 'HG_{01}' mode at 45° to the transverse axes. Due to the i^k term, the coherent combination of a HG_{01} and a HG_{10} with a $\pi/2$ phase difference between the constituents is a 'spiral phase' LG_{01} mode. An astigmatic mode converter takes a HG_{01} mode at 45° and applies this phase shift to one of the components. Recall the Gouy phase shift given in equation 3.30; this is an often ignored term which applies a phase shift to a beam as it passes through a focus. However, by ensuring that the axes of a HG_{01} mode at 45° are focussed to different waists, they will have a different z_R and therefore a different Gouy phase shift. By carefully selecting appropriate astigmatic optics, one can set this phase difference between the constituent modes to the required $\pi/2$. The astigmatism introduced must be then removed after successful conversion in order to prevent futher phase changes in the output mode.

Beijersbergen *et al.* chose to use a pair of cylindrical lenses in their experiment, and were able to convert a HG_{01} mode to a LG_{01} mode in this way [21]. Uren *et al.* advanced the technique by using spherical mirrors at an angle θ to the beam propagation axis in order to introduce astigmatism. This had the advantages of mirrors having higher damage thresholds for high peak power applications and usually suffering from fewer optical imperfections than cylindrical lenses. The following expressions were used to recreate their experiment in order to produce a high quality

LG_{01} spiral phase mode. For a full derivation consult [102]. For two identical spherical mirrors with radius of curvature R_c, at an angle θ with respect to the beam, the required separation between the mirrors is

$$2d = \frac{R_c}{\sqrt{2}\sin(\theta)\tan(\theta)}. \tag{3.34}$$

In order to obtain the correct phase difference between the constituent modes, the incident HG_{01} mode must be orientated at $45°$ to the axis of the rotation of the mirror. Upon contact with the first mirror it must have a fundamental mode radius of

$$w(d) = \left(\frac{2\sqrt{2}\lambda d}{\pi}\right)^{1/2} \tag{3.35}$$

and a radius of curvature

$$\frac{1}{R} = \frac{1}{2d\left(2+\sqrt{2}\right)} - \frac{R_c}{2\cos(\theta)}. \tag{3.36}$$

3.2.3 Experimental Configuration

The conditions for the input to the mode converter are very specific and requires careful magnification and experimental design to avoid distortions in the output mode. Two concave mirrors, highly reflective at 1030 *nm*, with a radius of curvature of 150 *mm* were used to make up the mode converter. The first mirror introduces the astigmatism between the constituent modes of the input, while the second mirror serves to undo this astigmatism and produce a stigmatic beam. For these mirrors at an angle $\theta = 45°$ relative to the incident beam the required separation between them is calculated from equation 3.34 to be 150 *mm*. Using these parameters, a HG_{01} mode at a wavelength of 1030 *nm* should have a fundamental beam radius at the first mirror of 264 *μm* and a radius of curvature of -134 *mm*. The beam waist in the HG_{01} source was positioned at the input-coupler, and was measured to be 181 *μm* in terms of the embedded fundamental mode (as defined in section 2.1.5). A number of lens arrangements were trialled in order to attempt to obtain the correct beam radius and curvature at the first mirror of the mode converter. It was found that a highly flexible arrangement was required due to slight differences from the ideal parameters produced highly distorted beams from the mode converter. Figure 3.15 shows the set-up which eventually successfully produced a high quality converted LG_{01} mode. The reduced-opacity optics on the far left of figure 3.15 represent the cavity of the HG_{01} source and pump separation optics in an effort to convey the position of the beam waist, which is marked w_0 and with a red cross. A 125 *mm* plano-convex lens was placed 250 *mm* from the beam waist. A dove prism was used to rotate the HG_{01} mode to the required angle relative to the x and y axis. The first mirror of the mode converter was placed 296 *mm* from the lens at a position calculated to give the
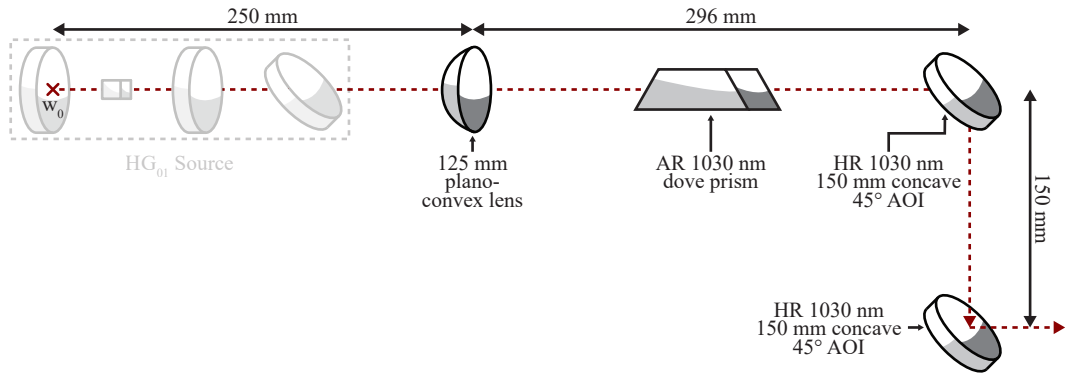
FIGURE 3.15: Schematic of the spherical mirror mode converter used
to obtain a LG_{01} mode from a HG_{01} input.

optimal beam radius and curvature using Gaussian beam propagation equations. The second mirror of the mode converter was placed 150 *mm* from the first mirror at the same angle of incidence to the beam as the first mirror. The mode converter was adjusted in order to optimise the transverse intensity profile of the output mode by slight variations ($< 2\,mm$) of the distance of the focusing lens to the cavity waist, the separation of the mode converter to the cavity lens and the separation of the mirrors of the mode converter.

3.2.4 Characterisation
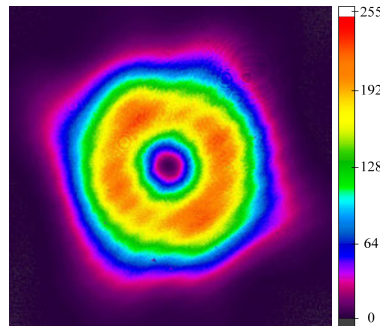
FIGURE 3.16: Intensity profile of the output LG_{01} mode from the
mode converter.

The intensity profile of the output mode from the spherical mirror mode converter is shown in figure 3.16. The output is a clear LG_{01} mode with minor impurities. The mode has a very low intensity central region, which means that there is likely very little fundamental mode impurity present, and has low astigmatism and good overall symmetry. The horizontal lines present on the image are unfortunately interference fringes from the imaging optics, but do not reflect negatively on the quality of the obtained mode. The largest of the defects present within the image are the 'spokes' - four regions of intensity protruding slightly from the mode. These are likely caused by thermal lensing within the laser crystal. Although this image was taken with the HG_{01} source operating at a low power of 210 *mW* the thermal lensing

effects are still present. The thermal lensing became such a problem at high power from the HG_{01} that the mode converter did not produce a recognisable mode. This is partly due to the thermal lens in the laser crystal changing the imaged beam waist and curvature to the mode converter in an unpredictable way, but also a symptom of the susceptibility of the mode converter to modal impurities in the input. Future sources of this design could make use of a different gain medium geometry, such as a thin-disk, in an effort to reduce this thermal lensing.
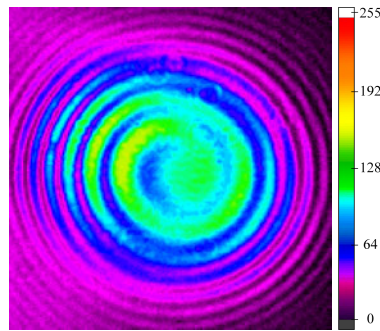
FIGURE 3.17: A Mach-Zehnder interferometer revealed spiral interference fringes demonstrating the presence of vortex phase in the LG_{01} beam from the mode converter.

The vortex phase of the LG_{01} source was the purpose of the construction of this source and mode converter. In order to establish whether or not the output mode did indeed possess this property a Mach-Zehnder interferometer was used [104]. The collimated output of the mode converter is split using a beam-splitter. One of the beams is passed through a pinhole in order to diverge the beam and create a spherical wavefront. The beams are then recombined. If the output from the mode converter has vortex phase, the interferogram produced from the Mach-Zehnder interferometer should be a spiral. Figure 3.17 is a CCD camera image of the interferogram from the Mach-Zehnder. There is a very clear spiral present which means that the obtained mode had some degree of vortex phase. The direction of the spiral also reveals the handedness of the spiral phase. It should be noted however that one of the benefits of the astigmatic mode converter design is the ability to choose the handedness of the output LG_{01} mode by changing the angle of the incident HG_{01} mode from $45°$ to $-45°$.

The output power of the HG_{01} source and the LG_{01} output from the mode converter was measured as a function of the absorbed pump power. The fraction of power that was lost during propagation through the mode converter was measured to be within the error on the detectors and therefore negligible. Figure 3.18 is a graph of the output power from the mode converted source as a function of the absorbed pump power. The slope efficiency was measured as 57% up to an absorbed pump power of 7.6 *W*. This was slightly above expectations due to the sub-optimal gain medium, and therefore could be excellent for a source of the same design with a gain medium geometry with better thermal handling. Thermal problems typical of a laser crystal rod become apparent above 8 *W* of absorbed pump power. The output power
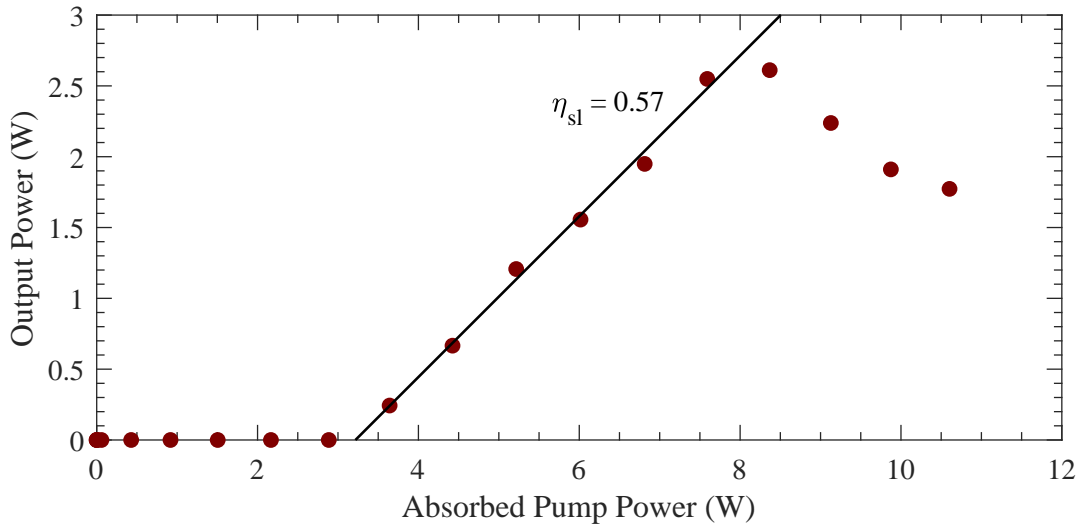
FIGURE 3.18: Output power of the LG_{01} mode source plotted against the absorbed pump power.

here begins to decrease with absorbed pump power due to the significant thermal lensing changing the cavity mode size, decreasing the overlap with the pump and likely causing significant depolarisation. Another negative was the relatively high threshold absorbed pump power of 2.5 *W*, which is again likely due to the highly doped laser crystal needing a high pump power in order to reach transparency. Although the combined available pump power of the diodes was 80 *W*, this power was unable to be used as it was deemed likely to cause damage to the laser crystal.

3.2.5 Summary

A 1030 *nm* Yb:YAG LG_{01} mode source with spiral phase was constructed. The initial source operated on the HG_{01} mode, which was targeted by placing the pump delivery fibres of two fibre-coupled laser diodes to be co-linear and separated from core-to-core by 200 *μm*. The output was an excellent HG_{01} mode at low powers, but the mode deteriorated at high pump powers due to significant thermal lensing. A spherical mirror mode converter was used to convert the HG_{01} source to a LG_{01} mode. The mode converter used the astigmatism from oblique angle reflections from two spherical mirrors in order to exploit the Gouy phase shift from a focus and introduce a phase delay between constituent modes in the incident HG_{01} mode to obtain a LG_{01} output. The LG_{01} result was a good match to a theoretical intensity profile and had clear spiral phase as evidenced by the interferogram from a Mach-Zehnder interferometer. The source had decent power characteristics up to a certain pump power with a slope efficiency measured at 57%. However, the threshold absorbed pump power was high at 2.5 *W* and the output power of the slope deteriorated rapidly with increasing pump power due to significant thermal effects in the laser crystal.

Chapter 4

Machine Learning for Transverse Laser Mode Analysis

During the development of the higher-order mode sources in this thesis the question "How good is my mode?" was encountered frequently. In most experimental higher-order mode systems the sources are constructed by visually optimising the output mode and quantified after using such metrics as the beam quality parameter $\left(M^2\right)$ and polarisation extinction ratio. This is not ideal as visual optimisation is subjective, therefore such sources would greatly benefit from a quantified real-time metric for optimisation. In addition, the solid-state lasers in this work are susceptible to thermal lensing and modal competition; the laser may be optimised at one power level but the cavity and modal composition effectively changes as the pump power is increased or decreased. Fundamental mode lasers can be engineered to be robustly single mode over a range of pump powers, while linearly polarised lasers can deliver a variable output power through the use of a waveplate and a polariser, which mostly circumvents this problem. For a radially polarised laser this isn't possible, therefore it is common to see evidence of undesired modal impurities in these sources.

The M^2 parameter has become almost ubiquitous in the literature, as it enables an easy direct comparison between fundamental mode sources if a common standard is followed. Real-time measurement of the M^2 is achievable through the use of Rayleigh scattering [189] and multiple axial position sampling [190] and $\sim 20\ Hz$ measurement frequencies are available from off-the-shelf commercial products [191]. While M^2 is a decent metric for optimising fundamental mode sources, the M^2 alone is not sufficient to optimise the transverse modal composition of a higher-order mode laser. For a multimode Hermite-Gaussian beam with modes of order n, m where the normalised modal composition coefficients C_{nm} satisfy $\sum_{n,m}|C_{nm}|^2 = 1$ the M^2 is given by Siegman [17] as

$$M_x^2 = \sum_{n=0}^{\infty} \sum_{m=0}^{\infty} (2n+1)\,|C_{nm}|^2 \quad \text{and} \quad M_y^2 = \sum_{n=0}^{\infty} \sum_{m=0}^{\infty} (2m+1)\,|C_{nm}|^2 \tag{4.1}$$

and for a combination of Laguerre-Gaussian modes of order p, l the M^2 is

$$M_r^2 = \sum_{p=0}^{\infty} \sum_{l=-p}^{p} (2p + l + 1) |C_{pl}|^2 \tag{4.2}$$

Figure 4.1 uses these expressions to visually demonstrate that entirely different modal compositions can have identical M^2 values. One image is of a pure LG_{01} mode, which has an M^2 of 2.0, while the other image is an incoherent combination of approximately 66% LG_{00} and 33% LG_{03}, which has a vastly different intensity profile yet identical M^2. A different metric is therefore needed in order to optimise the output of a higher-order mode solid-state laser.

100% LG_{01} 66% LG_{00}, 33% LG_{03}
$M^2 = 2.0$ $M^2 = 2.0$
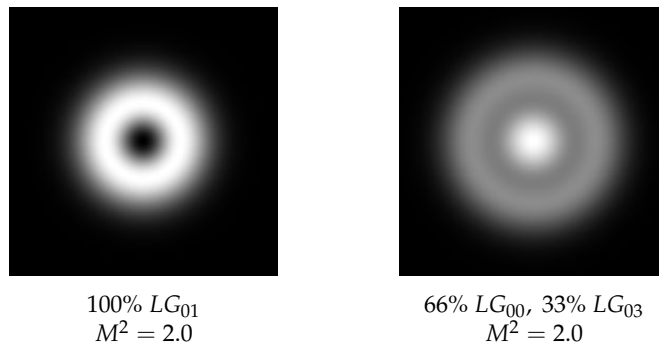
FIGURE 4.1: Theoretically generated single and multimode intensity profiles with identical M^2 values.

Modal decomposition provides a metric which would be suitable for optimisation of the output of a solid-state laser. Modal decomposition has previously been shown to: enable adaptive mode control [192, 193], mode resolved gain [194, 195] and bend-loss [196], optimise fibre to fibre coupling [197] and to diagnose transverse mode instability [198, 199]. Several experimental techniques have been developed to analyse modal composition in recent years, including spatially and spectrally resolved imaging (S^2) [200], frequency domain cross-correlated imaging (C^2) [201], ring resonator based approaches [202], interferometry [203], optical correlation filters [204] and digital holography [205]. While these techniques can all achieve accurate modal decomposition they require non-trivial experimental set-ups or post-processing of data. For example, S^2 imaging requires the use of a broadband source and an optical spectrum analyser, or alternatively a tunable laser and CCD camera. While these techniques have merits such as the ability to measure polarisation states [202], the complexity, intrusiveness and specialised nature of these experimental based methods makes them unattractive for use as a development aid for higher-order mode sources.

Numerical methods of modal decomposition remove the requirement for complex and sometimes bespoke experimental arrangements, and have been shown to be able to achieve more than satisfactory accuracies [206]. Gerchberg-Saxton algorithms [207] have been used in modal decomposition [208] with a benefit that the

computation time is independent of the number of modes to be decomposed. However Gerchberg-Saxton is an iterative approach with convergence times on the order of hundreds of seconds, which precludes their use for real-time modal decomposition. Line search methods [206] seek to minimise an error function such as the residuals between the observed laser beam and a beam reconstructed from modal coefficients. These line search methods update modal coefficients, converging in times of the order of a second, with convergence times increasing exponentially with the number of modes [206]. In addition, line search methods can be vulnerable to finding local minima and their success can depend strongly on the initial values. Genetic algorithms also deserve a mention as a possible numerical modal decomposition method, however their computation time is slow in comparison with other methods [209]. Stochastic parallel gradient descent (SPGD) algorithms have a similar working principle to line search methods, but have reduced computation times and are less susceptible to local minima and initial conditions owing to the stochastic nature of their optimisation. SPGD algorithms have been used to analyse modal composition with a frequency of approximately 9 *Hz* [210], which is fast compared to the other techniques mentioned, yet still slow compared to the timescales over which a transverse laser mode might vary.

A Convolutional Neural Network (CNN) is an image recognition method which has often been referred to as an 'artificial intelligence', 'machine learning' or 'deep learning' technique. There has been an explosion in interest in the use of CNNs in recent years, fuelled by the results of the 2012 ImageNet competition. A CNN was able to almost halve the error rates of the next best competition [211]. As a CNN relies on the association of an image with an ascribed characteristic through a training process, it is possible to achieve estimates of system properties from observed phenomena despite the system being complex or nonlinear. In addition, computation times are extremely fast, as CNNs make heavy use of parallel computing resources such as graphics processing units (GPUs) while returning a result with only a single forward pass through the network. For this reason, CNNs have been applied to many topics within optics within a short space of time, such as laser mode-locking [212], imaging through scattering media [213, 214], microscopy [215] and coherent beam combination [216]. The modal decomposition of a waveguide [217], a fibre [218] and a solid-state laser [219] has been demonstrated with a CNN with the latter a result from the work in this thesis. The computation time of modal decomposition using a CNN has been shown to be < 0.1 *ms*, independent of the number of modes, which represents a three order of magnitude improvement over the previous fastest method.

4.1 Convolutional Neural Networks

Machine learning is seeing increasing use in every day life and can be found in applications such as in smartphones, speech recognition, search engines, and self driving

cars. Prior to the widespread adoption of machine learning algorithms these applications required laborious programming, which required a good deal of expertise to implement algorithms that were limited in scope. Besides this ease of implementation, the use of machine learning approaches often provide increased speed and accuracy.

Neural networks belong to a class of machine learning that is often referred to as 'Deep Learning'. Deep learning is a form of representation learning that allows a computer to be fed raw data and labels and automatically discover the features that represent each label. These algorithms rely on successive transformations that act on raw data to reveal features, with the representation of features becoming more abstract deeper in the network. The 'Deep' descriptor refers to the large number of these successive transformations (layers) and therefore a hierarchical depth of feature extraction. The layers of a deep neural network are linked using weighted connections in a way that is reminiscent of neural connections, hence the sobriquet.

For a typical CNN, the upper levels are made of two types of layers - convolution and pooling. In a convolution layer, n learned filters of a size (i, j, k), where i, j are the width and height and k is the number of channels, are convolved with the input array with the filters moving across the array by a stride distance l. The convolution of the input with these filters produces n feature maps, arrays that contain the activations of the convolution between the input and filters. The convolution layer is normally followed by a non-linearity, of which the most commonly used is the rectified linear unit (ReLU). The ReLU function is simply $f(x) = max(x, 0)$. A batch normalisation layer can be included between each convolution and ReLU layer as a 'hidden' layer; its function is a subtraction of the mean and division by the standard deviation of a batch of training data. The batch normalisation speeds up the training process and reduces the sensitivity of the network to initial conditions. The output of the previous layers is then downsampled in a pooling layer. The main purpose of a pooling layer is to collate similar features, that may be otherwise variant through position or distortion, into motifs. This is achieved by essentially coarse-graining the positions of features. A pooling layer might operate by outputting the maximum of a group of units in an array before moving on to another group in a striding operation. The conv - ReLU - pool sequence is repeated a number of times through the middle layers of the CNN, with the optimal network depth being dependent on the application. The final layers of a CNN include fully-connected layers. In a fully-connected layer the input array is multiplied by a weighted matrix and a bias is added. This forms the 'brain' of the network due to the large number of learned weighted connections to previous layers. A dropout layer might be included as the next layer. The purpose of a dropout layer is to randomly set inputs to zero with a defined probability in order to aid in the prevention of over fitting the network during training. Finally, the output of the CNN comes from an activation layer. This is a function that returns an output vector, prediction or categorisation.

For a demonstration of the function of the early layers of a CNN a 120×120

(A) 120×120 pixel image of Pearl the cat.

(B) 58×58 pixel visualisation of the activation of a channel after the 5th layer of the CNN.

(C) 27×27 pixel visualisation of the activation of a channel after the 9th layer of the CNN.

(D) 11×11 pixel visualisation of the activation of a channel after the 13th layer of the CNN.
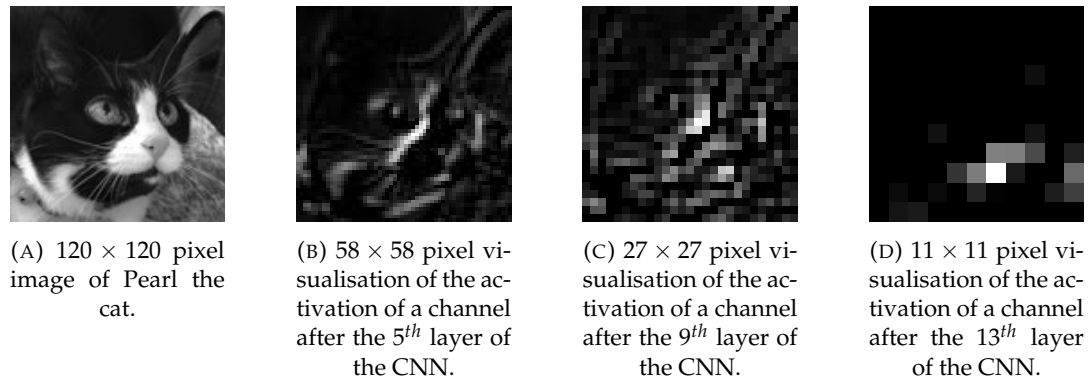
FIGURE 4.2: Visualisation of the working concept of a CNN. An image of a cat was input into the CNN. Channels were selected from the 5th, 9th and 13th layers to illustrate the increasing abstraction of feature recognition in deeper layers of the network.

pixel 8-bit greyscale image was used as an input to a trained CNN. Figure 4.2a is the original image of Pearl the cat that was used as the input. The initial activations displayed in the feature maps in the very early layers of a CNN are usually low level features such as edges. The actual activation depends on the filter used and may indicate for example, edges in a certain orientation, or transitions from high to low or vice versa. Figure 4.2b is a visualisation of one of the feature maps extracted from the 5th layer of the CNN. This feature map seems to be identifying edges in a diagonal orientation, with Pearl's ears and diagonal boundaries between her light and dark markings returning a high output. As one progresses deeper in the network the features are gathered into motifs, although they become less visually recognisable due to the abstraction of the feature maps. In Figure 4.2c we can see that in an activation in the 9th layer of the CNN Pearl is barely recognisable. Instead the CNN has further identified collections of edges forming the light patch around her nose. Finally, in the layer before the fully-connected layers, Figure 4.2d shows an activation that is maximal around the cat's nose. The CNN has detected the presence and shape of the continuous bright patch from the original image. This was unsurprising, as the CNN used to create the figure was trained in laser mode identification, therefore shaped bright regions of an image will lead to high activations.

Imagine we wanted to instead train a CNN to be able to recognise an image of a cat from other animals. The first step is to collect a large number of images of animals, including sufficient examples of cats, which are labelled with their true contents. We then create a CNN, which may be original, or it may adapt a pre-trained network in a process known as transfer learning. The output layer of the CNN is set to a classification layer with a number of elements equal to the number of possible animals. The weights of the CNN are then optimised using a training process. In the training process, the computer is shown an image and it returns a vector of scores for each of the possible image contents. It is unlikely at the start of the training process that the computer has returned a high score for the cat category. In supervised learning, the error function between the predicted scores and true

score is computed. During the training the computer adjusts the weights of the network to minimise the error function. In a typical deep learning application there may be millions of weights to adjust, and thousands of labelled example images to train with. An optimisation algorithm such as Stochastic Gradient Descent (SGD) or Adam (adaptive moment estimation) is usually used to adjust each weight to find a global minimum. The same approach to image recognition was used to create a CNN that was able to make predictions of modal composition.

4.2 BeamNet

Some of the best known image recognition CNNs such as Alexnet [211] and VGG-16 [220] have relatively large networks with 16 or more convolutional layers. The structure is optimised for three channel (full colour) images with highly diverse contents. Intensity based camera images of transverse laser modes are greyscale, meaning they only have a single channel of information, and have simple contents made up of various shaped intensity patterns. While the simultaneous research on this topic by An *et al.* [218] chose to modify the existing VGG-16 network, a smaller, more simple network was expected to deliver faster computation and training times while achieving similar accuracy. Therefore, a bespoke network designated *BeamNet* was created using the *MATLAB*® language. The structure of BeamNet is represented in figure 4.3. First of all, the input layer accepts single channel (greyscale) images with dimensions of 120×120 pixels; this resolution was chosen to match the FLIR Lepton®camera, but can be set arbitrarily. The second layer is a convolution layer, where eight 5×5 pixel filters are convolved with the input image. A ReLU layer is next, followed by a two-dimensional maximum pooling layer with a pooling region
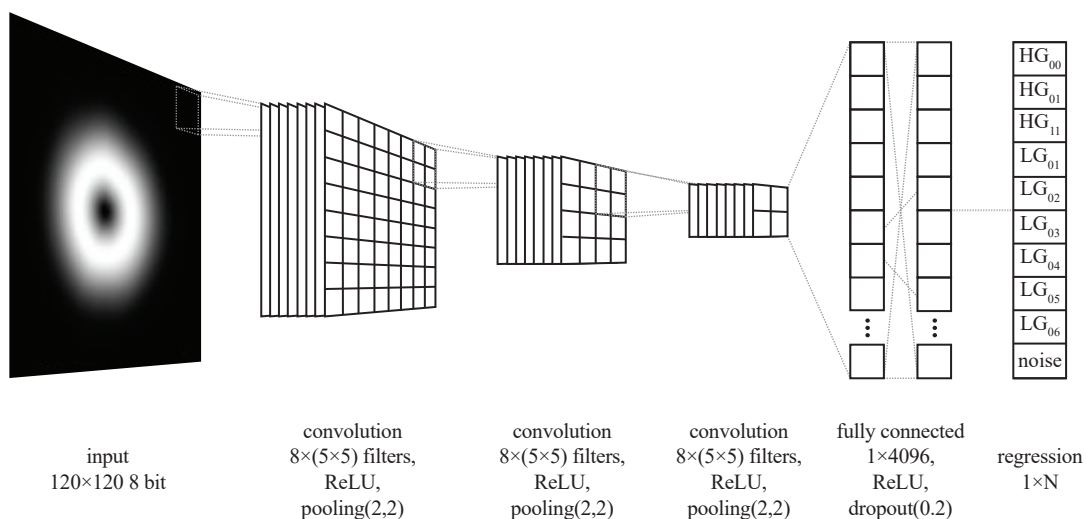
FIGURE 4.3: Visualisation of the BeamNet CNN structure

size of two units and a stride length of two. This pattern of convolution-ReLU-pooling is repeated twice more with the same parameters, with a batch normalisation layer between each convolution and ReLU layer. A fully connected layer with 4096 outputs follows the three convolution-ReLU-pooling blocks. A dropout layer with a 20% drop probability is then used to help prevent overfitting. The final layers of the network are a fully connected layer with N outputs, where N is the number of modes the model is being trained on, and a regression layer to calculate the mean-squared-error during training. This network structure and parameters were selected after consultation from Dr P. R. Wiecha of the University of Southampton and an iterative investigation where the number of layers and complexity was gradually increased and the parameters optimised while the prediction error of the trained network was monitored. The investigation confirmed that a network with more convolutional layers produced diminishing reduction in the error yet increased the computation time. It should be stressed however that this network structure is not entirely optimal and many advances in machine learning have been made recently that could further increase the accuracy and decrease the computation time, therefore past this proof of concept further computer science expertise would be valuable.

4.2.1 Training Data

Training a CNN requires a large amount of labelled data, and in some applications it can be difficult to obtain enough data to accurately train a network. In the case of transverse laser modes an arbitrary number of training images may be generated by utilising the equations for the transverse intensity distributions of any modes observed in a system. Free-space laser cavities operating on more than one non-degenerate transverse mode form incoherent superpositions due to the different frequencies of their longitudinal modes [221], therefore for generating training images phase-based components of the electric fields are neglected and the axial position is set to zero. The expressions used to generate the training images were:

$$I_{nm}^{HG} = \left| u_{nm}^{HG}(x,y) \right|^2 = \left| \frac{1}{w} C_{nm}^{HG} H_n \left(\frac{x\sqrt{2}}{w} \right) H_m \left(\frac{y\sqrt{2}}{w} \right) \exp \left[\frac{-(x^2 + y^2)}{w^2} \right] \right|^2 \quad (4.3)$$

$$I_{pl}^{LG} = \left| u_{pl}^{LG}(r,\phi) \right|^2 = \left| \frac{1}{w} C_{pl}^{LG} \left(\frac{r\sqrt{2}}{w} \right)^{|l|} L_p^{|l|} \left(2r^2 \right) \exp \left(il\phi \right) \right|^2 \quad (4.4)$$

where the normalisation constants are

$$C_{nm}^{HG} = \left(\frac{2}{\pi n! m!} \right)^{1/2} 2^{-\left(\frac{n+m}{2} \right)}, \quad C_{pl}^{LG} = \left(\frac{2p!}{\pi (p + |l|)!} \right)^{1/2}. \quad (4.5)$$

Assistance was received from A. D. Coupe in creating images programmatically

from these expressions. Nine modes were selected for training *BeamNet* based on observations of the modal composition of the Ho:YAG laser source, which is detailed in section 4.3.
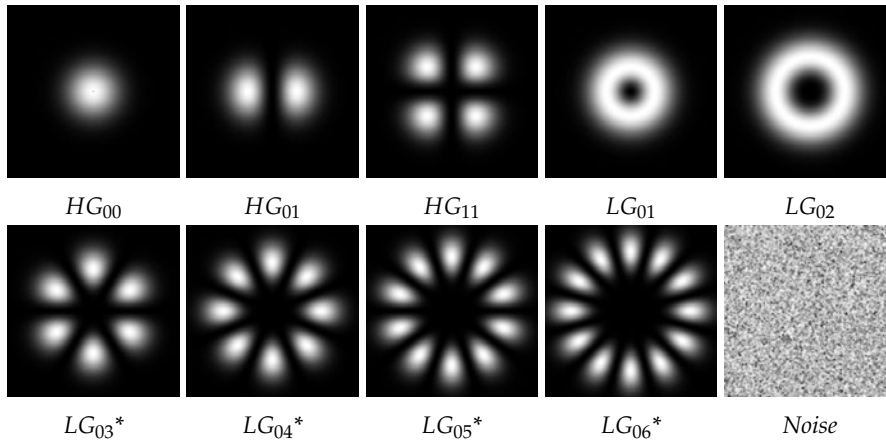
FIGURE 4.4: The transverse modes used to train *BeamNet*. Coherent superpositions of two otherwise degenerate Laguerre-Gaussian modes of the same order with opposite handedness are denoted with an asterisk.

Figure 4.4 shows example images of the selection of modes generated using equations 4.3 and 4.4. The so-called 'petal' modes denoted with an asterisk in figure 4.4 are coherent superpositions of two LG_{0l} modes with opposite handedness [97]. In addition to the nine modes, images of white noise were generated to simulate the lack of a laser beam incident on a camera. To create a varied data set and imitate real laser beams incident on a camera the central positions, beam radius, orientation and maximum combined intensity of the modes in each image was randomised between upper and lower limits. The modal composition present in each image was systematically varied such that each mode was incoherently superimposed with the other modes with normalised intensity contributions varying from 0–100% in 1% increments with equal numbers of images for each mode. 23,816 images were generated for use as a training data set, along with a further 7,384 for use as a validation data set. The images had a resolution of 120×120 pixels and intensity values ranging from $0 - 255$. A label in the form of a 1-D array of normalised modal composition of the form $\{HG_{00}, \cdots, LG_{06}, noise\}$ shared an index with each image in both the training and validation data sets. The training process therefore aimed to teach *BeamNet* to return a similar array with the composition of each mode indexed within. The image and label arrays were concatenated into four 4-D datastores to avoid exceeding the computer memory capacity. The final data was therefore separated into indexed datastores for training images, validation images, training labels, and validation labels.
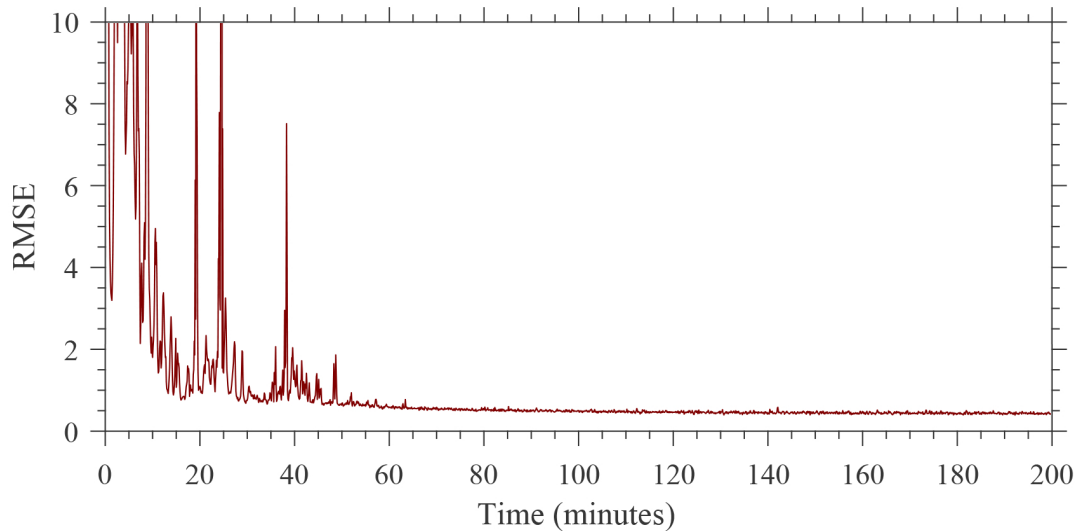
FIGURE 4.5: RMSE error as a function of time spent training *BeamNet*.

4.2.2 Training Process

In the training process for *BeamNet* an image from the training images data set is passed through the network in the forward direction. The output of the network is compared against the label from the training labels data set to find an error function. Backwards propagation though the network is then used to calculate the gradient of the error with respect to the learnable weights. This is repeated for a mini-batch of images; in the case of *BeamNet* the mini-batch size was 256. After iteration over the mini-batch an optimisation algorithm (Adam [222]) uses the computed error gradients and a specified learning rate to update the network weights, with a high learning rate corresponding to large adjustments. After the training process has iterated over all of the training data, an epoch is said to have ended. The training process is repeated over a specified number of epochs, with the learning rate potentially changing, until the desired accuracy of the network has been achieved or no further benefit is obtained. Figure 4.5 displays the Root-Mean-Square-Error (RMSE) of *BeamNet* as a function of time spent in the training process. *BeamNet* trains for 2000 epochs, with the learning rate decreasing by a factor of 10 every 500 epochs. Training for a larger number of epochs gives diminishing returns in error reduction. Initially, the RMSE is extremely large and variable in the completely untrained network, although it decreases rapidly due to the high learning rate. However, this high learning rate has the undesirable consequence of causing the network weights to occasionally well overshoot the optimum values, leading to the spikes observed before approximately 60 minutes of learning time. At this time, the 500th epoch has begun and the learning rate has decreased. The total training time in this example is just over 200 minutes on a computer equipped with an *Nvidia RTX 2080 Super* graphics processing unit (GPU). A GPU is used as the primary hardware for training and computing using CNNs due to the large number of parallel processors. Training with a conventional desktop CPU is possible, although the time would be on the order of weeks.

4.2.3   Evaluation

As a first test of the performance of *BeamNet*, the validation data set was passed to the network. Using a *Nvidia RTX 2080 Super* GPU *BeamNet* returned a prediction for the modal composition of 7384 beam images in 340 *ms* when averaged over 100 runs, corresponding to an average time of 49 *µs* per image. When paired with a camera with a sufficient frame rate this would allow for modal composition predictions on time-scales akin to the upper-state laser level lifetimes of some active ions. The accuracy of the network was explored by measuring the RMSE of the predictions from the validation data set. This is defined as

$$RMSE = \sqrt{\frac{\sum_{n=1}^{N}(\hat{x}_n - x_n)^2}{N}} \tag{4.6}$$

where $\hat{x}_n$ is the true value for mode *n*, x_n is the predicted value and N is the total number of modes the network is trained on. The normalised RMSE of *BeamNet's* predictions on the validation data set was 5.2% in a centesimal representation. This error is of a similar magnitude to previous numerical demonstrations of modal decomposition [206], but higher than competing investigations involving CNNs. Liu *et al.* [217] reported prediction errors of $< 2\%$ while An *et al.* [218] reported errors on the order of 1%, although it is important to note that their networks were trained on three and five spatial modes respectively compared to the ten outputs in *Beam-Net*. When *BeamNet* is trained on the first three LG_{0l} modes the normalised RMSE on the validation data set falls to 1.4%. For a first experimental demonstration an early version of *BeamNet* was used to analyse the modal composition of a Yb:YAG laser that operated on combinations of HG_{00}, HG_{01} and radially polarised LG_{01} modes [219]. This laser is detailed in section 3.1. The beam was sampled onto a *Thorlabs DCC1545M* CMOS camera as shown in figure 4.6. The frames from the CMOS camera were cropped and subsampled before being analysed by a version of *BeamNet*
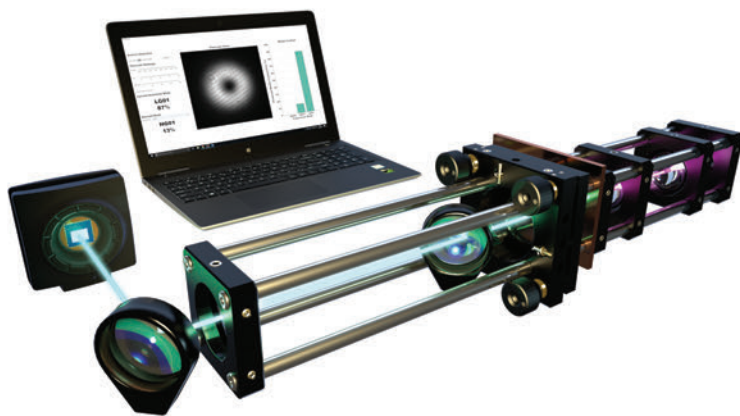
FIGURE 4.6: Render of the prediction of the modal composition of a
Yb:YAG laser using a CNN.
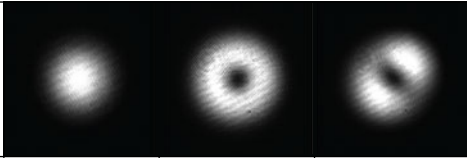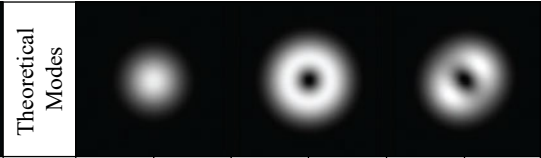
Experimental Modes	CNN	CNN	CNN	Theoretical Modes	Actual	CNN	Actual	CNN	Actual	CNN
HG_{00}	100%	0%	0%	HG_{00}	100%	100%	0%	0%	0%	0%
HG_{01}	0%	13%	75%	HG_{01}	0%	1%	0%	1%	75%	70%
LG_{01}	1%	87%	26%	LG_{01}	0%	0%	100%	98%	25%	26%

FIGURE 4.7: Right: theoretically generated modes with CNN predicted modal composition compared against actual composition. Left: experimentally obtained modes from a laser aligned by using CNN modal composition predictions to match the theoretical modal composition.

trained on the three visually observed output modes. Figure 4.7 displays the results of this preliminary experiment. A selection of theoretically generated modes including two pure and one incoherent combination is shown in the right-hand side of figure 4.7. The modal compositions used to generate the images are given in the 'Actual' column, and the predictions of *BeamNet* are shown in the 'CNN' column. There is some minor discrepancy between the actual and CNN predictions that is likely caused by the low contrast between images with similar compositions of these modes. This discrepancy is represented by the 8% normalised RMSE error of this early version of *BeamNet*. In addition, the predicted modal contents do not always sum to 100%; this is due to each mode having a composition predicted independently on top of the error introduced by the network. The Yb:YAG laser was then manually aligned to attempt to match the modal compositions of the three theoretically generated modes in figure 4.7. The modes from the Yb:YAG laser that achieved the closest compositions to the theoretical cases are shown in the left-hand side of figure 4.7. This experiment demonstrated that despite artefacts such as noise and interference fringes present in real camera images of laser modes a CNN was able to facilitate the real-time alignment of a laser source to produce visually similar modes to the desired result. Further experiments would need to be performed with other means of accurately measuring the modal composition in order to establish the accuracy of *BeamNet* on real laser modes past this simple visual comparison.

4.3 Automatic Optimisation of a Radially Polarised Ho:YAG Source

After the initial indication that *BeamNet* could successfully predict the modal composition of a simple higher-order-mode laser an experiment was performed to determine whether these predictions could be used as part of a control loop. A laser design by P. C. Shardlow *et al.* [223] was identified as previously suffering from problems with the output modal composition changing with pump power. A source
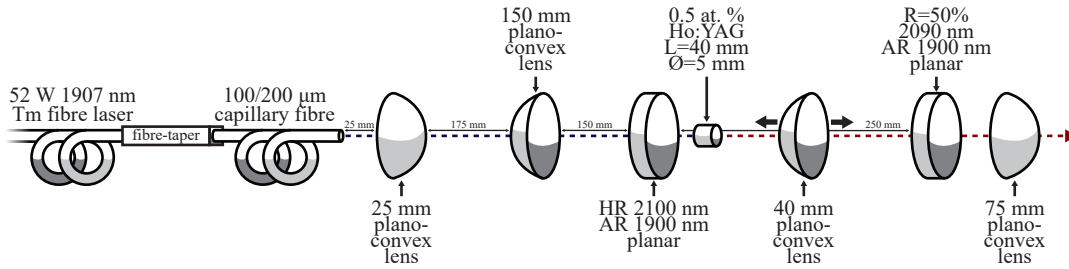
FIGURE 4.8: Schematic of the radially polarised Ho:YAG laser

inspired by this design was constructed by M. J. Barber and P. C. Shardlow; the schematic for this laser is shown in figure 4.8. A 40 *mm* long, 5 *mm* diameter 0.5 *at.%-* doped cylindrical Ho:YAG crystal, which was anti-reflection coated on both facets for 1.9 *μm* and 2.1 *μm*, was used as the gain medium. The Ho:YAG crystal was mounted in a water-cooled copper heatsink where the coolant temperature was maintained at 15°*C*. A highly reflective ($R = 99.9\%$ at 2.1 *μm*) planar mirror and a planar output coupler ($R = 50\%$ at 2.1 *μm*) formed the laser cavity around the Ho:YAG crystal, with a total cavity length of 250 *mm*. The Ho:YAG crystal was positioned close to the highly reflective mirror. The laser is pumped using a single-mode 1907 *nm* Tm fibre laser with a maximum available pump power of 52 *W*. In order to promote operation on the first-order radially polarised mode the pump laser is spliced, via a tapered section, to a capillary fibre taper with a 100 *μm* diameter inner air-hole and 200 *μm* outer diameter. When relay-imaged through a 25 *mm* and a 150 *mm* plano-convex lens the pump spot forms an annular ring in the Ho:YAG crystal with a 1.2 *mm* outer diameter. A 40 *mm* focal length anti-reflection coated plano-convex lens was included in the cavity in a variable position. The purpose of this intra-cavity lens was to change the cavity mode size in the laser crystal as a function of its axial position. By exploiting thermally induced bifocussing between the azimuthal and radial polarisations in the laser crystal, one can tailor the cavity mode size such that the laser operates on only the radially polarised LG_{01} mode, as described in section 3.1.2.

4.3.1   Source Characterisation

As predicted the intra-cavity lens required precise manual adjustment to obtain a radially polarised LG_{01} mode of reasonable quality. The output mode significantly changed with the incident pump power due to thermal lensing in the Ho:YAG crystal, requiring manual readjustment of the intra-cavity lens for each change. To characterise the source the incident pump power was set to 28 *W*. The intensity profiles, captured using a FLIR Lepton®microbolometer camera, of the radially polarised mode are shown in figure 4.9. Figure 4.9a is the output mode without any polarising optics. It is a visually acceptable LG_{01} profile, although there is some astigmatism and symmetry breaking features present; these are believed to be due to slight misalignment and possible asymmetrical thermal gradients. A thin-film linear polariser

was used to observe polarisation state of the output, as shown in figure 4.9b-e. These images, which represent different orientations of the linear polariser show the two-lobe HG_{01} form expected of a radially polarised mode after transmission through a linear polariser, with good minima between the lobes indicating a high polarisation purity.
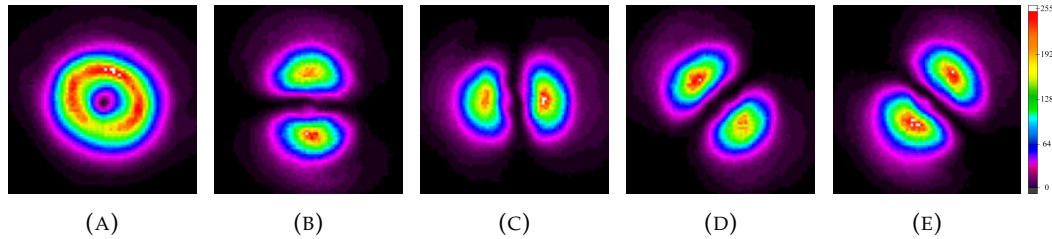
FIGURE 4.9: Intensity profiles of the output of the radially polarised Ho:YAG at 28 *W* incident pump power. (A) is without a linear polariser while (B)-(E) are after transmission through a linear polariser.

The radial polarisation extinction ratio (RPER) was measured from the images in figure 4.9 using the method detailed in 3.1.4. The lowest RPER obtained from the images was 25 : 1, indicating the laser operated on a high quality radially polarised mode when manually aligned at this pump power.

The M^2 of the radially polarised Ho:YAG source was measured in this manually aligned configuration to provide a comparison to similar sources in the literature. Figure 4.10 shows the measurements of the beam diameter on two axes as a function of axial position through a focus from which the M^2 is calculated. The measured M^2 was 2.0 in the sagittal axis and 2.1 in the tangential, which agrees with the expected value for a theoretical LG_{01} mode. The output of the Ho:YAG source was measured

(A) Sagittal axis

(B) Tangential axis
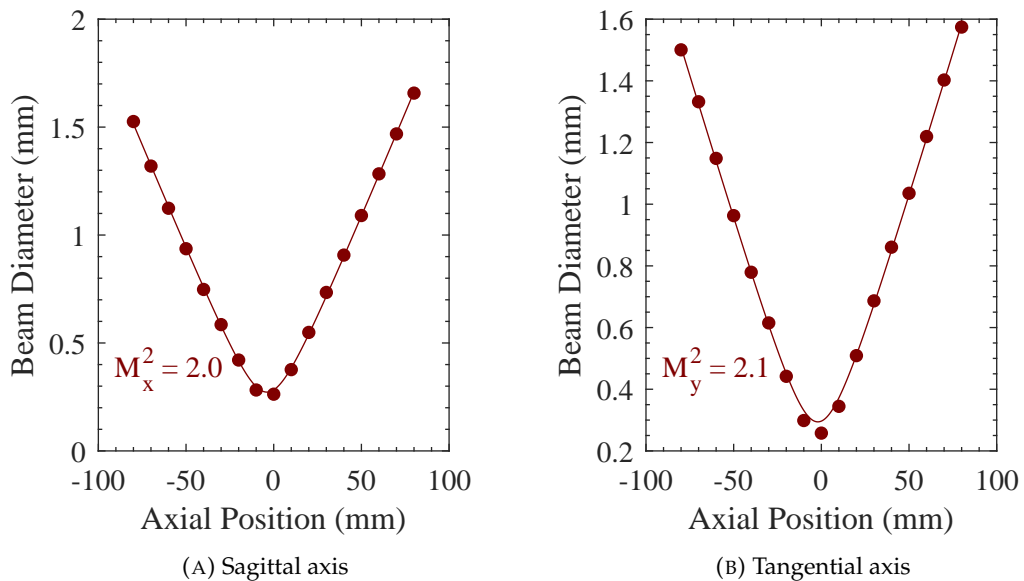
FIGURE 4.10: Beam quality factor measurements in sagittal (x) and tangential (y) axes for the manually optimised radially polarised Ho:YAG source at an output power of 28 *W*.

using a Yokogawa AQ6375B optical spectrum analyser, as shown in 4.11. As expected there is a single peak at approximately 2090 nm with a FWHM linewidth of $0.4\,nm$, typical of a rod laser without wavelength controlling elements. In summary,
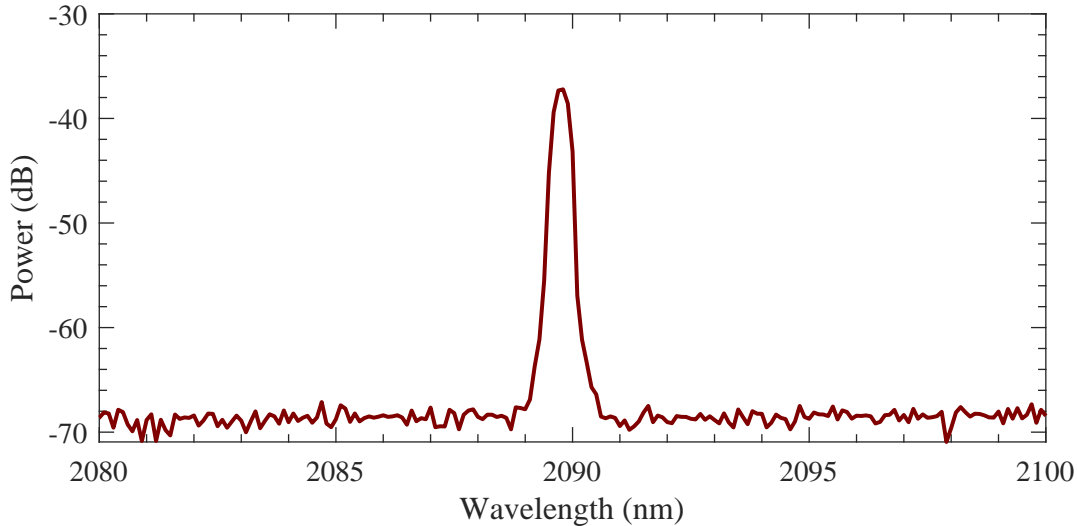
FIGURE 4.11: Emission spectrum of the radially polarised Ho:YAG source at 28 *W* output power.

the Ho:YAG source produced a high quality first-order radially polarised mode after careful manual alignment. Changes in pump power and slight axial displacement of the intra-cavity lens significantly impacted the appearance and polarisation purity of the output mode as desired, allowing for a demonstration of CNN-based mode control.

4.3.2   Control System

A control system was implemented in order to attempt to achieve the stabilisation of the radially polarised Ho:YAG source using a CNN. This control system is represented in figure 4.12. The output from the Ho:YAG laser is split into two equal power beams with the aid of a dichroic mirror with a polarisation independent reflectivity of 50%. After suitable attenuation, one beam is transmitted though a thin-film linear polariser before being captured by a FLIR Lepton camera. The polariser analysed beam is required to allow for *BeamNet* to diagnose a radial polarisation state as a transmitted HG_{01} mode. The other beam, with an unaltered polarisation state, is captured by a second camera. The images are cropped from their original 160×120 pixel resolution to 120×120. The cropped images of both beams then have their transverse modal composition predicted independently of each other by the *Beam-Net* CNN. The predicted modal content of each beam is returned as the normalised vector $\vec{P}$. The desired modal composition of the output beam is denoted $\vec{D}$.

$$\vec{P} = \left[P_{HG_{00}}, P_{HG_{01}}, P_{LG_{01}}, \cdots, P_{HG_{nm}}, P_{LG_{pl}} \right] \qquad (4.7)$$
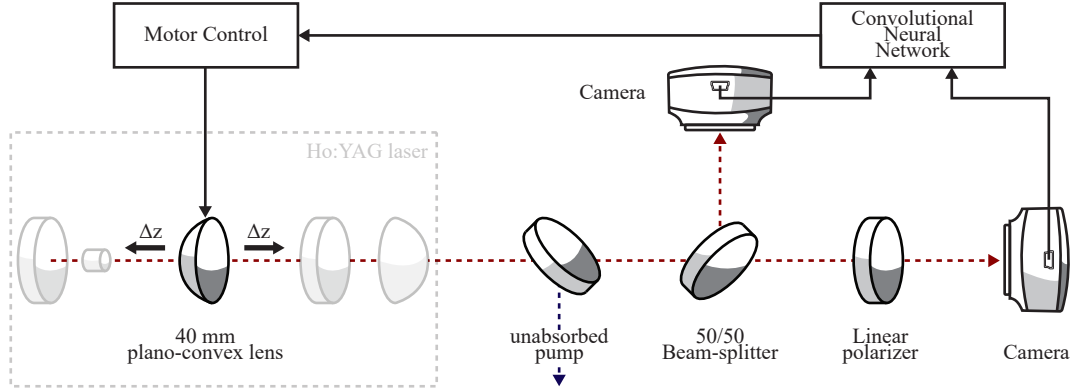
FIGURE 4.12: Schematic of the CNN based control system used to stabilise the radially polarised mode in a Ho:YAG laser

$$\vec{D} = \left[D_{HG_{00}}, D_{HG_{01}}, D_{LG_{01}}, \cdots , D_{HG_{nm}}, D_{LG_{pl}} \right] \tag{4.8}$$

An error function, E, is created between the predicted and desired modal composition vectors, such that

$$E = \frac{\|\vec{P} - \vec{D}\|}{\sqrt{N}} \tag{4.9}$$

where N is the number of modes. If the predicted modal composition is close to the desired modal composition, the error function tends to 0, while for completely different vectors the error tends to 1. To obtain a first order radially polarised mode the desired modal composition is 1 for the LG_{01} mode and 0 for all others in the beam path without the linear polariser. Similarly for the linear polariser analysed beam the desired modal composition is 1 for HG_{01} and 0 for all other elements. Therefore the total error function, E_{total} is a combination of the individual error functions for the polariser analysed beam, E_p, and the unaltered beam E_u.

$$E_{total} = E_p \cdot E_u \tag{4.10}$$

A stepper motor is used to dither the lens from its current position to five neighbouring positions so that the error function may be computed at each. The range of movement during the dithering of the lens was small compared to the displacement necessary to significantly change the modal content of the laser output. The gradient of the error function computed during the dithering operation is passed to a gradient descent algorithm to proportionally update the central position of the 40 *mm* plano-convex lens in the Ho:YAG laser cavity. This process is repeated while the laser is operating to optimise the modal composition despite parameter changes.

4.3.3 Transverse Mode Stabilisation

To test the effectiveness of the CNN based control system the pump power of the Ho:YAG source was varied with and without the control active. Figure 4.13 is a table

FIGURE 4.13: Output power of the Ho:YAG source as a function of pump power for the cases of no locking and CNN based LG_{01} and HG_{01} feedback locking.

of images at various pump powers of the output mode after a linear polariser with: no stabilisation, stabilisation to the LG_{01} radially polarised mode and to demonstrate the flexibility of the method, stabilisation to the fundamental HG_{01} mode. Without the control system active the output mode is an LG_{01} mode with good radial polarisation at 28 W of incident pump power; this is because the mode was manually optimised at this power. Below this pump power, and without the control system, the mode is not recognisable as an LG_{01} anymore. Similarly as the pump power is increased the radial polarisation purity decreases as other modes are introduced. For reference, without the control system the M^2 parameter was measured to be 2.0×2.1 at 28 W and 2.1×2.0 at 49 W incident pump power.

When the CNN based control system is active and set to optimise the radially polarised LG_{01} mode the radial polarisation purity is quite consistent at all power levels. At the highest incident pump powers there is some slight polarisation state degradation that the control system was not able to account for in its current proof-of-concept form. The M^2 parameter of the LG_{01} mode is effectively unchanged with the control system active, at 2.0×2.1 at 28 W and 2.0×2.0 at 49 W. The linearly polarised HG_{00} mode obtained using the CNN control system was consistent at all power levels, with only a slight astigmatism and the presence of either scattering or a faint high order mode reducing the modal purity. The M^2 of the obtained HG_{00} mode was measured to be 1.3×1.4; this inflated beam quality parameter can be simply explained by the pump and cavity being designed for operation on the LG_{01} mode, so there was likely some higher-order mode content.

To quantify the performance of the control system in optimising the Ho:YAG to a radially polarised mode the RPER was measured as a function of the incident pump
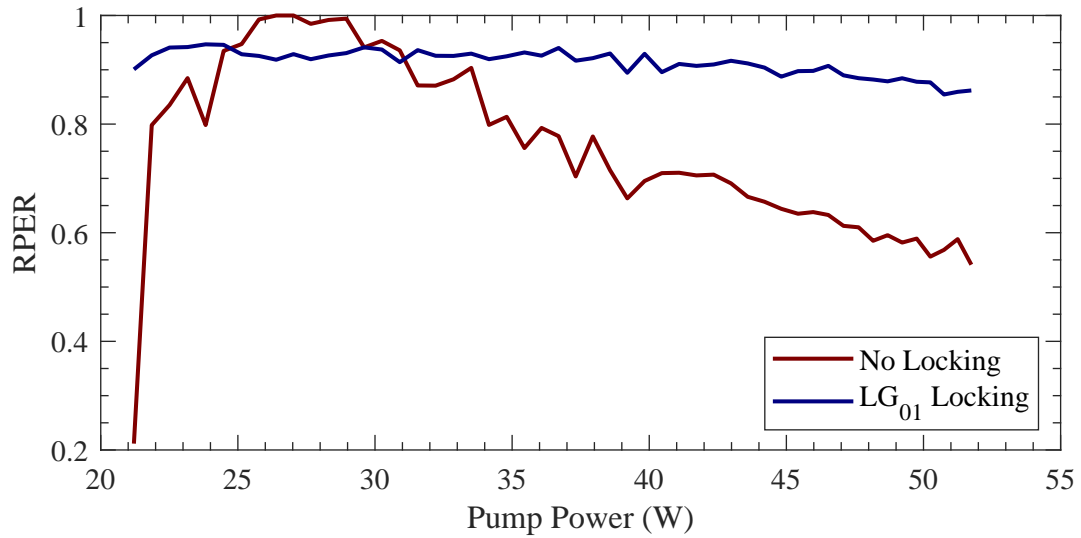
FIGURE 4.14: Radial Polarisation Extinction Ratio of the Ho:YAG source as a function of pump power with and without CNN feedback

power with the control system active and inactive. The data is shown in figure 4.14. As shown in the images in figure 4.13, when the control system is not active the RPER is only high at an incident pump power between 25 and 30 W, close to the power for which the laser was manually aligned. Away from the manual alignment the RPER significantly decreases down to as low as 0.21, representing a transition to either the HG_{00} at lower powers and azimuthal LG_{01} and higher order components at powers above 28 W. In comparison, when the control system is active and attempting to lock the output mode to a radially polarised LG_{01} the RPER is almost constant over the full range of pump power. As noted from the beam images, at the highest pump powers there is a slight degradation in the RPER although it remains above 0.86 - a large improvement with the control system active. In addition, it is observed that the peak RPER of the source without the control system active is higher than with the control system around the incident pump powers that the source was manually aligned on. This is attributed to the continuous dithering of the intracavity lens.

To measure the potential impact of the control system on lasing performance the output power of the Ho:YAG source was measured as a function of absorbed pump power for the cases where the control system was inactive, locking to the radially polarised LG_{01}, and locking to the HG_{00} mode. This data is shown in figure 4.15. Without the control system locking the transverse mode the slope efficiency of the Ho:YAG source was measured at 67%. With the control system active the efficiency of the source is reduced to 61% for the radially polarised LG_{01} mode and 0.55% for the HG_{00} mode. The higher efficiency of the source with no control system active is attributed to partial operation on higher-order modes having an improved overlap with the pumped region at high pump powers in this source. The control system effectively constrains operation of the source to the radially polarised LG_{01} mode,
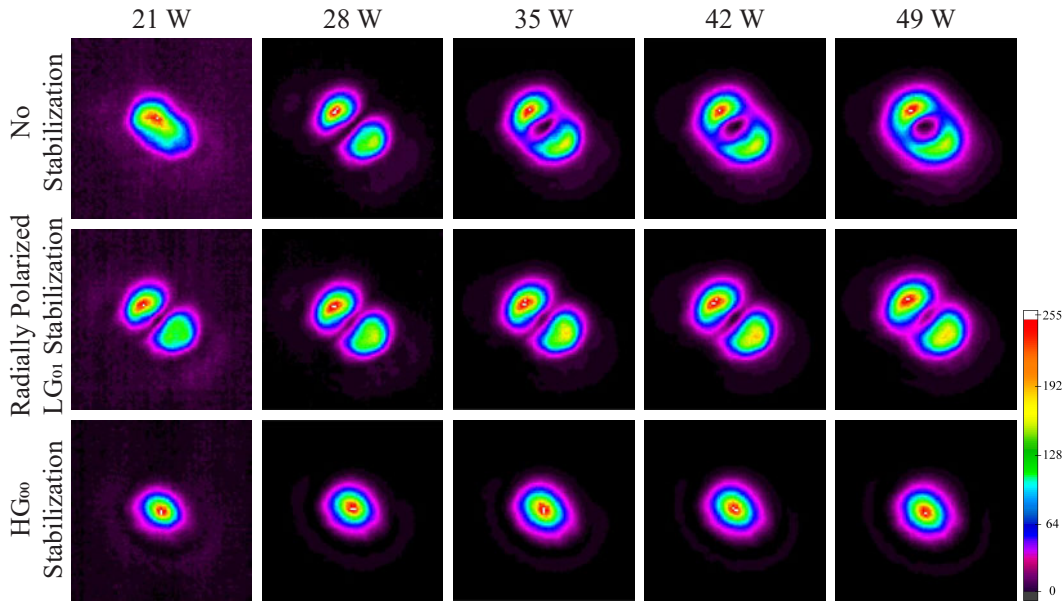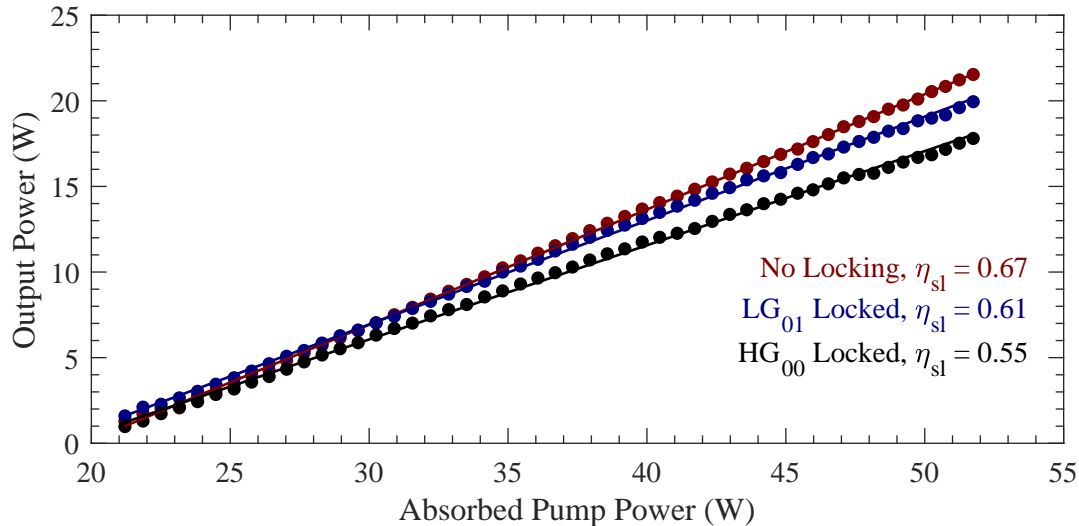
FIGURE 4.15: Output power of the Ho:YAG source as a function of pump power for the cases of no locking and CNN based LG_{01} and HG_{01} feedback locking.

which extracts slightly less gain from the laser crystal compared to a more multi-mode output. The large difference between the efficiency of operation on the HG_{00} and LG_{01} modes is again attributed to the laser simply not being designed to operate on the fundamental mode. However, the robust operation on the HG_{00} mode demonstrates the flexibility of the CNN based approach, with only a single vector needing to be changed to select a different transverse mode.

4.4   Summary

In summary, a CNN has been used to demonstrate the effective recognition and prediction of Laguerre and Hermite-Gaussian transverse laser modes in real-time. The computation times are of particular note at an average of 49 μs per image and would enable a fast control system to utilise measurement frequencies in the thousands of Hz provided that a high frame-rate camera is used. The accuracies of the network were acceptable, with a 5.2% normalised RMSE error on a validation dataset with ten degrees of freedom. This error was suitable for a proof-of-concept demonstration of the application and experimental proof, however it is very likely that this error could be reduced by a large amount while keeping the computation times low. The *BeamNet* network that was created was the result of a first foray into the topic, using introductory tutorials and advice. With more research and expertise the network could use more advanced and novel techniques to give improved results. Despite this, *BeamNet* proved to be useful in providing a real-time metric for the optimisation of solid-state laser cavities. The first demonstration of its use in an experimental test was in diagnosing the modal composition of a Yb:YAG source. The laser was adjusted to produce diagnosed modal compositions as close as possible to a selection of theoretical modes. The results showed that the experimental modes were at least

visually similar to the theoretical modes with the target composition. Therefore, in a limited form, a CNN was demonstrated as a real-time laser optimisation aid that may be able to overcome the limitations of the use of the beam quality parameter for higher-order modes.

A more robust test of the *BeamNet* CNN was whether it could be used to provide an error signal for a feedback-based control system to lock a laser to a particular transverse mode. This was achieved in the radially polarised Ho:YAG source demonstration where the CNN was used to create an error signal to control the position of an intra-cavity lens. The error signal was used by a gradient descent algorithm which continually dithered the lens position around a central point before updating the central position to the new optimum. This system was able to keep the output mode a radially polarised LG_{01} over the full range of pump power, in contrast to not having the control system active. In addition, the flexibility of the CNN based system was demonstrated by locking the Ho:YAG system to a HG_{00} mode of adequate quality. Some limitations of this proof-of-concept CNN control system were identified; the peak of the radial polarisation extinction ratio was higher when the system was manually aligned compared to the CNN optimised value at this same pump power. This was believed to be due to the continuous dithering of the gradient descent algorithm. Several control algorithms, such as hill-climb and PID control, were attempted in the experiment with limited success before the gradient descent was used. It is probable that a more suitable algorithm, for which dithering is not necessary, could produce improved results. Furthermore, the control relied on the optimisation of a single parameter in the laser cavity - the intra-cavity lens position. A more advanced laser control system could simultaneously control multiple variables in the laser cavity, such as the mirror alignment, in addition to the intra-cavity lens, while using the CNN to produce an error signal.

Another problem that was identified from the use of the *BeamNet* CNN in the Ho:YAG system was the uncertainty of the network in the face of experimental and camera artifacts. The network returned lower peak predictions than expected due to the contributions of noise and mode distortions such as astigmatism. To make the CNN more robust, it is possible to generate experimental image imperfections in the training data so that the network learns modal characteristics while ignoring the imperfections. A. D. Coupe developed parts of the training data script to implement some possible image imperfections, although ultimately these were not implemented for the sake of simplicity in this proof-of-concept. Future iterations of CNN based control systems should implement the imperfections in the training data. Ultimately, the limitations of a CNN based modal composition metric and control system are a symptom of its infancy.

Overall these results allow for the conclusion that a CNN trained to predict transverse modal compositions is effective in live optimisation of a free-space cavity to a first-order radially polarised mode, with strong indications that it can be used to optimise for a general modal composition. The key advantages demonstrated are

the orders-of-magnitude reduction in computation time compared to similar methods and the simplicity of its implementation in laser systems. It is anticipated that CNNs will find a place in future industrial lasers to aid in maintaining the output beam profile and in diagnostics for higher-order modes where the M^2 parameter is not sufficient.

Chapter 5

Intracavity S-Waveplate for Generation of Radial Polarisation

This chapter reports the design, construction and results of a laser source which used an intracavity spatially variant waveplate (S-waveplate) to ensure operation on the first-order radially polarised mode. This was made possible for the first time by the recent development of refined femtosecond laser written S-waveplate with that promised much lower scattering losses than previous iterations [224].

The aims of the experiment were to investigate what happens to the cavity mode either side of the S-waveplate, with the primary hope being the generation of a high quality radially polarised mode. In addition, the placement of the S-waveplate within a laser resonator allows for the use of well-developed loss measurement techniques, as the absolute loss of this new S-waveplate had yet to be measured at the design wavelength of 1064 *nm*.

5.1 Spatially Variant Waveplates

The control of the phase of light has been traditionally performed by altering the thickness or the refractive index of a medium. It is also possible to alter the geometric phase of light by the use of spatially variant anisotropy, which is the concept behind the spatially variant waveplate (S-waveplate). With the aid of a femtosecond-pulsed source, anisotropy can be introduced in optical media which can take on any arbitrary design. This process is described and explained by Sakakura *et al.* in [224]. The S-waveplate of interest here is a substrate in which sub-wavelength birefringent structures have been written, where the slow axis of these birefringent structures are aligned at an angle $\phi/2$ to the azimuthal angle ϕ. This is the origin of the term 'spatially variant', as these waveplates have a continuously varying birefringence as a function of azimuthal angle. In simple terms, a spatially variant birefringence can be permanently written into a substrate in such a way that linearly polarised light (when aligned correctly) is converted to radially polarised light after transmission through the S-waveplate. If the retardance is correctly written into the waveplate, and if the incident polarisation is pure, the opposite is also true; radially polarised light transmitted through the S-waveplate is converted to linearly polarised light.

This type of S-waveplate has been used in the past to operate a cladding-pumped Yb-doped fibre laser on the radially polarised mode with the aid of the waveplate in an external feedback cavity [159]. In this paper, the authors note that the far-field transmission of the S-waveplate used was only $\approx$ 75%. This loss was attributed to scattering and absorption from inhomogeneities and the femtosecond laser induced defects, along with the lack of anti-reflection coatings on the fused-silica substrate. This level of loss was acceptable for a cladding-pumped fibre laser due to the extremely high gain available, but in a free-space source with a laser crystal this loss would be disastrous for the threshold and power characteristics. In 2020, an S-waveplate with the same polarisation converting properties was published which claimed much lower optical loss [224]. A femtosecond laser was used to introduce sub-wavelength birefringent structures in the same way, however by carefully choosing the parameters of the writing laser the authors claimed that the nanoporous silica structures they observed in this new generation of S-waveplate were fundamentally different from the laser-induced nanogratings in the previous generation of waveplates. Y. Lei *et al.* provided one of these waveplates for testing within a solid-state laser cavity. Figure 5.1 is a photograph of the femtosecond
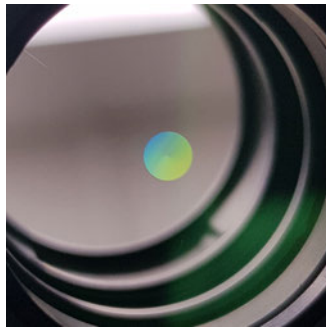
FIGURE 5.1: The femtosecond written S-Waveplate in the visible spectrum.

S-waveplate designed to act as a linear-to-radial polarisation converter. It is important to note that in this photograph the S-waveplate is at a very different angle of incidence to what it is designed for, which allows the effect of the birefringence to be seen as a colour gradient for white light. This S-waveplate was written into an excimer grade UV fused silica substrate with a diameter of 25 *mm* and a thickness of 3 *mm*. The substrate was coated with an anti-reflection coating specified as $R < 0.2\%$ at 1064 *nm*. In order to ensure that the performance of the S-waveplate was not significantly impacted by the substrate, high optical specifications were chosen. The substrate had a specified low wavefront error of $\lambda/20$, a parallelism of 5″ and a scratch-dig surface quality of 10-5. The altered region of the substrate had a diameter of 6 *mm* and was written directly under the AR coating on one side of the substrate.

5.2 Experimental Configuration

In order to examine the effect of introducing an S-waveplate into a laser resonator, a linearly polarised Nd:YVO$_4$ source operating on the LG_{01} mode at 1064 *nm* was constructed. A schematic of this source is shown in figure 5.2.
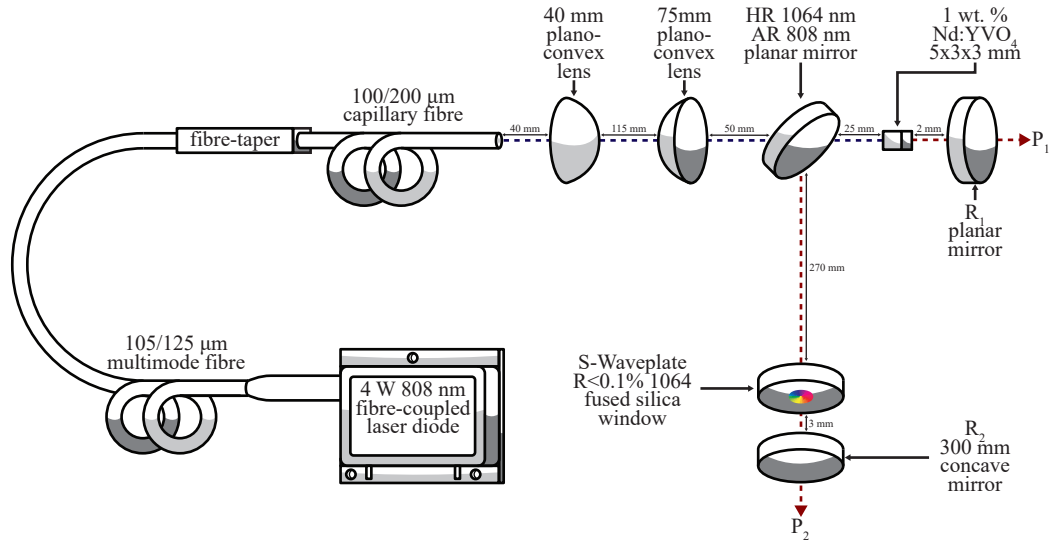
FIGURE 5.2: Schematic of the end-pumped 1064 nm radially polarised intracavity S-waveplate Nd:YVO$_4$ laser.

The laser cavity was made from three mirrors, folded into an 'L' shape. This was chosen in order to be able to introduce pump light to the cavity while also being able to see the output beam in two opposite directions. The transverse mode in the cavity would be different either side of the S-waveplate when it was introduced, so having access to both of these modes was deemed important. Two of the cavity mirrors were planar, while the third was concave with a 300 *mm* radius of curvature. The total cavity length was 300 *mm*. One of the planar mirrors was used at one end of the laser cavity as an output coupler, with a reflectivity denoted R_1. At the other end of the cavity the concave mirror was used as another output coupler, with reflectivity denoted R_2. The final planar cavity mirror was used as a pump input coupler and was therefore highly transmissive ($T > 98\%$) at the 808 *nm* pump wavelength and highly reflective ($R > 99.5\%$) at the intended 1064 *nm* lasing wavelength. This mirror was orientated at 45° to the other cavity mirrors. The gain medium in this source was a cuboid 1 *wt*.% Nd:YVO$_4$ crystal with dimensions $5 \times 3 \times 3$ *mm* that was mounted in a water-cooled copper heat-sink. The end facets of the crystal were anti-reflection coated at the pump and lasing wavelengths. The separation between the crystal and the planar output-coupler was approximately 2 *mm*. The crystal was pumped using a 4 *W*, 808 *nm* fibre-coupled laser diode (BWT Beijing LTD.) which was spliced to a capillary fibre taper identical to the one discussed in section 3.1.1. The 100/200 *μm* capillary fibre conditioned the pump light into an annular profile in the near-field in order to target the first-order LG_{01} mode. The capillary fibre was imaged into the Nd:YVO$_4$ crystal with a 40 *mm* and a 75 *mm* plano-convex lens used as

part of a 4f telescope. The magnification factor for the pump telescope was therefore 1.875, meaning that the pump spot in the laser crystal had a 375 μm outer diameter and a 188 μm inner diameter. The S-waveplate was introduced and removed from the cavity as required in order to investigate its impact. When in the cavity it was positioned approximately 3 mm from the concave output coupler at a normal orientation to the beam. Finally, the outputs are shown on figure 5.2 as P_1 and P_2 from output coupler R_1 and R_2 respectively.

5.3   Characterisation

5.3.1   Beam Images
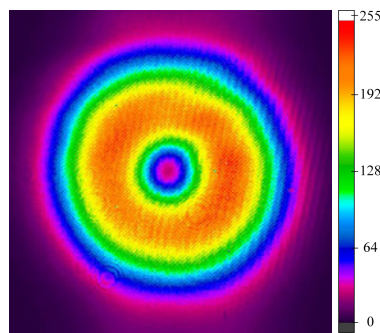
FIGURE 5.3:   Linearly polarised output intensity profile of the Nd:YVO$_4$ source without an S-waveplate in the cavity.

The pump power was set to the full available 4 W for the purpose of imaging the outputs of the source. In the absence of the S-waveplate in the cavity the transverse intensity profile of the output is shown in figure 5.3. Visually the output is an excellent LG_{01} mode. It is symmetrical, has a lack of modal impurities, and with the exception of a slightly higher than desired central intensity resembles a theoretical LG_{01} mode. The mode was linearly polarised and identical from both outputs of the laser. This provided an excellent starting point for observing the effects that the S-waveplate might have on the mode. Figure 5.4a is a CCD camera image of the output P_1 of the source when the S-waveplate was present in the cavity. Unfortunately there is obvious distortion present within the mode, but the overall profile retains an annular shape and is comparable to other published LG_{01} modes. The central region has also expanded relative to the rest of the mode. This was one of the major flaws in the S-waveplate during its construction. It was found that the central region of the S-waveplate that should provide a polarisation singularity had poorly defined anisotropy at its centre that caused some distortion in the laser mode. The effect of this was that the cavity mode had to be expanded in order to fit the centre of the S-waveplate within the natural singularity of the LG_{01} mode, leading to the cavity design in figure 5.2.

The mode from output P_1 was linearly polarised, as evidenced by the images presented in figures 5.4b and 5.4c which correspond to the transmission of the mode

(A) No polariser
(B) After linear polariser, maximised transmission
(C) After linear polariser, minimised transmission
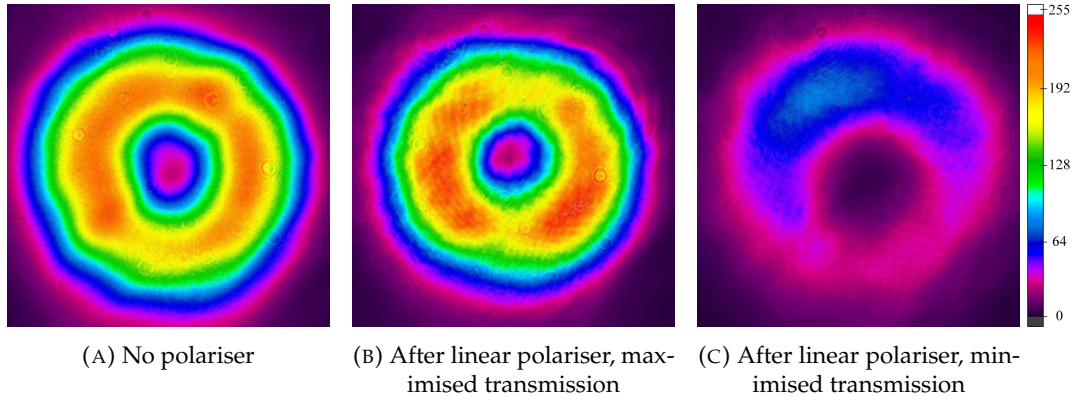
FIGURE 5.4: Intensity profiles of the linearly polarised P_1 output of the Nd:YVO$_4$ source with the S-waveplate in the cavity.

through a linear polariser with maximised transmission and the same with the polariser rotated by 90°. The majority of the mode is transmitted through the linear polariser when the transmission is maximised, with the exception of a region on one side of the mode. This intensity not transmitted in 5.4b can be found in 5.4c. This is a sign that the retardance of the S-waveplate is sub-optimal in this region. The

(A) No polariser
(B) After linear polariser, 0 degree orientation
(C) After linear polariser, 90 degree orientation
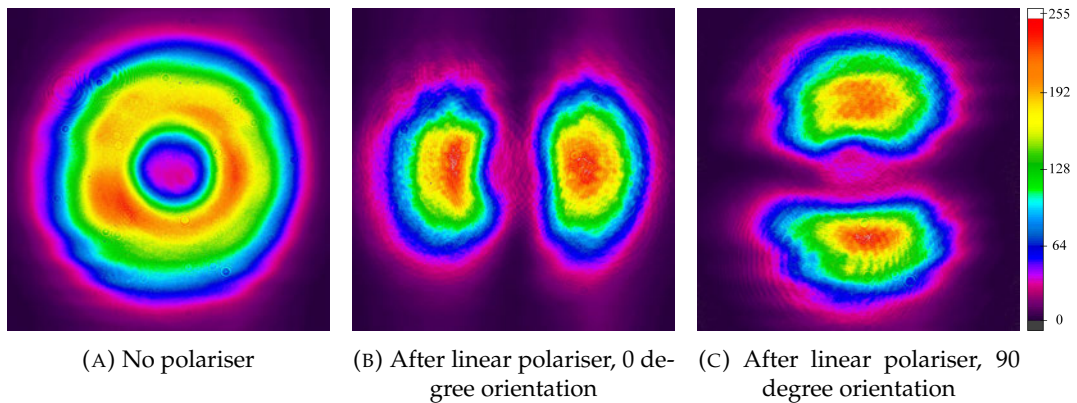
FIGURE 5.5: Intensity profiles of the radially polarised P_2 output of the Nd:YVO$_4$ source with the S-waveplate in the cavity.

intensity profile of the other output, P_2, is shown in figure 5.5a. Again some distortion is present in the output mode. However, it is still recognisably annular, albeit with an enlarged central intensity minimum compared to the rest of the mode. Figures 5.5b and 5.5c show the same output albeit after transmission through a linear polariser with a 90° shift in orientation between the images. These look very much like the HG_{01} profile that is expected for the transmission of radially polarised light through a linear polariser. The polarisation purity looks good, as the images show two distinct lobes at each orientation with intensity low between the lobes.

These results show clear potential for the direct generation of radial polarisation in a laser cavity, which may be scalable to higher power. There is an interesting question as to what the mode in 5.4a *is*. While in a radially polarised mode the central singularity is formed as a result of a polarisation singularity, the presence of the

same in the linearly polarised output may indicate a phase singularity, meaning that this output is a spiral phase LG_{01} mode that may carry OAM. Another explanation is that this mode is an incoherent combination of a HG_{01} and a HG_{10} mode, or two handednesses of LG_{01} modes. Unfortunately this would require extensive experimentation to confirm which explanation is true that was not possible within time constraints.

5.3.2 Polarisation Extinction Ratios

The polarisation characteristics of the source were quantified using the measurement of their extinction ratios for the linearly and radially polarised beams respectively. For the linearly polarised case, the power transmitted through a linear polariser as a function of polariser orientation angle is measured, and the ratio between the maximum and the minimum transmitted power gives the linear polarisation extinction ratio. Figure 5.6 is a graph of these measurements taken for output P_1 without the
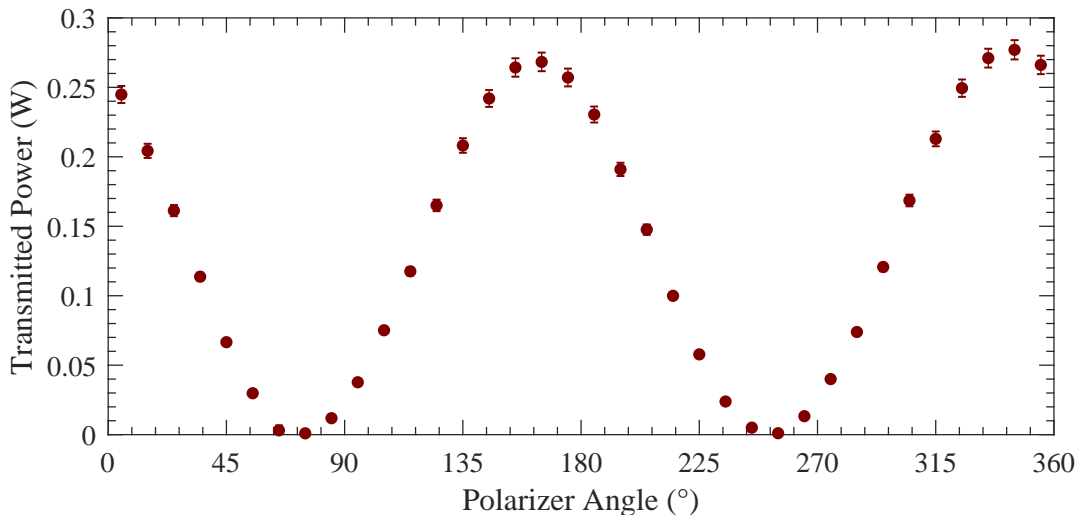
FIGURE 5.6: Power transmitted through a linear polariser as a function of polariser orientation angle for the P_1 output of the Nd:YVO$_4$ source without the S-waveplate present in the cavity.

S-waveplate present in the cavity. The linear polarisation extinction ratio in this case is 280:1, which is likely limited by error in the measurement as the minimum power transmitted through the polariser was effectively zero. While there is no polarisation control elements in the laser, the gain of Nd:YVO$_4$ is extremely dependent on polarisation. This means that the laser crystal itself acts to preferentially select linear polarisation, which is one of the main reasons that this crystal was chosen. The polarisation extinction ratio was the same from output P_2. The same measurement of the polarisation extinction ratio was taken at output P_1 with the S-waveplate present in the cavity. Figure 5.7 is a graph of this data. It is immediately obvious that the linear polarisation of this output is not as pure as it was without the S-waveplate in the cavity, as the minimum power transmitted is a significant fraction of the maximum power. The polarisation extinction ratio was measured from this data to be
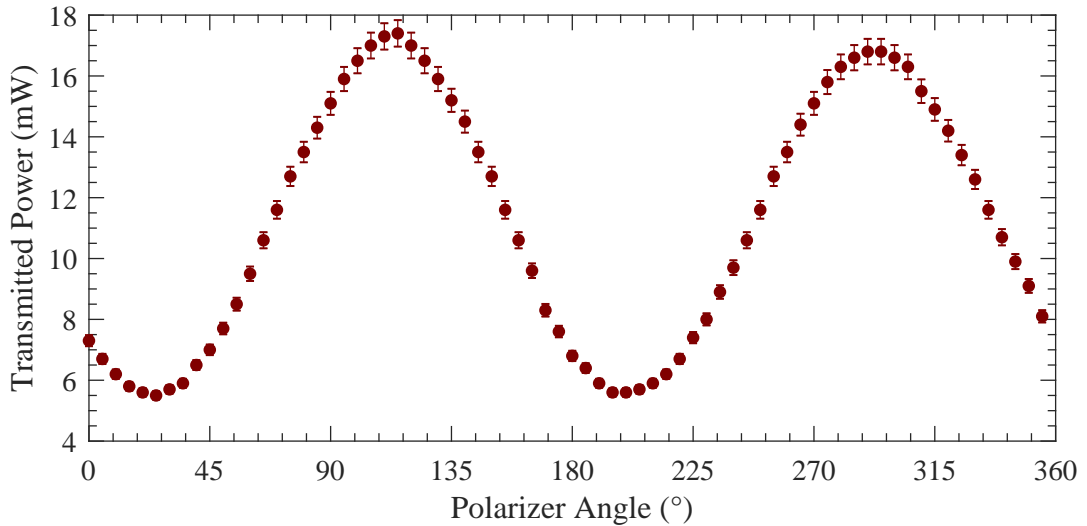
FIGURE 5.7: Power transmitted through a linear polariser as a function of polariser orientation angle for the P_1 output of the Nd:YVO$_4$ source with the S-waveplate present in the cavity.

3:1. The retardance values of the waveplate are likely slightly off specification at some azimuthal coordinates, as evidenced by the spatial dependence of the power transmitted through a linear polariser, shown in figure 5.4c. As the retardance can be arbitrarily tuned this was not seen as a significant problem, and could likely be corrected in future manufacturing of these S-waveplates.

The radial polarisation extinction ratio (RPER) was measured for output P_2 when the S-waveplate was present in the cavity, using the same method as described in section 3.1.4. At a source output power of 250 mW the RPER was measured at 35:1. While not as high as the RPER of the radially polarised mode produced from the source in chapter 3, this is still high enough to be considered an acceptable radially polarised mode. Should the retardance of the S-waveplate be optimised in future experiments the RPER will likely only improve.

5.3.3 Power Characteristics

The output power of the source was measured as a function of the absorbed pump power for a cavity without the S-waveplate, with the S-waveplate, and with the cavity mode propagating through a part of the substrate which did not have any femtosecond written alterations to it, which is denoted 'AR substrate' from here on. The maximum slope efficiencies were found for output-coupler reflectivities $R_1 > 99.5\%$ and $R_2 = 85\%$. Figure 5.8 shows this data. Overall the data are very linear, and behave as one might expect a solid-state laser to in terms of power characteristics. The slope efficiencies overall are lower than one might expect for a Nd:YVO$_4$ source, this may be due to a slight mismatch of the pump profile with the cavity mode. The important result to take from this graph is the small effect that the introduction of the waveplate has on the slope efficiencies and thresholds. The slope efficiency
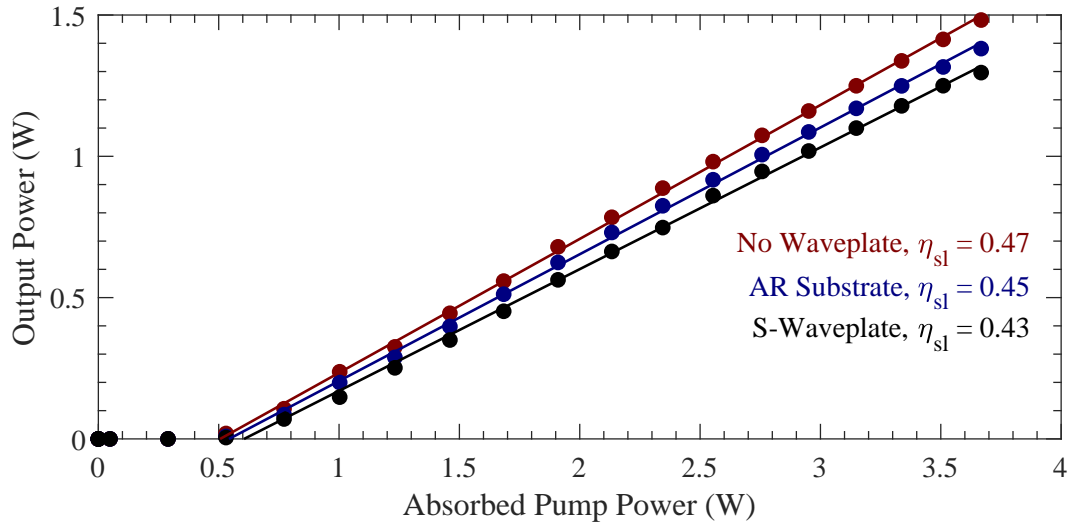
FIGURE 5.8: Output power of the Nd:YVO$_4$ source plotted against the absorbed pump power for the case of no intracavity waveplate, an AR coated substrate, and the intracavity S-waveplate. The maximum slope efficiencies shown were achieved with output coupler reflectivities R$_1$>99.5% and R$_2$=85%

of the basic cavity was measured as 47%, for the AR coated substrate it was 45% and for the S-waveplate it was 43%. The threshold absorbed pump powers were 0.51 *W*, 0.54 *W* and 0.61 *W* for the cavity without waveplate, AR substrate and the S-waveplate respectively. This is a first indication that the S-waveplate has a very low loss at the operating wavelength. The linearity of the data is also an indication that with more available pump power this source could achieve a higher output power without significant detriment.

5.3.4   Beam Quality Measurements

The beam quality parameter (M^2) of the source was measured at outputs P_1 and P_2 at a combined output power of 250 *mW* with and without the S-waveplate present in the cavity. The method used was identical to the one described in section 3.1.4. The data is presented in four graphs in figure 5.9, which are titled with output 1, output 2, waveplate and no waveplate to denote measurements of the beam diameter as a function of axial position for outputs P_1 and P_2 with and without the S-waveplate in the cavity respectively. Overall the measured M^2 parameters are close to the intended 2.0, with the largest measured values being 2.6. These inflated M^2 values may be able to be explained by the presence of some higher order modes. If the cavity length was increased by only a few millimetres the output mode began to have significant power present in the LG_{02} mode, so it is likely that some component of this mode was present and indistinguishable on the CCD images from the LG_{01} mode when the cavity was returned to the designed length. Without the S-waveplate in the cavity the M^2 in the y axis appears higher for output P_1 than it does for output P_2. This can partially be explained by the poor fit of the polynomial for the M^2
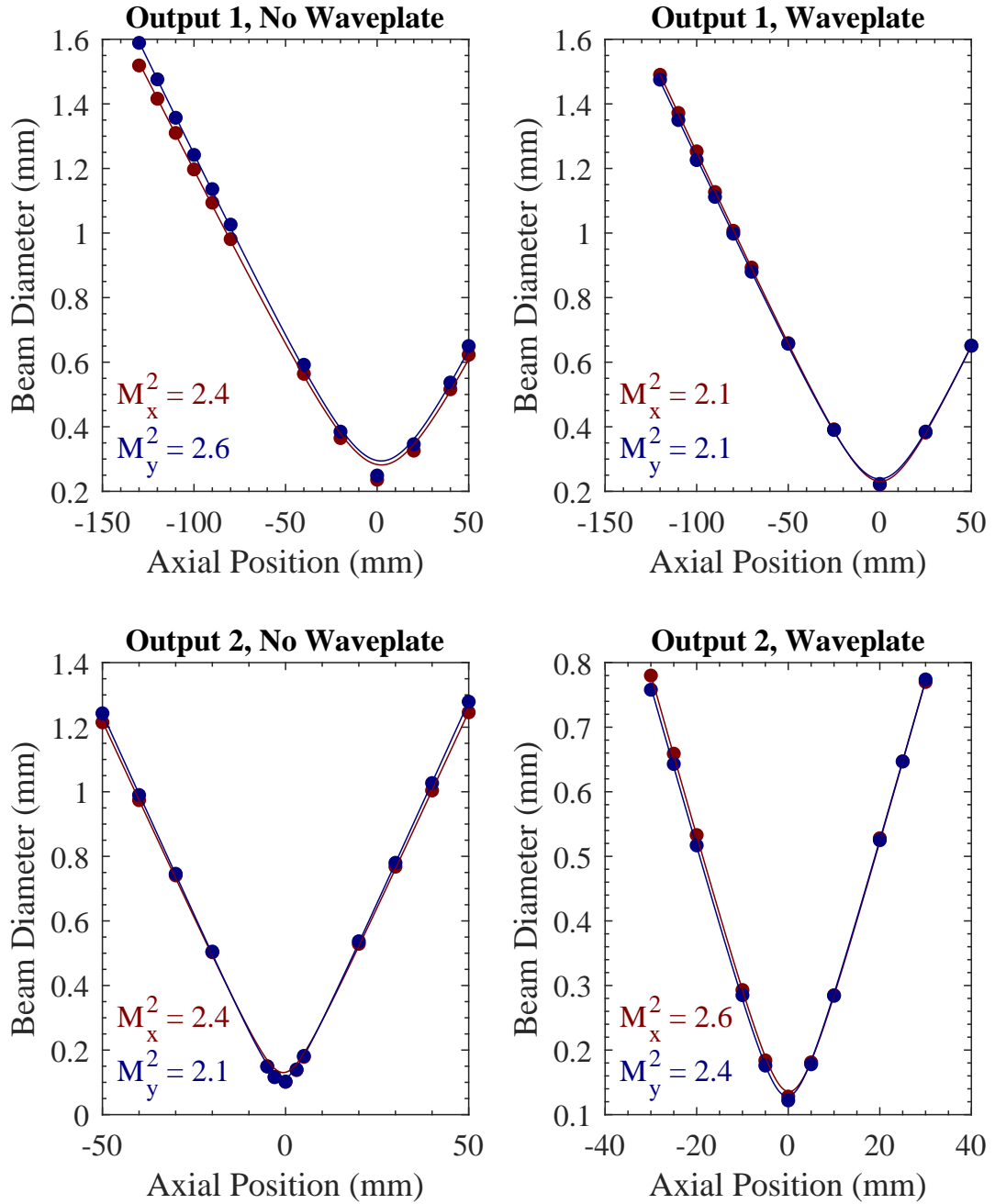
FIGURE 5.9: Beam quality factor measurements for the Nd:YVO$_4$ source in sagittal (x) and tangential (y) axes for outputs P$_1$ and P$_2$ with and without the S-waveplate in the cavity.

in both axes for output P_1, however there was another suspected factor. As a CCD camera was used to measure the beam diameters of these higher-order modes there was some degree of 'CCD bloom' present during the measurements. High power near-infrared light incident on a silicon based CCD device can cause some leakage of light through to the electronic components, which can cause phantom intensity to appear in a streak on one axis [225]. This has been shown to increase the M^2 on that axis when calculating beam diameters based on the second-moment integration method [226]. While efforts were taken to decrease the effect of this blooming, such as attenuation of the beam and increasing the exposure time of the camera, this blooming will have a small effect on the obtained M^2 parameters.

The important result to take from these measurements is that the introduction of the S-waveplate does not significantly increase the M^2 of the output modes upon its inclusion in the cavity. The graphs showing the M^2 for output P_1 with the S-waveplate included shows similar beam diameters at similar axial positions, while the M^2 parameter is smaller on both axes. The polynomial fit is better for this data, which in part is the cause of the reduced M^2. However, this may be evidence for the S-waveplate controlling the power leakage into higher-order modes than the desired first-order mode. As the retardance distribution of the S-waveplate was written in order to convert linear polarisation to the first order radially polarised mode, the second-order radially polarised mode will not be converted to a linearly polarised mode of the same orientation as the conversion of the first-order mode. This means that the higher-order modes will likely experience reduced gain as they pass through the Nd:YVO$_4$ crystal and will therefore be suppressed.

The M^2 was slightly higher on both axes for the radially polarised output P_2 when the S-waveplate was in the cavity, however the increase is not significant enough to cause concern. In fact, the measurement of these M^2 parameters as slightly different for both outputs with the inclusion of the S-waveplate in the cavity when compared to the S-waveplate not being in the cavity raises the question as to the use of this measurement for quantifying higher-order laser modes. Both outputs had distortions added to the output modes from the addition of the S-waveplate in the cavity, however these are not reflected in a consistent way in the M^2 measurements.

5.3.5   Findlay-Clay Loss Measurements

The loss of the S-waveplate was of great interest in order to compare it against previous generations of the femtosecond writing process. A direct single-pass measurement of the loss can be heavily inaccurate and does not reflect the performance of the S-waveplate in its intended application. In this section the application of a method for the determination of the internal losses of a four-level laser which was developed by Findlay and Clay is reported [227]. This method gives the total loss of a laser resonator in a steady-state. By rearranging the mathematics for the output power of a four-level laser system and assuming the intracavity loss, $\delta \ll 1$, one can obtain the

following expression (for a full derivation see [5])

$$- \ln R = \left(\frac{2\eta}{P_s} \right) P_{th} - \delta \tag{5.1}$$

where R is the combined output coupler reflectivity, η is an efficiency factor, P_s is the saturation power, P_{th} is the threshold absorbed pump power and δ is the intracavity loss. The relationship between $- \ln R$ and P_{th} should therefore be linear; if one plots $- \ln R$ against P_{th} the intracavity loss may be measured by finding the intercept with the y axis.

Experimentally, this means varying the output coupler reflectivity of a laser and measuring the threshold pump power for each reflectivity. One method of doing this is by the use of a Brewster-angled window inside the laser cavity. At Brewster's angle, the window will have close to zero reflectivity assuming that the incident beam has correctly aligned polarisation. By deviating the angle of the window from Brewster's angle the reflectivity of the window will increase as a function of the angular deviation. A schematic of this experimental arrangement is shown in figure 5.10. In this experiment, there are four outputs which are denoted P_1 and P_2 as

FIGURE 5.10: Experimental arrangement for measurement of the S-waveplate loss.

before, and P_3, P_4 for the outputs introduced by the inclusion of an uncoated fused-silica window orientated at approximately Brewster's angle. A half-waveplate at 1064 *nm* was introduced into the cavity before the fused-silica window in order to rotate the axis of the linear polarisation to minimise the reflectivity of the Brewster-angled window. Brewster's angle was found experimentally by optimising the angle of the fused-silica window and the orientation of the half-waveplate while the laser was operating such that the output powers P_3 and P_4 were close to zero. The angle of the fused-silica window was then deviated from this angle with the aid of an opto-mechanical rotation stage. At each angular deviation the output power was

measured from each output as a function of the input pump power. The threshold pump power was also measured at each deviation by recording the input pump power necessary to first see relaxation oscillations in the laser output.

The total reflectivity, R, was obtained using a simplification of the expressions first derived by Rigrod [228]. The relationship between the generalised output power P_a from a cavity optic of reflectivity R_a and the output power P_b from another reflectivity R_b can be expressed as

$$\frac{P_a}{P_b} = \frac{1 - R_a}{1 - R_b} \sqrt{\frac{R_b}{R_a}}. \tag{5.2}$$

If we now take the reasonable assumption that $\sqrt{R_b/R_a} \approx 1$ we can obtain R_b as a simple expression of P_a, P_b and R_a

$$R_b = 1 - \frac{P_b(1 - R_a)}{P_a}. \tag{5.3}$$

This expression allows for the calculation of the reflectivity of the Brewster-angled plate as a function of known and measurable quantities. In order to simplify the experiment the reflectivity R_2 was assumed to be 100% due to the inclusion of a highly reflective cavity mirror in this position. Only one output coupler was used, R_1 which was chosen to be 97.7%. By measuring the power from all output coupling optics, the total output coupling reflectivity from both surfaces of the Brewster-angled window combined was calculated using

$$R_{Brewster} = 1 - \frac{(P_3 + P_4)(1 - R_1)}{P_1} \tag{5.4}$$

The calculated reflectivity of the Brewster-angled window was averaged over many values of P_1, P_3 and P_4 obtained over different pump powers. Finally, the total output coupling reflectivity of the source was calculated as $R = R_1 R_{Brewster}$. The experiment was performed with no S-waveplate in the cavity, with a reference AR coated substrate in the cavity and with the S-waveplate in the cavity. The comparison between the total cavity loss in each case will allow for the calculation of the loss of the S-waveplate structure itself.

Figure 5.11 is a graph of the calculated $-\ln R$ against the measured threshold absorbed pump power for each angle of the window. The y intercept is measured for each data set and displayed as δ on the graph. The loss of the S-waveplate is therefore extremely low, as the difference between the calculated losses of the S-waveplate and the substrate it is written on is only $0.4 \pm 1.2\%$. While the error on this measurement is high compared to the value obtained for the loss of the S-waveplate, it allows for a confident statement that the S-waveplate has an extremely low loss when used as an intracavity polarisation converter at 1064 nm.
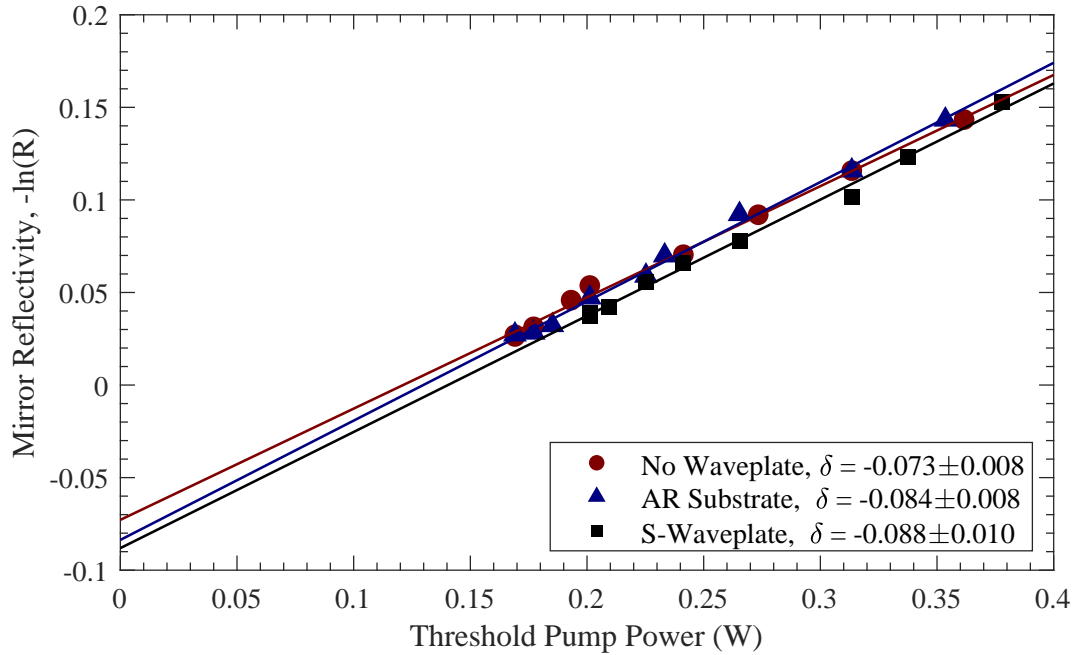
FIGURE 5.11: Plotted measurements of the threshold pump power of the Nd:YVO$_4$ source for a range of total cavity mirror reflectivities for no waveplate, an AR coated substrate, and the S-waveplate following the Findlay-Clay method. Determination of the y intercept allows for a measurement of the intracavity loss in each case enabling a measurement of the loss of the S-Waveplate.

5.4 Summary

A sample of a new generation of spatially variant waveplate was used as an intracavity polarisation converting element in a solid state Nd:YVO$_4$ laser operating at 1064 *nm* on a linearly polarised LG_{01} mode. The source was designed to have multiple interchangeable output couplers in order to observe the effect the S-waveplate had on the mode within the laser cavity. It was found that on one side of the cavity, before the S-waveplate that the output was linearly polarised with a polarisation extinction ratio of 3:1, while on the other side of the S-waveplate the output was radially polarised, with an RPER of 35:1. The effect of the inclusion of the S-waveplate on the cavity was explored by operating the source with no extra intracavity elements, the substrate that the S-waveplate was written in, and the S-waveplate. The inclusion of the S-waveplate was not found to significantly degrade the performance of the source. The optimal slope efficiency decreased by 2% due to the inclusion of the S-waveplate, the beam quality parameter was not consistently affected in each output, and the beam profiles suffered minor distortion while maintaining recognisable LG_{01} profiles. However, the linearly polarised output did decrease its polarisation extinction ratio from 350:1 to 3:1 due to the inclusion of the S-waveplate. It is believed that the spatially variant retardance of the S-waveplate may need optimisation that will easily remedy this problem. The loss of the S-waveplate relative

to the substrate it was written into was measured at just $0.4 \pm 1.2\%$ using a modified Findlay-Clay loss measurement technique. Overall the use of an intracavity S-waveplate shows great promise for the construction of robust and simple radially polarised lasers and may be scalable to much higher output power.

Chapter 6

Amplification of Annular Modes in a Thermally Guiding Fibre-Rod

This chapter details the amplification of the radially polarised and a vortex LG_{01} sources shown in chapter 3 with a thermally guiding fibre-rod. This hybrid geometry was introduced by C.R. Smith *et al.* in [229] for amplifying fundamental modes. In a simple description, the thermally guiding fibre-rod is a fibre with a large diameter core where the temperature based refractive index change enables the signal beam to be guided without interacting with the fibre waveguide. Pump light can be coupled into the core or an optional inner cladding. This design inherits the thermal and convenience benefits of fibres due to the relatively long length and large surface area while mitigating the problems associated with waveguide mode coupling, and the non-linear effects of small mode areas. The cylindrical symmetry and any birefringence being largely radial or azimuthal mean that the thermally guiding fibre rod naturally suits the amplification of radially polarised and vortex phase annular modes.

The chapter begins with a general theoretical model, an extension of the model in [229], of the radius and curvature of a higher-order mode as a function of fibre and thermal parameters and the propagation distance. This model allows for the calculation of an appropriate choice of input beam parameters and was used to inform the experimental design. The implementation of the fibre-rod using a commercial fibre is then described along with other device considerations. The experiment to amplify a radially polarised source with the fibre-rod is described, and data is presented showing the fibre-rod geometry well preserving the mode and polarisation properties. The experiment was repeated with a vortex phase Laguerre-Gaussian mode, and preliminary results show that the amplification is possible, with similar results to the radially polarised mode. The potential limitations, namely a significant amplified spontaneous emission content, a difficult alignment process and the effect of input beam quality are discussed along with the merits of this hybrid amplifier geometry.

6.1   The Thermally Guiding Fibre-Rod

6.1.1   Thermal Guidance Model

The non-uniform temperature distributions present in optical gain media results in a non-uniform refractive index profile through a range of thermo-optic effects. One of the most dominant effects observed is thermal lensing, where the change in refractive index at a position in a material is approximately proportional to a coefficient dn/dT, contributions from material stresses, and differential expansion. Silica has a positive dn/dT and therefore the temperature distributions seen in end-pumped cylindrical gain media create a focussing lensing effect for propagating light. This is usually encountered as a detrimental effect, however, it is also possible to use this lensing to guide a beam through a gain medium. The thermally guiding fibre-rod utilises this thermal lensing to propagate mode through the core of a large mode area fibre without interacting with the core/cladding interface.

C.R. Smith *et al.* developed a theoretical model to predict the evolution of the mode radius of an input beam as it propagates through the thermally guiding fibre-rod and to choose the appropriate experimental parameters [230]. An extension of this model is recorded here with a generalisation to higher-order modes. The key assumptions of the model are that stress and birefringence thermo-optic effects are small compared to the dn/dT contribution to thermal lensing, heat is generated in the fibre-rod core from the quantum defect of the optical pumping cycle, the heat flow is radial, and the pump deposition is transversely uniform across the core. The total refractive index of the thermally guiding fibre-rod is assumed to take the form

$$n(r,z) = n_0 - \frac{1}{2}n_g(z)r^2. \tag{6.1}$$

Here n_0 is the refractive index at the centre of the core and $n_g(z)$ is the radial variation in refractive index, given by

$$n_g(z) = n_{th}(z) + n_s, \tag{6.2}$$

where n_s is a static contribution to account for deviation of the core from a flat refractive index profile and $n_{th}(z)$ is the refractive index contribution arising from heat in the core.

By considering the temperature distribution arising from P_h, the pump power deposited as heat, in a rod of thermal conductivity κ, with uniform radial pump deposition density in a core of radius r_1, evaluating the effect of this temperature distribution on the refractive index and separating constant and temperature dependent terms, one can obtain an expression for $n_{th}(z)$.

$$n_{th}(z) = \frac{dn}{dT}\left(\frac{P_h(z)}{2\pi r_1^2 k dz}\right) \tag{6.3}$$

The transformation applied to a beam from transmission through a refractive index such as that in equations 6.1-6.3 may be modelled using the ray-transfer matrix for a graded index medium of length d, shown in equation 6.4 [10].

$$\begin{pmatrix} A & B \\ C & D \end{pmatrix} = \begin{pmatrix} \cos\left(z\sqrt{\frac{n_0}{n_g}}\right) & \frac{1}{\sqrt{n_0 n_g}}\sin\left(z\sqrt{\frac{n_g}{n_0}}\right) \\ -\sqrt{n_0 n_g}\sin\left(z\sqrt{\frac{n_g}{n_0}}\right) & \cos\left(z\sqrt{\frac{n_g}{n_0}}\right) \end{pmatrix} \tag{6.4}$$

A complex beam parameter, $q(z)$, is then defined in equation 6.5. The complex beam parameter contains important beam parameters: R is the beam radius of curvature, M^2 is the beam quality factor, λ the wavelength, and w the beam radius. $\Re$ and $\Im$ represent the real and imaginary parts of the complex beam parameter respectively.

$$q(z) = \left[\frac{1}{R(z)} - i\frac{M^2\lambda}{\pi w^2(z)}\right]^{-1} = \Re + i\Im \tag{6.5}$$

A matrix transformation may be performed upon an input complex beam parameter to obtain an output complex beam parameter. The beam radius and curvature after transmission through a distance z of fiber-rod may then be found by applying the transformation given in equation 6.4 to an input complex beam parameter, $\Re_{in} + i\Im_{in}$. This may be rearranged to obtain the output beam radius, w, and curvature, R, given in equations 6.6 and 6.7.

$$R = \frac{(A\Re_{in} + B)^2 + A^2\Im_{in}^2}{AC\Re_{in}^2 + AC\Im_{in}^2 + AD\Re_{in} + BC\Re_{in} + DB} \tag{6.6}$$

$$w = \sqrt{\frac{M^2\lambda}{\pi}\frac{(A\Re_{in} + B)^2 + A^2\Im_{in}^2}{\Im_{in}}} \tag{6.7}$$

If one then assumes that the input beam should be at a waist, w_0, it is possible to substitute equations 6.4 and 6.5 into equation 6.7 to obtain an expression for the beam radius in the fiber-rod as a function of z. The output beam radius from the fibre-rod device may be calculated from 6.8 by setting z equal to the fibre length.

$$w(z) = \sqrt{w_0^2 + \left(\frac{(M^2)^2\lambda^2}{n_0 n_g \pi^2 w_0^2} - w_0^2\right)\sin^2\left(z\sqrt{\frac{n_g}{n_0}}\right)} \tag{6.8}$$

This sinusoidal expression mathematically describes the interplay between diffraction and thermal focussing causing the beam radius to oscillate along the length of the fibre-rod. The period of this oscillation is $\pi\sqrt{n_0/n_g}$. There is, however, a value of the input beam waist w_0 for which the beam radius does not oscillate; this optimum beam waist is found by setting $w(z) = w_0$ in equation 6.8 and solving for w_0,

producing equation 6.9.

$$w_0 = \left(\frac{\left(M^2\right)^2 \lambda^2}{n_0 n_g \pi^2} \right)^{\frac{1}{4}} \tag{6.9}$$

In the case that thermal guiding dominates over any static contribution ($n_{th} \gg n_s$) the condition for constant beam radius simplifies to

$$w_0 = \left(\frac{2 r_1^2 \kappa \left(M^2\right)^2 \lambda^2}{\pi n_0 P_h(z) dn/dT} \right)^{\frac{1}{4}}. \tag{6.10}$$

In the case of end-pumping the pump deposition is not in reality a uniform function of z, instead it may be described by

$$P_h(z) \approx \alpha_p P_{in} exp(-\alpha_p z) \tag{6.11}$$

where γ is the fraction of absorbed pump power converted to heat, α_p is the absorption coefficient and P_{in} the input pump power. This approximation of the pump power heat deposition distribution assumes the ground-state depletion is negligible. From equation 6.10, one can see that a varying heat deposition, P_h, along the length of the device will also result in a value for the non-oscillating w_0 that changes along the device. In essence, the beam radius decreases at the pump input end of the device. Deviation from a beam waist of w_0 at the input will result in an oscillation of the beam radius with respect to distance propagated in the device with a position dependent period given by

$$\Delta z = \sqrt{\frac{2 \pi^3 r_1^2 n_0 \kappa}{P_h(z) dn/dT}}. \tag{6.12}$$

An issue with the TGFR is apparent. There is a limit to device length, as there needs to be enough heat to guide the mode. For a single-pass the fibre rod therefore needs to be shorter than a length for efficient absorption, which decreases the efficiency of the amplifier. To combat this the unabsorbed pump light could be recycled for a second pass or a double-end pumping arrangement could be used. In any case, the fibre-rod length needs to be selected in order to create a relatively uniform thermal profile along the length.

The calculated beam radius as a function of z for a mode of M^2 of 2.0 propagating through a 100 *mm* long fibre-rod is shown in figure 6.1. Three different pump power scenarios are shown for a 95 μm radius seed introduced at $z = 0$ *mm*. 915 nm pump light is introduced at the signal output end of the fibre-rod at $z = 100$ *mm* and therefore propagates in the opposite direction to the seed beam. The fibre-rod is cooled by direct contact between two water-cooled aluminium v-grooves in an effort to ensure radial heat-flow. The material properties are assumed to be that of silica, with thermal conductivity 1.38 $Wm^{-1}K^{-1}$ [231], and the change of refractive index with temperature 12.9 $\times 10^{-6} K^{-1}$ [232]. Previous work by Smith *et al.* [230] on the
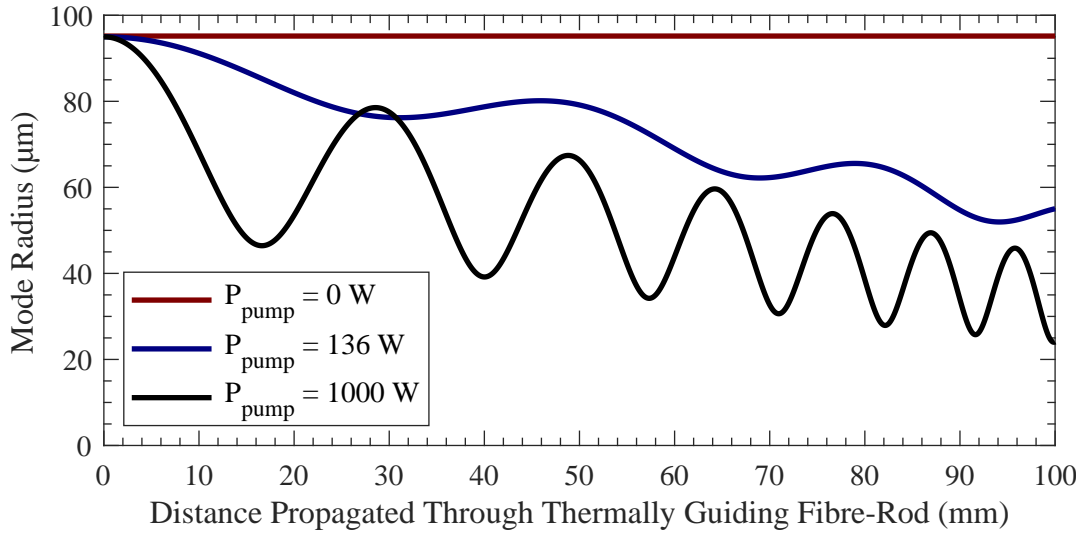
FIGURE 6.1: Modelled evolution of the mode radius of a first order annular mode input into a thermally guiding fibre-rod at a beam waist of 95 μm with counter propagating pump light for the scenarios of 0, 136, and 1000 W pump power.

same fibre indicated the presence of a static weakly guiding refractive index profile in the core. The value of n_s was assumed to be 3600 m^{-2} from their experiments.

In the absence of pumping, this value of n_s yields an optimum input beam waist of 95 μm from equation 6.8 for a beam of $M^2 = 2.0$ at a signal wavelength of 1030 nm. This is shown by the straight red line in figure 6.1 for $P_{pump} = 0$ W. 95 μm was therefore selected as a target beam waist for experimental demonstrations to simplify the initial alignment process. The effect of the anticipated maximum pump power coupled into the fibre-rod on the behaviour of the mode radius as it propagates through the length of the fibre rod is shown by the blue line at $P_{pump} = 136$ W. The mode radius decreases on average with distance propagated through the fibre-rod due to the heat-loading being higher at the pump input end. The mode radius also oscillates as expected, periodically diverging and focussing due to an interplay between diffraction and thermal lensing.

The important outcome of this model is that a higher-order mode is able to propagate through the core of the fibre-rod given parameters expected in an experimental demonstration. The average mode radius at a pump power of 136 W is predicted to be ≈ 73 μm. The mode is not predicted to interact with the core-cladding interface of the LMA fibre at a radius $r_1 = 150$ μm.

Another pump power scenario is shown in figure 6.1 as a black line, for $P_{pump} = 1000$ W to analyse the behaviour of the fibre-rod at power levels desired for future experiments. As is predicted in the model and shown in figure 6.1, the amplitude of the mode radius oscillation with respect to z is increased with the higher pump power while the period decreases. The magnitude of these oscillations may be decreased by optimising the input beam parameters. The average mode radius at

1000 *W* of pump power was calculated to be $\approx 54\ \mu m$, which remains large compared to the typical mode sizes observed in single-mode high power fibre amplifiers. This aspect of the thermally guiding fibre-rod gives an optimism to avoiding limiting mechanisms such as non-linear effects in some regimes of operation.

6.1.2 Fibre-Rod Device Design

The thermally guiding fibre-rod was demonstrated using a commercially available triple-clad Extra-Large-Mode-Area (XLMA) fibre supplied by Nufern. The XLMA fibre had a Yb-doped circular core with a 300 μm diameter and 0.11 NA. The inner cladding was octagonal in shape, with a flat-to-flat distance of 400 μm. The outer cladding was again circular with a 480 μm outer diameter.
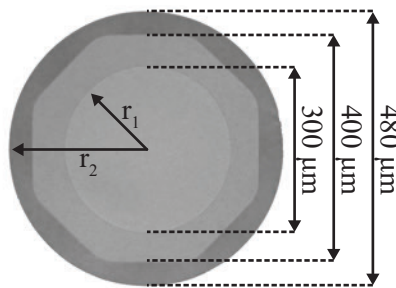
FIGURE 6.2: End-face microscope view of the Yb-doped triple clad fibre used in the thermally guiding fibre-rod amplifier device.

Figure 6.2 is a cross-sectional view of the Nufern XLMA fibre, with dimensions of the core and claddings annotated along with the definitions of the r_1 and r_2 radii. This fibre was chosen for its extremely large and uniform Yb-doped core. A 100 *mm* length of the fibre was used for a proof-of-concept demonstration of the amplification of higher-order modes. The fibre was supplied with a polymer coating that was removed for this experiment.

Rectangular fused-silica windows of dimensions $7 \times 7 \times 4\ mm$, with anti-reflection coatings for 915 to 1064 *nm* on one face were spliced to each end of the fibre-rod using a system designed and built by P.C. Shardlow. The purpose of the anti-reflection coated windows was to reduce loss and feedback when the fibre-rod is used as an amplifying medium. Firstly, the uncoated face of the fused-silica window was aligned parallel to the cleaved end-face of the XLMA fibre by observing interference fringes between the two closely spaced surfaces with a microscope objective. After alignment the fibre was moved clear of the fused-silica window; the axial position of the fibre was controlled using a micro-stepper motor for μm-scale positioning accuracy. The uncoated face of the fused-silica window was pre-heated with a $\sim 60\ W$, 10.6 μm CO_2 laser for a controlled time period. The beam from the CO_2 laser was split into two approximately equal beams using a beam splitter and directed onto the face of the fused-silica window such that the desired splicing position of the fibre-rod was flanked by the two beams. The anti-reflection coated opposite face was

FIGURE 6.3: The end-capped fibre-rod.

FIGURE 6.4: The end-capped fibre-rod mounted in a heat-sink.

cooled using a nitrogen gas jet during the heating process in order to avoid thermal damage. The fibre was then pushed into the hot region of the fused-silica window in a controlled manner and held for a short time with the CO_2 laser incident on the area around the fibre. This end-cap splicing process was repeated on the other end of the XLMA fibre. A completed end-capped fibre rod device is shown in figure 6.3.

The end-capped fibre-rod was mounted in a bespoke heatsink composed of two water cooled aluminium blocks with a v-groove cut into each. The fibre-rod was sandwiched in the two v grooves such that there were 4 points of contact with the circumference of the outer cladding along the entire length. An image of one end of the fibre-rod mounted in the heatsink is provided in figure 6.4. Beyond the obvious purpose of cooling the fibre-rod in an amplifier experiment, the heat-sink was designed to keep the fibre-rod as straight as possible as previous results by Smith *et al.* indicated that slight deviances from a straight device significantly degraded the output beam profiles [230].

6.2 Amplification of a Radially Polarised Mode

6.2.1 Experimental Configuration

With the fibre-rod having been successfully end-capped and mounted the experimental demonstration of the amplification of a radially polarised beam using the thermally guiding fibre-rod was performed. The schematic for this experiment is shown in figure 6.5. The radially polarised source detailed in section 3.1 was used as the seed source for this experiment. The red dashed line in figure 6.5 indicates the beam path of the radially polarised seed. The seed was conditioned to as close to the target 95 μm beam waist as possible through the use of a 100 mm focal length anti-reflection coated plano-convex focusing lens. This focusing lens was positioned

250 *mm* away from the 150 *mm* focal length collimating lens used in the radially polarised seed source. The resulting beam waist was verified using a Spiricon SP620U CCD camera as 97 *μm*, within error of the target beam waist. The converging seed beam was steered into the core of the fibre-rod using a highly-reflective dielectric mirror at 1030 *nm* and a short-pass filter that was highly reflective at wavelengths above 950 *nm*. Both the filter and the highly reflective mirror were orientated at a 45° angle with respect to the seed beam. The seed was aligned through the fibre-rod in the absence of pump light. This alignment was a difficult procedure that may present as a limitation of the fibre-rod architecture if an improved procedure or automation method cannot be established. The current alignment procedure [233] is best described as observing the output of the fibre-rod in the near and far-fields and iteratively adjusting the steering mirrors one axis at a time to reduce the complexity of the scrambled highly multi-mode output. After a great deal of effort the modal pattern can be reduced to a few-lobe structure that can be further finely adjusted to retrieve the original input mode. The reason for the increased difficulty in aligning the mode in the fibre-rod over a conventional fibre is the requirement for the mode to not interact with the core-cladding interface, meaning that the input angle and position must be within strict tolerances. Despite this difficulty the obtained output mode was very similar to the input mode in the absence of pump light and the alignment was stable over time.

A 155 *W* 915 *nm* fibre-coupled diode laser was used as the pump source. The pump light was delivered through a 105/125 *μm* 0.22 NA multi-mode fibre and is represented by a dashed blue line in figure 6.5. The pump delivery fibre output was imaged using two anti-reflection coated plano-convex lenses of focal lengths 50 *mm* and 100 *mm* in a 4f configuration to give a total magnification factor of 2. The converging pump light was steered into the core of the fibre-rod using a highly reflective dielectric mirror at the pump wavelength and a long-pass filter with a
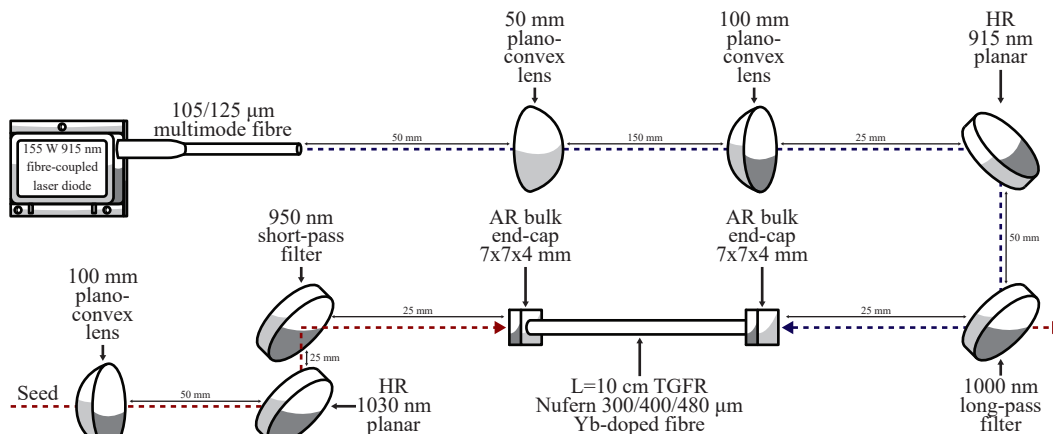

FIGURE 6.5: Schematic of the experimental arrangement used in the amplification of a radially polarised mode in a thermally guiding fibre-rod.

cut-off at 1000 *nm*, both orientated at 45° with respect to the pump beam. The inner cladding of the fibre-rod was not used in this experiment, but would allow for higher input pump power in future experiments using this fibre. The pump light completed a single pass of the 100 *mm* length of fibre-rod and is separated from the counter propagating seed by the 950 *nm* short-pass filter. 136 *W* was measured as the maximum pump power incident on the fibre due to a combination of the diode laser being below specification and loss from the 1000 *nm* long-pass filter.

6.2.2 Characterisation and Results

The radially polarised mode was recovered from the output of the thermally guiding fibre-rod over the full range of pump power. As the pump power changed the curvature of the mode at the output was seen to vary between converging and diverging several times, as expected from the theoretical model. Figures 6.6a and 6.6b show a comparison between the input radially polarised seed and the amplified output of the thermally guiding fiber-rod in the far-field for the maximum pump power of 136 *W*. Before amplification the radially polarised mode in 6.6a was of very high quality with a well defined annular profile and good central minimum, and free of severe aberrations or distortions. After amplification the mode pictured in 6.6b remained a high quality annular mode. There was no sign of coupling to the fibre modes. However, some slight distortion was introduced; the right-hand side of the mode in figure 6.6b shows some slight distortion, while the centre of the output mode appears enlarged compared to the input mode. These distortions are likely the result of misalignment, as aligning the input mode such that it propagates through the exact centre of the fibre-rod was difficult and lacked a reference position, or some deviation of the refractive index distribution from a cylindrical symmetry.

Figures 6.6c and 6.6d are images of the beam transmitted through a linear polariser, where 6.6d has been amplified. There is some minor distortion, disregarding the interference effects, as was seen from the amplified mode without being analysed by the linear polariser. Despite the slight distortion the desired two-lobe intensity profile is obtained with good results. There was no measurable decrease in the radial polarisation extinction ratio (RPER) when using the measurement technique described in section 3.1.4 on 36 polariser orientations; before amplification the RPER was 100:1 and after amplification it was unchanged. This is an encouraging result for the thermally-guiding fibre rod geometry, as it shows that higher-order radially polarised modes can be amplified with the polarisation unaffected by detrimental thermal effects. To apply some quantitative measure to the degradation of the mode caused by the amplification process the M^2 parameter of the amplified mode was measured. Figure 6.7a and 6.7b are graphs of the measured beam diameters of the amplified mode at maximum pump power as a function of axial position through a focus for the sagittal and tangential axis respectively. The M_x^2 parameter in the sagittal axis was measured as 2.2 ± 0.1 and in the tangential axis it was 2.1 ± 0.1. This is slightly higher than the M^2 of the seed source at 1.9 ± 0.1 but consistent with

(A) Radially polarised mode before amplification

(B) Radially polarised mode after amplification

(C) Radially polarised mode before amplification analysed by a linear polariser

(D) Radially polarised mode after amplification analysed by a linear polariser
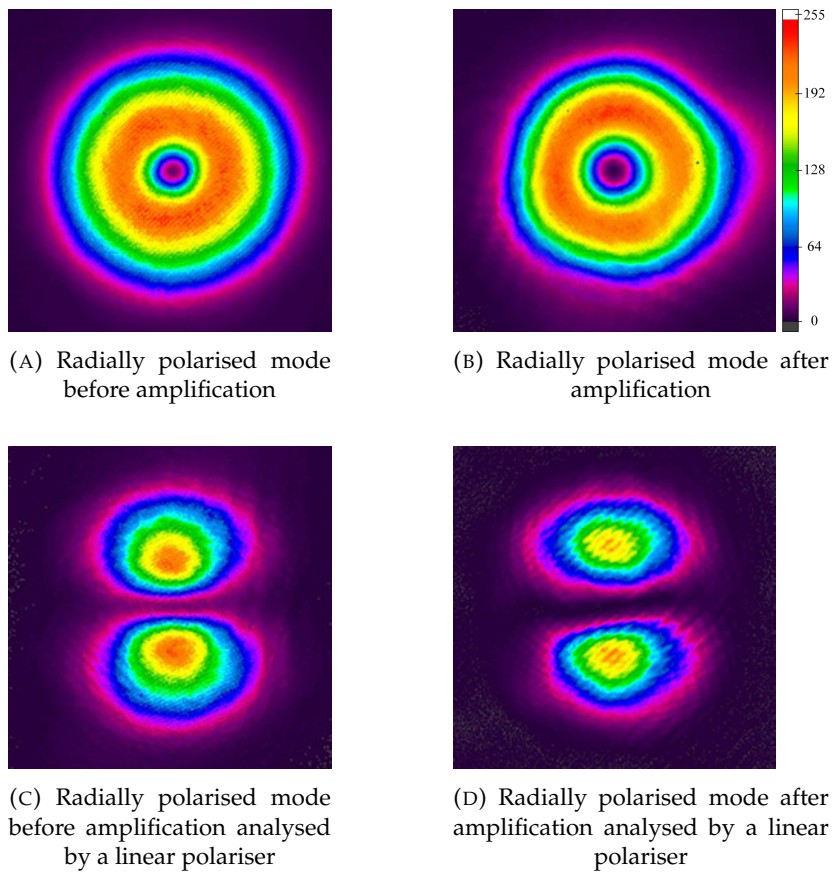
FIGURE 6.6: Intensity profiles of the radially polarised mode before and after amplification at the maximum pump power of 136 *W*, and the same beams as analysed by linear polarisers.

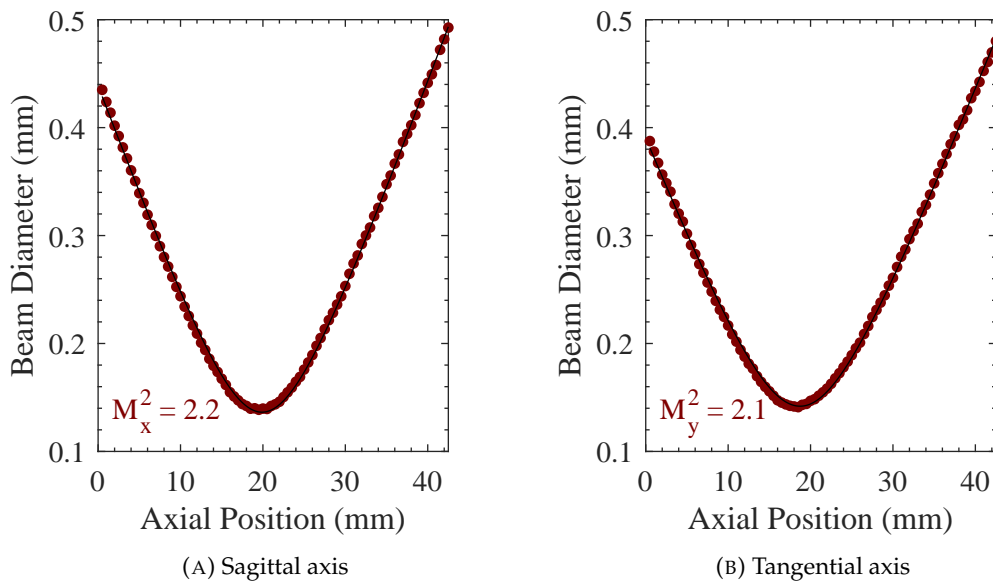(A) Sagittal axis

(B) Tangential axis

FIGURE 6.7: Beam quality factor measurements for the radially polarised mode after amplification at the maximum pump power of 136 *W* in the thermally guiding fibre-rod in sagittal (x) and tangential (y) axes.

the distortion observed in figure 6.6b and 6.6d. The slight increase in the M^2 is not judged to be a cause for concern regarding the thermally guiding fibre-rod architecture, and the encouraging result is that dramatic degradation that would indicate an interaction of the mode with the core-cladding interface is not observed.
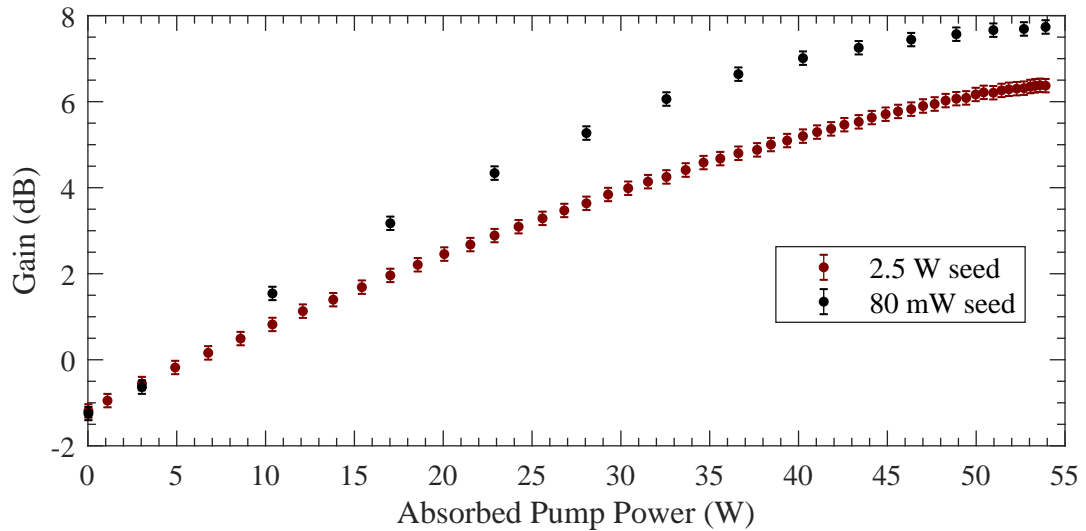
FIGURE 6.8: Gain of the thermally guiding fibre-rod amplifier plotted against absorbed pump power for a 2.5 *W* seed and an 80 *mW* seed power.

While this experiment was primarily a proof-of-concept demonstration that a radially polarised mode could be amplified with thermally guiding fibre-rod with a focus on maintaining beam quality and polarisation, the gain performance of the amplifier was studied for this short 100 *mm* length to explore future prospects. The power of the amplified radially polarised signal light was measured as a function of absorbed pump power in the fibre-rod for two input seed powers of 2.5 *W* and 80 *mW*; the data is shown in figure 6.8. The maximum signal output power was 10.7 *W* for an input seed power of 2.5 *W* at 54 *W* of absorbed pump power. The single-pass gain at this maximum output power is therefore calculated as 6.4 *dB* and the extraction efficiency as 20.6%. The maximum small-signal single-pass gain was measured as 7.7 *dB* for the 80 *mW* seed. The pump power required to reach transparency was approximately 6.7 *W* - this is shown as a negative gain below this power in figure 6.8 and is a result of the quasi-three level nature of Yb-doped silica having significant absorption at the lasing wavelength. Overall the gain and extraction efficiency are low, although to a certain extent this is expected from such a short length of fibre.

A more serious concern is the roll-over in the gain at the high range of absorbed pump power. This was a sign that some detrimental process was clamping the gain. Initial tests were carried out to rule-out detrimental thermal effects as the cause of the roll-over; quasi-continuous operation at low duty cycles of the pump source had no impact on the gain despite the reduction in the average heat load. The next investigation for detrimental effects was to measure the power spectrum of the seed

output end of the fibre-rod amplifier at maximum pump power for seeded and un-
seeded operation using an optical spectrum analyser. Broadband emission typical of
the presence of amplified spontaneous emission (ASE) was observed in both cases,
as shown in figure 6.9. This was a first indication that a significant amount of gain
was potentially being used up by ASE. Further evidence of significant ASE was ob-
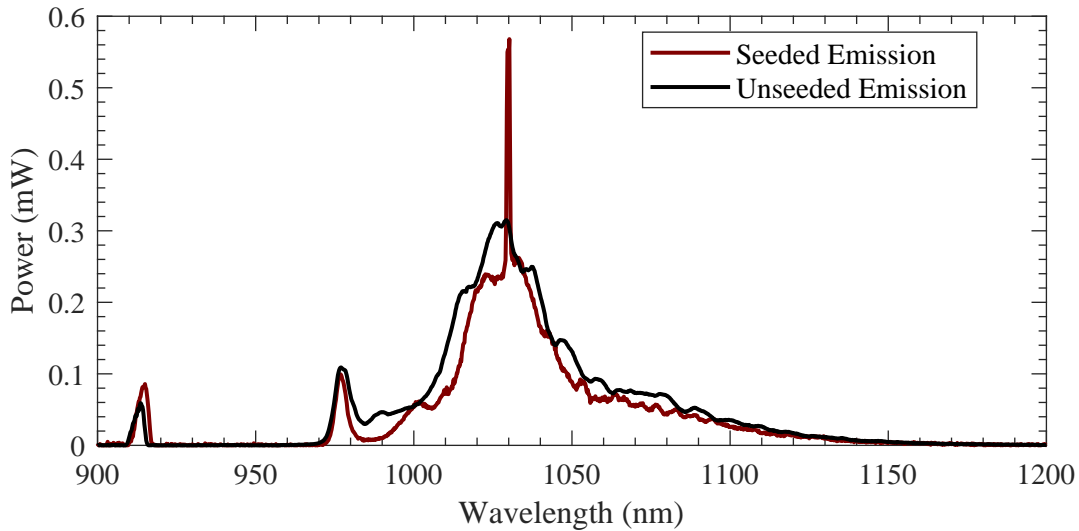
FIGURE 6.9: Power spectra of the seed output end of the thermally
guiding fibre-rod amplifier for unseeded and seeded cases at the max-
imum pump power of 136 *W*.

served by monitoring the power above wavelengths of 950 *nm* emitted from the seed
input end of the fibre-rod amplifier while the amplifier was pumped and seeded.
The data shown in in figure 6.10 reveals power unrelated to the pump or seed ex-
ponentially increasing with respect to the absorbed pump power in the fibre-rod
amplifier. This unattributed power becomes significant where the gain experienced
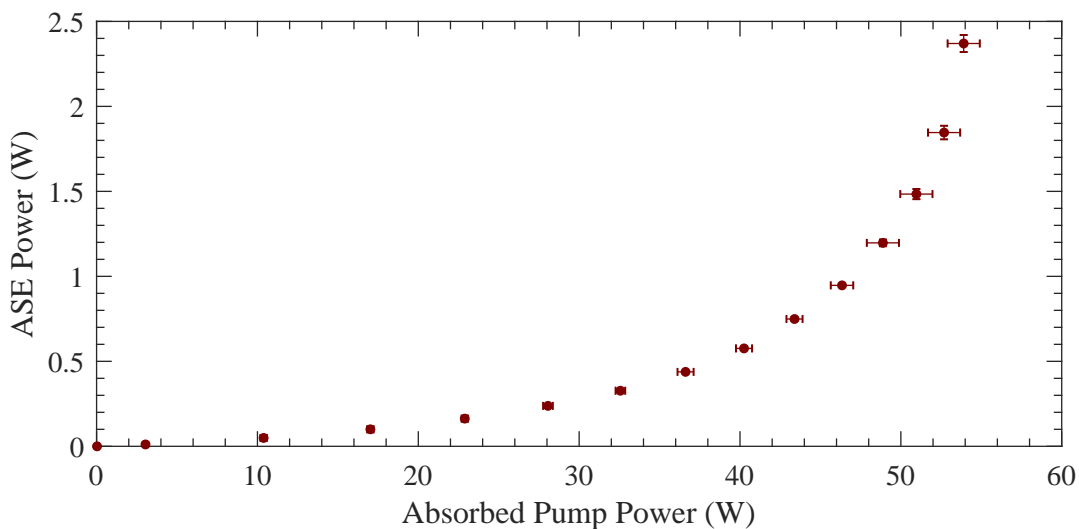
FIGURE 6.10: Single-aperture amplified spontaneous emission power
as a function of absorbed pump power in the thermally guiding fibre-
rod amplifier

by the radially polarised seed rolls over. This suspected ASE was highly divergent compared to the thermally guided radially polarised seed as it relied on the highly multi-mode step-index in-built waveguide of the fibre. The high divergence of the suspected ASE made it difficult to measure within the confines of the experimental set-up, therefore accurate measurements of the suspected ASE power in the seed output direction were not possible without significant changes to the experiment. Rough measurements of the suspected ASE power in the seed output direction with clipping on optics did however indicate a similar order-of-magnitude power level as the suspected ASE in the opposite direction that was shown in figure 6.10. The approximate amount of ASE power observed as emission from the fibre waveguide structure does not explain all of the unaccounted power. It is possible that the total ASE power contained in closed paths and transverse directions is much higher. Unfortunately, the Yb-doped XLMA fibre used in this fibre is predisposed to being susceptible to ASE in this regime of operation. This fibre is quasi-three-level in nature, the in-built waveguide is extremely multi-mode and ASE strength increases with the number of modes supported in a fibre [234]. In addition, this experiment used a low seed power and imperfect overlap between the pump and signal light, further compounding the likelihood of significant available gain being used by the ASE.

Several avenues are apparent for further power scaling and overcoming this ASE problem. The fibre-rod parameters can be engineered to give better pump and signal overlap in conjunction with a higher seed power to preferentially use the available gain. This could be achieved by using a fibre-rod with a lower dopant concentration for example. The thermally guiding fibre-rod has an advantage in that the ASE is guided by the in-built fibre waveguide while the signal is thermally guided. The extremely multi-mode fibre waveguide has a much higher output divergence than the thermal guiding, therefore spatial filtering could be used to effectively reduce the ASE power between stages in a multi-stage amplifier chain.

6.3   Amplification of a Laguerre-Gaussian Vortex Mode

A similar experiment to the amplification of a radially polarised mode using the thermally guiding fibre-rod was attempted with the Laguerre-Gaussian vortex mode source detailed in section 3.2. The aim of this experiment was to determine whether a cylindrically symmetric higher order mode with a different polarisation state could be propagated and amplified in the thermally guiding fibre-rod without significant degradation. This was successfully demonstrated with preliminary results, however due to time constraints a full investigation was unfortunately not possible.

6.3.1 Experimental Configuration

The experimental configuration was largely the same as was used for the experiment with a radially polarised seed discussed in section 6.2.1. The pump side of the experiment was identical, and the only modification that had to be made to couple the seed source in was a different magnification of the lens system. Figure 6.11 shows the experimental arrangement used for the amplification of the vortex mode. The
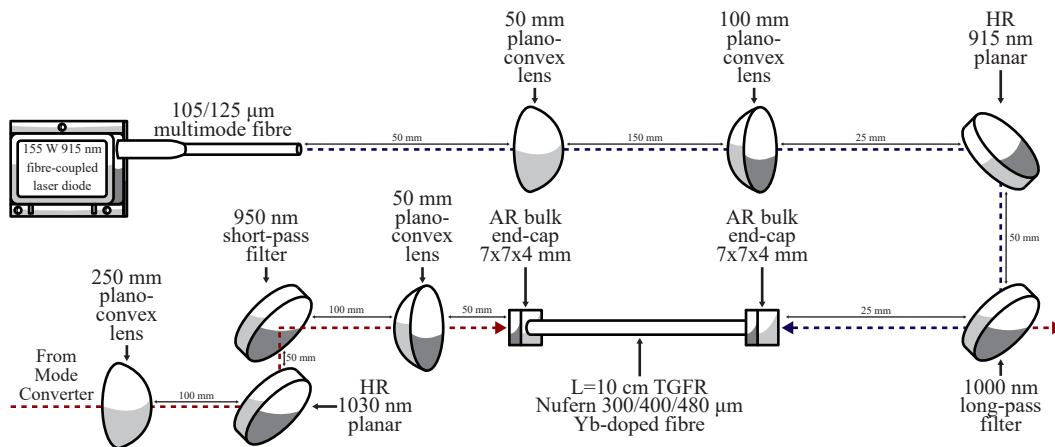
FIGURE 6.11: Schematic of the experimental arrangement used in the amplification of a Laguerre-Gaussian vortex mode in a thermally guiding fibre-rod.

HG_{01} source (section 3.2.1) was converted to a vortex LG_{01} mode using the spherical mirror mode converter (section 3.2.2). The output from the mode converter was collimated using a 250 *mm* focal length plano convex lens positioned approximately 300 *mm* from the second mirror of the mode converter. The collimated beam radius was measured to be 425 ± 10 *μm* when averaged over two axes. A 50 *mm* plano-convex focussing lens was positioned 300 *mm* from the collimating lens in order to give a magnification factor of 0.2. This conditioned the converted LG_{01} mode to have a beam waist radius of 85 *μm*; although this beam waist was not at the calculated optimum of 95 *μm* it was modelled to propagate in the absence of pump power without issue. Two seed beam steering mirrors were positioned between these two lenses in order to align the vortex mode into the core of the fibre-rod. One of these was a simple highly reflective mirror while the other was a 950 *nm* short-pass filter. In the interest of exploring the effect of the thermally guiding fibre-rod on the beam the seed power was kept to 210 *mW* to minimise the detrimental thermal effects observed at higher output powers. The pump side of the amplifier experiment was the same as described in section 6.2.1, namely a 155 *W*, 915 *nm* commercial fibre-coupled laser diode from which the output was coupled into the core of the fibre-rod with a magnification factor of 2.0.

6.3.2 Characterisation and Results

The LG_{01} mode was mostly recovered after amplification in the thermally guiding fibre-rod. Figure 6.12a is an image of the LG_{01} vortex mode before amplification, and is recreated here for direct comparison the the far-field mode amplified at maximum pump power shown in 6.12b. It is immediately obvious that the mode is not entirely preserved. In the amplified output from the fibre-rod there is a significant proportion of power that has visibly coupled into the fibre waveguide modes and therefore diverging away from a thermally guided component. It is also noticeable that the thermally guided component of the amplified output is a very clean and symmetrical annular mode, in contrast to the input mode which has some components or aberrations extra to the desired LG_{01} mode. The input mode appears to have four 'spurs' that are likely the result of thermal distortions having passed through the mode converter, and may have components of other transverse modes. Because the input beam parameters for these undesired components and aberrations were not accounted for in the design of the thermally guiding fibre-rod amplifier experiment a suggested explanation for the difference between the input and output modes is that these components interacted with the fibre waveguide. Despite a significant amount of power being lost to the fibre modes, the thermally guided component appears to be an excellent LG_{01} mode.

(A) Before amplification (B) After amplification
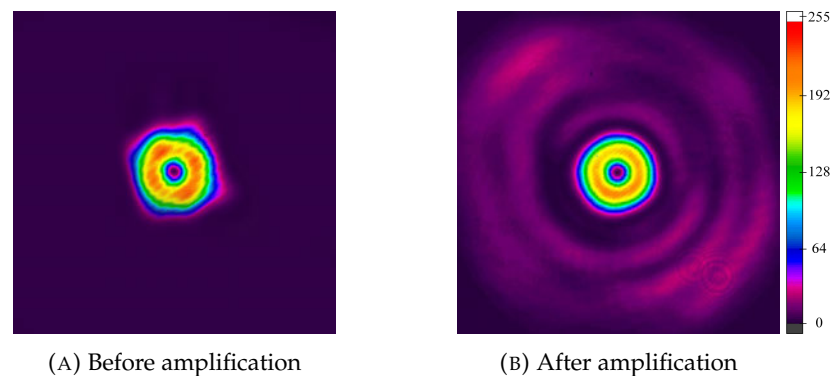
FIGURE 6.12: Intensity profiles of the LG_{01} mode before and after amplification at the maximum pump power of 136 W.

The gain performance of the thermally guiding fibre-rod amplifier was measured as a function of the absorbed pump power for the 210 mW vortex LG_{01} seed. This data is shown in figure 6.13. This data is at a glance similar to the gain data for the amplification of the radially polarised mode shown in figure 6.8, however the peak gain in figure 6.13 is noticeably lower than for both data sets in figure 6.8, at just 4.2 dB. The same roll-over caused by the high ASE was present in this experiment. The data is also more variable in figure 6.13 at the higher range of absorbed pump power. This is likely due to the large power content coupling into the fibre waveguide modes as shown in figure 6.12b, which due to its high divergence is not captured by the aperture of the power meter when aligned for the thermally guided component. To test this hypothesis a 50 mm focal length plano-convex lens was used
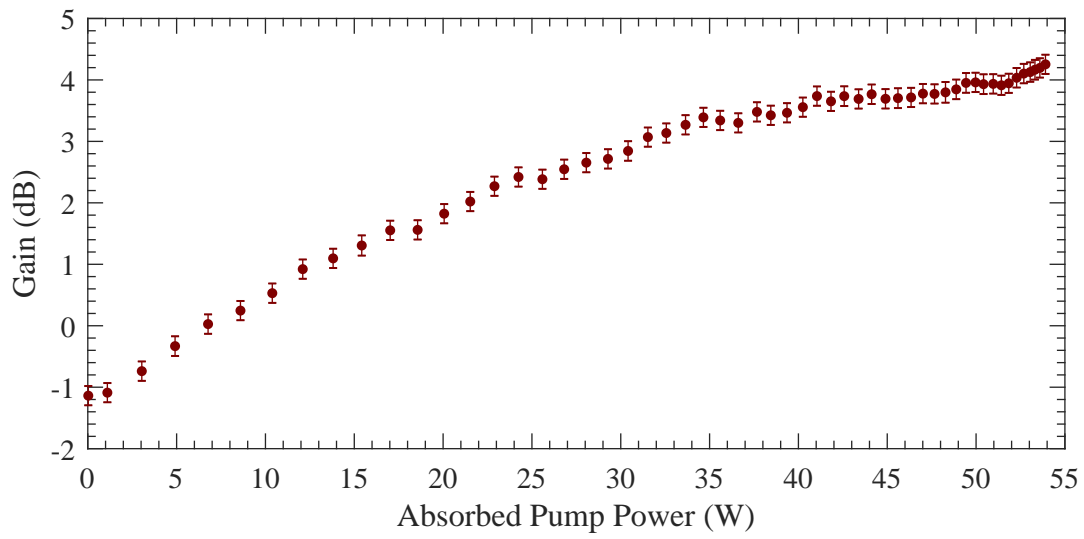
FIGURE 6.13: Gain of the thermally guiding fibre-rod amplifier plotted against absorbed pump power for a 210 mW LG_{01} seed.
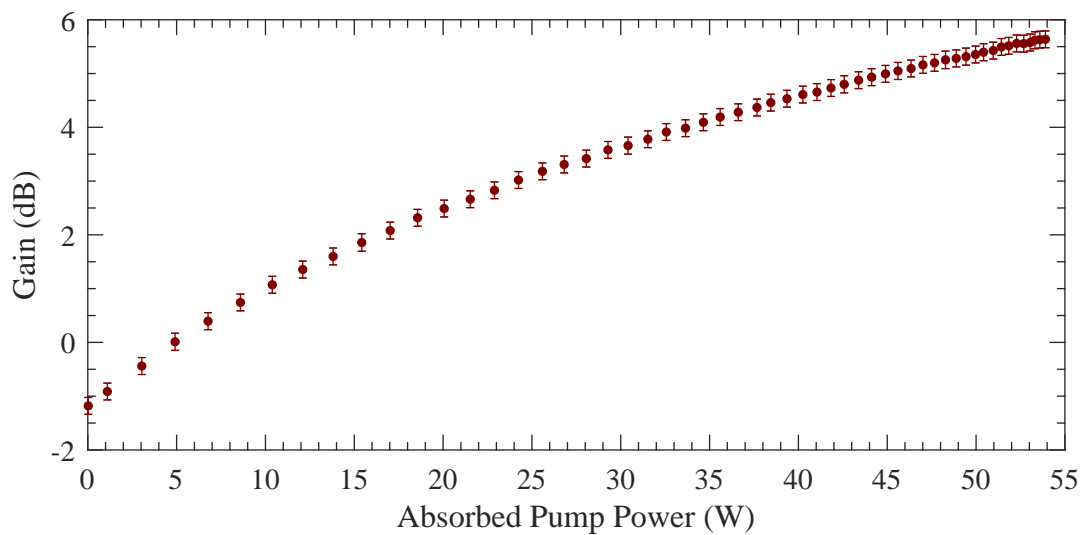
FIGURE 6.14: Gain of the thermally guiding fibre-rod amplifier plotted against absorbed pump power for a 210 mW LG_{01} seed, with an additional lens to capture light coupled into fibre waveguide modes.

to ensure the fibre waveguided component of the output was within the aperture of the power meter. The experiment was repeated, with the total output power shown in 6.14. The maximum gain, with the addition of the divergent fibre waveguide signal power, was similar to the maximum gain observed in figure 6.8 at a maximum of 5.6 dB. There was still some small amount of power lost through clipping on the 1000 nm long-pass filter, nevertheless, this measurement was sufficient to explain the lower gain experienced by the thermally guided component of the signal beam. The maximum output power was measured at 770 mW, corresponding to a power extraction efficiency of approximately 1%. This experiment confirmed that a vortex phase LG_{01} mode could be amplified in the thermally guiding fibre-rod with some coupling of input modal impurities to the fibre modes, yet further investigation is warranted into the effect of the input beam quality on the output beam and on the effect the amplification has on the phase of the LG_{01} mode.

6.4 Summary

The amplification of a radially polarised beam, and preliminary data of amplification of a vortex LG_{01} beam, was demonstrated in a thermally guiding fibre-rod. The 1030 nm radially polarised beam was successfully guided through the 300 μm core of a 100 mm length of Yb-doped Nufern XLMA fibre without interacting with the core/cladding interface using input beam parameters obtained from a model extended to higher-order modes. When pumped with a 155 W, 915 nm fibre-coupled laser diode the radially polarised mode was amplified with a peak gain of 7.7 dB for an 80 mW seed power and a maximum output power of 10.7 W for a 2.5 W seed power. The radially polarised mode was visibly well maintained after amplification, with the M^2 increasing from 1.9 ± 0.1 to 2.1 ± 0.1 agreeing that the beam quality was only slightly degraded. The radial polarisation purity was unchanged by the amplification process.

The data from the amplification of a vortex LG_{01} mode showed that although the mode was successfully propagated through the thermally guiding fibre-rod, a significant amount of power held in modal impurities and thermal aberrations in the input mode coupled into the fibre waveguide modes. The result was a visually high quality thermally guided annular mode with a highly divergent multi-mode component co-propagating with it. Gain measurements of the thermally guided component and the focussed output of the entire fibre output confirmed that a large amount of power was coupled to fibre modes and gave an indication that input beam quality is an important consideration for the thermally guiding fibre-rod.

A potential limitation from ASE was discovered in this iteration of the thermally guiding fibre-rod. A significant power in broadband emission was detected and explains a roll-over in signal gain observed in all of the amplification experiments. However, a large number of changes can be made to the fibre, input mode and experimental parameters to mitigate against this ASE. In addition, the thermally guiding

fibre-rod gives the ability to spatially filter the ASE, as it has a high divergence compared to the thermally guided signal light - this will be a key advantage in future multi-stage amplification experiments.

The main advantage demonstrated with this fibre-rod amplifier is the preservation of the polarisation and beam quality of the input mode with extremely large mode radii and good thermal performance. These benefits could provide a way to mitigate many of the drawbacks experienced by other amplifier geometries. Future experiments should explore the multi-stage amplification of higher-order modes at higher seed and pump powers with longer fibre-rod device lengths, in addition to exploring narrow linewidth or pulsed regimes of operation in order to evaluate the full potential of the thermally guiding fibre-rod.

Chapter 7

Conclusions

This research project began with broad aims: improve the obtainable quality and power of Laguerre-Gaussian vector and vortex modes. The introduction and background, chapters 1 and 2, introduced current generation methods and the huge range of applications of these exotic laser modes. The main limitations facing researchers in the field and the key innovations were reviewed. By considering the most pressing of these limitations, this thesis presented innovations in quantitative beam quality diagnostics, generation methods, and amplifier architectures for annular modes.

The first experimental chapter in this thesis, and indeed the first experimental work performed chronologically, was the construction of the first order radially polarised and vortex Laguerre-Gaussian mode sources written in chapter 3. The combination of existing techniques of gain shaping with an annular pump distribution, shaped via a capillary pump-delivery fibre, and thermally induced bifocussing proved very successful in enabling a high quality radially polarised mode from a free-space Yb:YAG laser. This source had an intensity profile very similar to a theoretical LG_{01} mode, and a high polarisation purity with a 'radial polarisation extinction ratio' of 100:1. The M^2 parameter was measured to be 1.9 ± 0.1 on both the x and y axis. The output power characteristics of this source exemplified one of the problems of generating cylindrical vector modes through thermally induced bifocussing. The highest power obtained at the optimum polarisation purity was $5.9\,W$. This source was very successful for its purpose; the output was a high quality radially polarised LG_{01} mode that was used heavily in other experiments.

The other source documented in chapter 3 was the HG_{01} free-space Yb:YAG laser that was converted to a vortex LG_{01} mode with an extracavity spherical mirror mode converter. While the double pump-spot approach used to operate on a HG_{01} source was initially developed by R. Uren and Q. Liu, an advancement to this method was the very easy and robust technique of placing the pump delivery fibres of two fibre-coupled laser diodes parallel alongside one another with the outer polymer layer stripped from one fibre. This method of positioning the fibres produced pump spots of the correct separation relative to the individual spot size in the case of commercial $105/125\,\mu m$ core/cladding standard multimode fibre, without the need for complex optomechanics or end-capping. The spherical mirror mode converter developed

by R. Uren was used to produce an acceptable vortex LG_{01} mode with a clearly observed handedness. Some impurities were visible in the obtained LG_{01} mode that were judged to be a result of distortions induced by the significant thermal lensing encountered in the Yb:YAG crystal, or inclusion of a small amount of other higher-order modes. The output power of the HG_{01}, and therefore converted LG_{01} mode, was limited to 210 mW before the thermal lensing produced unacceptable distortions in the mode, however the source could be pushed to an output of 2.5 W with a 57% slope efficiency before the output power rolled off. Despite the difficulties facing the generation of this vortex LG_{01} mode, it was suitable for study in further experiments.

As was explained in chapter 4, after encountering the problem of the lack of a good quantified metric of transverse modal purity, the machine learning algorithm *BeamNet* was developed that was able to provide modal composition predictions in real-time through the use of only a suitable camera and computer. The concept of a convolutional neural network and the training and development of *BeamNet* was included in 4, followed by theoretical end experimental evaluations of its performance. Somewhat astoundingly, *BeamNet* was able to predict the modal composition of 7384 previously unseen synthetic intensity profiles of incoherent superpositions of transverse modes in 340 ms, regardless of the number of modes, meaning the averaged computation time for a single image was just 49 μs. This represented a three order of magnitude decrease in computation times compared to the next best numerical method. The normalised root mean squared error established from this validation data set competed well with other methods, with values of 5.2% for a network trained on 10 modes, and 1.4% when trained on three modes. *BeamNet* was initially experimentally tested on the radially polarised source from chapter 3, proving suitable as a quantified alignment aid metric. A more thorough experimental test was the active stabilisation of a radially polarised Ho:YAG source with *BeamNet* being used to generate an error function for a feedback loop. The Ho:YAG laser exhibited variable transverse modes in the output when the pump power was varied; the output was robustly locked to either a fundamental mode or a radially polarised LG_{01} mode when the feedback loop was active. *BeamNet* is therefore a very promising candidate for quantifying the modal composition of a laser with very little specialist equipment and at camera-limited measurement frequencies. Suggested further developments should include the modelling of the near and far-field behaviour of superpositions of transverse modes and the subsequent training of *BeamNet* to more accurately diagnose modal composition through intensity profile analysis at multiple axial positions. The network structure itself could likely be optimised using more advanced methods and expertise. It would not take an extraordinary amount of work to implement convolutional neural networks like *BeamNet* into a robust and accurate measurement system for improved quantification of transverse laser modes, and into a wide range of laser systems. It would be particularly suited to application in beam shaping systems for industrial laser processing.

The use of a spatially variant waveplate (S-waveplate) fabricated using a refined

femotosecond direct laser writing process inside the cavity of a Nd:YVO$_4$ laser was reported in chapter 5. The laser was designed to preferentially operate on a linearly polarised mode with a LG_{01} intensity profile, and indeed a high quality annular mode with a linear polarisation extinction ratio of 280:1 was obtained at a maximum combined output power of 1.5 W at a 47% slope efficiency. The introduction of the S-waveplate in the cavity had the effect of causing the cavity to operate on a different mode either side of the waveplate. For this reason, the laser was built with two output couplers. A radially polarised LG_{01} mode with a high radial polarisation extinction ratio of 35:1 was obtained from one output and a linearly polarised output with a LG_{01} intensity profile from the other output. With the S-waveplate in the cavity the linearly polarised output had a polarisation extinction ratio of just 3:1. Both outputs had visual imperfections in the intensity profile as a result of the inclusion of the S-waveplate. Measurements of the M^2 parameter was were not conclusively increased by the inclusion of the S-waveplate, however the measurements were inconsistent values between 2.1 and 2.6 depending on the axis and output. The distortions added to the output modes by the S-waveplate were judged to have been caused by a slightly sub-optimal retardance distribution of the S-waveplate, which could be easily fine-tuned in future devices. The additional loss of the S-waveplate relative to the substrate it was written in was measured using a Findlay-Clay analysis to be just 0.4%. The fact that the S-waveplate induced such a small additional loss to the laser cavity gives a great deal of hope for the future use of this device in direct generation of high power radially polarised modes.

Finally, the radially polarised and the vortex Laguerre-Gaussian sources from chapter 3 were amplified in a thermally guiding fibre-rod as described by chapter 6. Both beams were successfully thermally guided through the 300 μm diameter core of the 100 mm long Yb-doped fibre-rod without relying on the in-built fibre waveguide for propagation. The peak gain obtained from this proof-of-concept fibre-rod amplifier was 7.7 dB, while the highest output power obtained was 10.7 W from a 2.5 W radially polarised seed. There was a large roll-off in the gain at the highest pump powers; the roll-off was thought to be due to significant ASE build up due to the measurement of several Watts of broadband emission from either end of the amplifier. The radially polarised mode was amplified with very little visual change in the intensity profile, with a minor distortion introduced, as evidenced by the M^2 increasing from 1.9 to 2.1 after amplification. The radial polarisation extinction ratio was unchanged when measured before and after amplification. The vortex Laguerre-Gaussian mode, while successfully amplified in a preliminary experiment, lost power to waveguide modes. Due to the visual observation that impurities of the input mode were removed after propagation through the fibre-rod, it was theorised that these impurities did not satisfy the carefully calculated guidance condition for the LG_{01} mode and were therefore coupled into waveguide modes. Overall, the thermally guiding fibre-rod was shown to be very capable of amplifying annular modes with very little degradation added to the output, although the input beam quality

requirements should be carefully studied and quantified in future experiments. The extremely large mode area and good thermal performance of the thermally guiding fibre-rod amplifier geometry should prove a promising candidate for the scaling of annular modes to much higher powers. Suggested future works should check the viability of longer device lengths, could include the amplification of pulsed annular mode sources, or demonstrate multi-stage amplification using several thermally guiding fibre-rods with spatial filters in between each stage to prevent ASE build-up.

Ultimately, this thesis has described the current state of research into generating high quality annular modes at significant output powers, identified several key problems and contributed novel research towards analysis, generation and amplification methods for these modes. With such a wealth of applications and recent advances there is a good deal of optimism that vortex and vector Laguerre-Gaussian modes will become commonplace in commercial, industrial and research environments.

An incredible amount was learned during the experimentation and writing of this thesis, hopefully this has been conveyed to the reader together with inspiration for their own work. Although this thesis is now at its end, it may serve as a beginning for others to produce some excellent research on these fascinating laser modes.

Publications

T. L. Jefferson-Brain et al. "Generation of a Radially Polarized Beam in a Solid-State Laser Using an Intracavity Spatially Variant Waveplate (withdrawn due to COVID-19)". In: CLEO 2020 San Jose. 2020.

T. L. Jefferson-Brain et al. "Control and stabilization of spatial mode quality in a radially polarized solid-state laser using machine learning". In: Solid State Lasers XXIX: Technology and Devices. Vol. 11259. International Society for Optics and Photonics. 2020, 112590F.

T. Jefferson-Brain et al. "Amplification of a radially polarized beam in a thermally guiding ytterbium-doped fiber rod". In: Applied Physics B 125.9 (2019), p. 167.

T. Jefferson-Brain et al. "Alignment of Higher-Order Mode Solid-State Laser Systems with Machine Learning Diagnostic Assistance". In: 2019 Conference on Lasers and Electro-Optics Europe & European Quantum Electronics (CLEO/Europe-EQEC). IEEE. 2019, pp. 1–1

T. L. Jefferson-Brain et al. "Generation and amplification of a LG01 laser with a thermally-guiding fiber-rod". In: Solid State Lasers XXVIII: Technology and Devices. Vol. 10896. International Society for Optics and Photonics. 2019, 108961A.

C. R. Smith et al. "Thermally guided ytterbium-doped fiber-rod laser". In: Solid State Lasers XXVII: Technology and Devices. Vol. 10511. International Society for Optics and Photonics. 2018, p. 105111I.

Bibliography

[1] T. H. Maiman. "Stimulated optical radiation in ruby". In: *Nature* 187.4736 (1960), pp. 493–494.

[2] M. Edwards et al. "Progress towards ignition on the National Ignition Facility". In: *Physics of Plasmas* 20.7 (2013), p. 070501.

[3] S. Stellmer et al. "Laser cooling to quantum degeneracy". In: *Physical Review Letters* 110.26 (2013), p. 263003.

[4] B. P. Abbott et al. "Observation of gravitational waves from a binary black hole merger". In: *Physical Review Letters* 116.6 (2016), p. 061102.

[5] W. Koechner. *Solid-State Laser Engineering*. 6th ed. Springer-Verlag New York, 2006.

[6] A. E. Siegman. *Lasers*. University Science Books, 1986.

[7] O. Svelto and D. C. Hanna. *Principles of lasers*. Vol. 1. Springer, 2010.

[8] W. A. Clarkson. "Solid State Lasers". Lecture notes, OPTO6002, University of Southampton. 2016.

[9] T Hansch, M Pernier, and A Schawlow. "Laser action of dyes in gelatin". In: *IEEE Journal of Quantum Electronics* 7.1 (1971), pp. 45–46.

[10] H. Kogelnik and T. Li. "Laser beams and resonators". In: *Applied Optics* 5.10 (1966), pp. 1550–1567.

[11] H Rubens and O Krigar-Menzel. "Flammenröhre für akustische Beobachtungen". In: *Annalen der Physik* 322.6 (1905), pp. 149–164.

[12] A. G. Fox and T. Li. "Resonant modes in a maser interferometer". In: *Bell System Technical Journal* 40.2 (1961), pp. 453–488.

[13] G. D. Boyd and J. P. Gordon. "Confocal multimode resonator for millimeter through optical wavelength masers". In: *Bell System Technical Journal* 40.2 (1961), pp. 489–508.

[14] G. D. Boyd and H. Kogelnik. "Generalized confocal resonator theory". In: *Bell System Technical Journal* 41.4 (1962), pp. 1347–1369.

[15] Q. Zhan. "Cylindrical vector beams: from mathematical concepts to applications". In: *Advances in Optics and Photonics* 1.1 (2009), pp. 1–57.

[16] A. E. Siegman. "How to (maybe) measure laser beam quality". In: *Diode Pumped Solid State Lasers: Applications and Issues*. Optical Society of America. 1998, MQ1.

[17]   A. E. Siegman. "New developments in laser resonators". In: *Optical Resonators*.
       Ed. by D. A. Holmes. Vol. 1224. International Society for Optics and Photon-
       ics. SPIE, 1990, pp. 2 –14. DOI: `10.1117/12.18425`. URL: `https://doi.org/`
       `10.1117/12.18425`.

[18]   L. Allen et al. "Orbital angular momentum of light and the transformation of
       Laguerre-Gaussian laser modes". In: *Physical Review A* 45.11 (1992), p. 8185.

[19]   R. A. Beth. "Mechanical detection and measurement of the angular momen-
       tum of light". In: *Physical Review* 50.2 (1936), p. 115.

[20]   C. Tamm and C. Weiss. "Bistability and optical switching of spatial patterns
       in a laser". In: *Journal of the Optical Society of America B* 7.6 (1990), pp. 1034–
       1038.

[21]   M. W. Beijersbergen et al. "Astigmatic laser mode converters and transfer of
       orbital angular momentum". In: *Optics Communications* 96.1-3 (1993), pp. 123–
       132.

[22]   D. G. Hall. "Vector-beam solutions of Maxwell's wave equation". In: *Optics
       Letters* 21.1 (1996), pp. 9–11.

[23]   C.-Y. Han et al. "Simple triangular path interferometer for generation of an in-
       homogeneously polarized beam". In: *Japanese Journal of Applied Physics* 48.9R
       (2009), p. 092402.

[24]   C. Rosales-Guzmán, B. Ndagano, and A. Forbes. "A review of complex vector
       light fields and their applications". In: *Journal of Optics* 20.12 (2018), p. 123001.

[25]   A. E. Willner et al. "Optical communications using orbital angular momen-
       tum beams". In: *Advances in Optics and Photonics* 7.1 (2015), pp. 66–106.

[26]   L. Zhu et al. "18 km low-crosstalk OAM+ WDM transmission with 224 in-
       dividual channels enabled by a ring-core fiber with large high-order mode
       group separation". In: *Optics Letters* 43.8 (2018), pp. 1890–1893.

[27]   M. Erhard et al. "Twisted photons: new quantum perspectives in high dimen-
       sions". In: *Light: Science & Applications* 7.3 (2018), pp. 17146–17146.

[28]   N. J. Cerf et al. "Security of quantum key distribution using d-level systems".
       In: *Physical Review Letters* 88.12 (2002), p. 127902.

[29]   A. Mair et al. "Entanglement of the orbital angular momentum states of pho-
       tons". In: *Nature* 412.6844 (2001), pp. 313–316.

[30]   M. Krenn et al. "Twisted photon entanglement through turbulent air across
       Vienna". In: *Proceedings of the National Academy of Sciences* 112.46 (2015), pp. 14197–
       14201.

[31]   A. Sit et al. "High-dimensional intracity quantum cryptography with struc-
       tured photons". In: *Optica* 4.9 (2017), pp. 1006–1010.

[32] W. Cheng, J. W. Haus, and Q. Zhan. "Propagation of vector vortex beams through a turbulent atmosphere". In: *Optics Express* 17.20 (2009), pp. 17829–17836.

[33] M. A. Cox et al. "On the resilience of scalar and vector vortex modes in turbulence". In: *Optics Express* 24.16 (2016), pp. 18105–18113.

[34] M. A. Cox et al. "The resilience of Hermite–and Laguerre–Gaussian modes in turbulence". In: *Journal of Lightwave Technology* 37.16 (2019), pp. 3911–3917.

[35] M. Gecevičius et al. "Single beam optical vortex tweezers with tunable orbital angular momentum". In: *Applied Physics Letters* 104.23 (2014), p. 231110.

[36] A. M. Yao and M. J. Padgett. "Orbital angular momentum: origins, behavior and applications". In: *Advances in Optics and Photonics* 3.2 (2011), pp. 161–204.

[37] M. Friese et al. "Optically driven micromachine elements". In: *Applied Physics Letters* 78.4 (2001), pp. 547–549.

[38] G. Knöner et al. "Integrated optomechanical microelements". In: *Optics Express* 15.9 (2007), pp. 5521–5530.

[39] K. Ladavac and D. G. Grier. "Microoptomechanical pumps assembled and driven by holographic optical vortex arrays". In: *Optics Express* 12.6 (2004), pp. 1144–1149.

[40] J. Leach et al. "An optically driven pump for microfluidics". In: *Lab on a Chip* 6.6 (2006), pp. 735–739.

[41] C Brabetz et al. "Laser-driven ion acceleration with hollow laser beams". In: *Physics of Plasmas* 22.1 (2015), p. 013105.

[42] Y. Wu et al. "Polarized electron-beam acceleration driven by vortex laser pulses". In: *New Journal of Physics* 21.7 (2019), p. 073052.

[43] J. R. Moffitt, C. Osseforth, and J. Michaelis. "Time-gating improves the spatial resolution of STED microscopy". In: *Optics Express* 19.5 (2011), pp. 4242–4254.

[44] L Yan et al. "Q-plate enabled spectrally diverse orbital-angular-momentum conversion for stimulated emission depletion microscopy". In: *Optica* 2.10 (2015), pp. 900–903.

[45] M. P. Lavery et al. "Observation of the rotational Doppler shift of a white-light, orbital-angular-momentum-carrying beam backscattered from a rotating body". In: *Optica* 1.1 (2014), pp. 1–4.

[46] M. Duocastella and C. B. Arnold. "Bessel and annular beams for materials processing". In: *Laser & Photonics Reviews* 6.5 (2012), pp. 607–621.

[47] S. Safdar et al. "Finite element simulation of laser tube bending: Effect of scanning schemes on bending angle, distortions and stress distribution". In: *Optics & Laser Technology* 39.6 (2007), pp. 1101–1110.

[48] C. E. Protasov and A. V. Gusarov. "Modeling the effect of beam shaping at selective laser melting". In: *Procedia IUTAM* 23 (2017), pp. 147–154.

[49] M. Rahimian et al. "Polarization dependent nanostructuring of silicon with femtosecond vortex pulse". In: *APL Photonics* 2.8 (2017), p. 086104.

[50] F. Takahashi et al. "Picosecond optical vortex pulse illumination forms a monocrystalline silicon needle". In: *Scientific Reports* 6 (2016), p. 21738.

[51] K. S. Youngworth and T. G. Brown. "Focusing of high numerical aperture cylindrical-vector beams". In: *Optics Express* 7.2 (2000), pp. 77–87.

[52] W. Chen and Q. Zhan. "Three-dimensional focus shaping with cylindrical vector beams". In: *Optics Communications* 265.2 (2006), pp. 411–417.

[53] G. M. Lerman, L. Stern, and U. Levy. "Generation and tight focusing of hybridly polarized vector beams". In: *Optics Express* 18.26 (2010), pp. 27650–27657.

[54] J. Chen, C. Wan, and Q. Zhan. "Vectorial optical fields: recent advances and future prospects". In: *Science Bulletin* 63.1 (2018), pp. 54–74.

[55] G. M. Lerman and U. Levy. "Effect of radial polarization and apodization on spot size under tight focusing conditions". In: *Optics Express* 16.7 (2008), pp. 4567–4581.

[56] D. Biss and T. Brown. "Polarization-vortex-driven second-harmonic generation". In: *Optics Letters* 28.11 (2003), pp. 923–925.

[57] S. Carrasco et al. "Second-and third-harmonic generation with vector Gaussian beams". In: *Journal of the Optical Society of America B* 23.10 (2006), pp. 2134–2141.

[58] D. P. Biss, K. S. Youngworth, and T. G. Brown. "Dark-field imaging with cylindrical-vector beams". In: *Applied Optics* 45.3 (2006), pp. 470–479.

[59] N. Bokor and N. Davidson. "Toward a spherical spot distribution with 4π focusing of radially polarized light". In: *Optics Letters* 29.17 (2004), pp. 1968–1970.

[60] R. Chen et al. "Imaging using cylindrical vector beams in a high-numerical-aperture microscopy system". In: *Optics Letters* 38.16 (2013), pp. 3111–3114.

[61] S. Segawa, Y. Kozawa, and S. Sato. "Demonstration of subtraction imaging in confocal microscopy with vector beams". In: *Optics Letters* 39.15 (2014), pp. 4529–4532.

[62] S. Segawa, Y. Kozawa, and S. Sato. "Resolution enhancement of confocal microscopy by subtraction method with vector beams". In: *Optics Letters* 39.11 (2014), pp. 3118–3121.

[63] Q. Zhan and J. R. Leger. "Focus shaping using cylindrical vector beams". In: *Optics Express* 10.7 (2002), pp. 324–331.

[64] N. Bhebhe, C. Rosales-Guzman, and A. Forbes. "Classical and quantum analysis of propagation invariant vector flat-top beams". In: *Applied Optics* 57.19 (2018), pp. 5451–5458.

[65] X. Li et al. "Three-dimensional orientation-unlimited polarization encryption by a single optically configured vectorial beam". In: *Nature Communications* 3.1 (2012), pp. 1–6.

[66] M. Michihata, T. Hayashi, and Y. Takaya. "Measurement of axial and transverse trapping stiffness of optical tweezers in air using a radially polarized beam". In: *Applied Optics* 48.32 (2009), pp. 6143–6151.

[67] Y. Kozawa and S. Sato. "Optical trapping of micrometer-sized dielectric particles by cylindrical vector beams". In: *Optics Express* 18.10 (2010), pp. 10828–10833.

[68] M. Donato et al. "Optical trapping of nanotubes with cylindrical vector beams". In: *Optics Letters* 37.16 (2012), pp. 3381–3383.

[69] B. J. Roxworthy and K. C. Toussaint Jr. "Optical trapping with π-phase cylindrical vector beams". In: *New Journal of Physics* 12.7 (2010), p. 073012.

[70] S. Skelton et al. "Trapping volume control in optical tweezers using cylindrical vector beams". In: *Optics Letters* 38.1 (2013), pp. 28–30.

[71] Q. Zhan. "Properties of circularly polarized vortex beams". In: *Optics Letters* 31.7 (2006), pp. 867–869.

[72] L. Huang et al. "Optical trapping of gold nanoparticles by cylindrical vector beam". In: *Optics Letters* 37.10 (2012), pp. 1694–1696.

[73] L Novotny et al. "Longitudinal field modes probed by single molecules". In: *Physical Review Letters* 86.23 (2001), p. 5251.

[74] M. Neugebauer et al. "Polarization-controlled directional scattering for nanoscopic position sensing". In: *Nature Communications* 7.1 (2016), pp. 1–6.

[75] F. K. Fatemi. "Cylindrical vector beams for rapid polarization-dependent measurements in atomic systems". In: *Optics Express* 19.25 (2011), pp. 25143–25150.

[76] S. Berg-Johansen et al. "Classically entangled optical beams for high-speed kinematic sensing". In: *Optica* 2.10 (2015), pp. 864–868.

[77] R. Wang et al. "Focused cylindrical vector beam assisted microscopic pSPR biosensor with an ultra wide dynamic range". In: *Optics Letters* 37.11 (2012), pp. 2091–2093.

[78] A. K. Dubey and V. Yadava. "Laser beam machining—a review". In: *International Journal of Machine Tools and Manufacture* 48.6 (2008), pp. 609–628.

[79] V. Niziev and A. Nesterov. "Influence of beam polarization on laser cutting efficiency". In: *Journal of Physics D: Applied Physics* 32.13 (1999), p. 1455.

[80] R. Weber et al. "Effects of radial and tangential polarization in laser material processing". In: *Physics Procedia* 12 (2011), pp. 21–30.

[81] W. S. Werner, K. Glantschnig, and C. Ambrosch-Draxl. "Optical constants and inelastic electron-scattering data for 17 elemental metals". In: *Journal of Physical and Chemical Reference Data* 38.4 (2009), pp. 1013–1092.

[82] D. Breitling et al. "Drilling of metals". In: *Femtosecond technology for technical and medical applications*. Springer, 2004, pp. 131–156.

[83] C. Föhl and F. Dausinger. "High precision deep drilling with ultrashort pulses". In: *Fourth International Symposium on Laser Precision Microfabrication*. Vol. 5063. International Society for Optics and Photonics. 2003, pp. 346–351.

[84] A Ancona et al. "High speed laser drilling of metals using a high repetition rate, high average power ultrafast fiber CPA system". In: *Optics Express* 16.12 (2008), pp. 8958–8968.

[85] M. A. Ahmed et al. "Radially polarized high-power lasers". In: *XVII International Symposium on Gas Flow, Chemical Lasers, and High-Power Lasers*. Vol. 7131. International Society for Optics and Photonics. 2009, p. 71311I.

[86] M. Meier, V. Romano, and T. Feurer. "Material processing with pulsed radially and azimuthally polarized laser radiation". In: *Applied Physics A* 86.3 (2007), pp. 329–334.

[87] S. Matsusaka, Y. Kozawa, and S. Sato. "Micro-hole drilling by tightly focused vector beams". In: *Optics Letters* 43.7 (2018), pp. 1542–1545.

[88] A. Ito, Y. Kozawa, and S. Sato. "Generation of hollow scalar and vector beams using a spot-defect mirror". In: *Journal of the Optical Society of America A* 27.9 (2010), pp. 2072–2077.

[89] S. Vyas, Y. Kozawa, and S. Sato. "Generation of a vector doughnut beam from an internal mirror He–Ne laser". In: *Optics Letters* 39.7 (2014), pp. 2080–2082.

[90] A. Hu et al. "Numerical investigation on the generation of high-order Laguerre–Gaussian beams in end-pumped solid-state lasers by introducing loss control". In: *Applied Optics* 53.33 (2014), pp. 7845–7853.

[91] D. Lin and W. Clarkson. "Polarization-dependent transverse mode selection in an Yb-doped fiber laser". In: *Optics Letters* 40.4 (2015), pp. 498–501.

[92] D. Naidoo, K. Aït-Ameur, and A. Forbes. "Intracavity vortex beam generation". In: *Laser Beam Shaping XII*. Vol. 8130. International Society for Optics and Photonics. 2011, p. 813009.

[93] Y. Chen, Y. Lan, and S. Wang. "Generation of Laguerre–Gaussian modes in fiber-coupled laser diode end-pumped lasers". In: *Applied Physics B* 72.2 (2001), pp. 167–170.

[94] J. Bisson, Y. Senatsky, and K.-I. Ueda. "Generation of Laguerre-Gaussian modes in Nd: YAG laser using diffractive optical pumping". In: *Laser Physics Letters* 2.7 (2005), p. 327.

[95] J. Kim and W. Clarkson. "Selective generation of Laguerre–Gaussian (LG0n) mode output in a diode-laser pumped Nd: YAG laser". In: *Optics Communications* 296 (2013), pp. 109–112.

[96] D. Kim and J. Kim. "High-power TEM 00 and Laguerre–Gaussian mode generation in double resonator configuration". In: *Applied Physics B* 121.3 (2015), pp. 401–405.

[97] I. A. Litvin et al. "Doughnut laser beam as an incoherent superposition of two petal beams". In: *Optics Letters* 39.3 (2014), pp. 704–707.

[98] D. Lin, J. Daniel, and W. Clarkson. "Controlling the handedness of directly excited Laguerre–Gaussian modes in a solid-state laser". In: *Optics Letters* 39.13 (2014), pp. 3903–3906.

[99] D. Kim and J. Kim. "Direct generation of an optical vortex beam in a single-frequency Nd: YVO 4 laser". In: *Optics Letters* 40.3 (2015), pp. 399–402.

[100] Q. Liu et al. "Integration of helicity-control and pulse-modulation for vortex laser based on a black phosphorus plate". In: *Optics Express* 24.26 (2016), pp. 30031–30037.

[101] N. Zhou, J. Liu, and J. Wang. "Reconfigurable and tunable twisted light laser". In: *Scientific Reports* 8.1 (2018), pp. 1–10.

[102] R. Uren et al. "Method for Generating High Purity Laguerre–Gaussian Vortex Modes". In: *IEEE Journal of Quantum Electronics* 55.5 (2019), pp. 1–9.

[103] M. Beijersbergen et al. "Helical-wavefront laser beams produced with a spiral phaseplate". In: *Optics Communications* 112.5-6 (1994), pp. 321–327.

[104] K. Sueda et al. "Laguerre-Gaussian beam generated with a multilevel spiral phase plate for high intensity laser pulses". In: *Optics Express* 12.15 (2004), pp. 3548–3553.

[105] W. Lee, X.-C. Yuan, and W. Cheong. "Optical vortex beam shaping by use of highly efficient irregular spiral phase plates for optical micromanipulation". In: *Optics Letters* 29.15 (2004), pp. 1796–1798.

[106] S. Oemrawsingh et al. "Production and characterization of spiral phase plates for optical wavelengths". In: *Applied Optics* 43.3 (2004), pp. 688–694.

[107] T. Watanabe et al. "Generation of a doughnut-shaped beam using a spiral phase plate". In: *Review of Scientific Instruments* 75.12 (2004), pp. 5131–5135.

[108] V. V. Kotlyar et al. "Generation of phase singularity through diffracting a plane or Gaussian beam by a spiral phase plate". In: *Journal of the Optical Society of America A* 22.5 (2005), pp. 849–861.

[109] W. Cheong et al. "Direct electron-beam writing of continuous spiral phase plates in negative resist with high power efficiency for optical manipulation". In: *Applied Physics Letters* 85.23 (2004), pp. 5784–5786.

[110] C. Jun et al. "Generation of optical vortex using a spiral phase plate fabricated in quartz by direct laser writing and inductively coupled plasma etching". In: *Chinese Physics Letters* 26.1 (2009), p. 014202.

[111] V Pramitha, A Vijayakumar, and S. Bhattacharya. "Fabrication of multilevel spiral phase plates by focused ion beam milling". In: *International Conference on Optics in Precision Engineering and Nanotechnology (icOPEN2013)*. Vol. 8769. International Society for Optics and Photonics. 2013, 87691S.

[112] H. Li et al. "Orbital angular momentum vertical-cavity surface-emitting lasers". In: *Optica* 2.6 (2015), pp. 547–552.

[113] P. Vayalamkuzhi et al. "Direct patterning of vortex generators on a fiber tip using a focused ion beam". In: *Optics Letters* 41.10 (2016), pp. 2133–2136.

[114] S. Pachava et al. "Generation and decomposition of scalar and vector modes carrying orbital angular momentum: a review". In: *Optical Engineering* 59.4 (2019), p. 041205.

[115] V. Y. Bazhenov, M. Vasnetsov, and M. Soskin. "Laser beams with screw dislocations in their wavefronts". In: *JETP Letters* 52.8 (1990), pp. 429–431.

[116] N. Heckenberg et al. "Generation of optical phase singularities by computer-generated holograms". In: *Optics Letters* 17.3 (1992), pp. 221–223.

[117] L. Janicijevic and S. Topuzoski. "Fresnel and Fraunhofer diffraction of a Gaussian laser beam by fork-shaped gratings". In: *Journal of the Optical Society of America A* 25.11 (2008), pp. 2659–2669.

[118] L. Yi-Dong, G. Chun-Qing, and G. Ming-Wei. "Study on holographic grating diffraction for Laguerre–Gaussian beam generation". In: *Chinese Physics B* 17.5 (2008), p. 1769.

[119] L. Stoyanov et al. "Far field diffraction of an optical vortex beam by a fork-shaped grating". In: *Optics Communications* 350 (2015), pp. 301–308.

[120] Z. Sacks, D Rozas, and G. Swartzlander. "Holographic formation of optical-vortex filaments". In: *Journal of the Optical Society of America B* 15.8 (1998), pp. 2226–2234.

[121] I. Sola et al. "High power vortex generation with volume phase holograms and non-linear experiments in gases". In: *Applied Physics B* 91.1 (2008), pp. 115–118.

[122] A. Y. Bekshaev et al. "Generation of optical vortex light beams by volume holograms with embedded phase singularity". In: *Optics Communications* 285.20 (2012), pp. 4005–4014.

[123] A. Jesacher et al. "Near-perfect hologram reconstruction with a spatial light modulator". In: *Optics Express* 16.4 (2008), pp. 2597–2603.

[124] A. Forbes, A. Dudley, and M. McLaren. "Creation and detection of optical modes with spatial light modulators". In: *Advances in Optics and Photonics* 8.2 (2016), pp. 200–227.

[125] Y.-X. Ren et al. "Experimental generation of Laguerre-Gaussian beam using digital micromirror device". In: *Applied Optics* 49.10 (2010), pp. 1838–1844.

[126] S. A. Goorden, J. Bertolotti, and A. P. Mosk. "Superpixel-based spatial amplitude and phase modulation using a digital micromirror device". In: *Optics Express* 22.15 (2014), pp. 17999–18009.

[127] R. Ismaeel et al. "All-fiber fused directional coupler for highly efficient spatial mode conversion". In: *Optics Express* 22.10 (2014), pp. 11610–11619.

[128] S Pidishety et al. "Orbital angular momentum beam excitation using an all-fiber weakly fused mode selective coupler". In: *Optics Letters* 42.21 (2017), pp. 4347–4350.

[129] J. Yang et al. "All-fiber multiplexing and transmission of high-order circularly polarized orbital angular momentum modes with mode selective couplers". In: *IEEE Photonics Journal* 11.3 (2019), pp. 1–9.

[130] X. Heng et al. "All-fiber stable orbital angular momentum beam generation and propagation". In: *Optics Express* 26.13 (2018), pp. 17429–17436.

[131] R. C. Devlin et al. "Arbitrary spin-to–orbital angular momentum conversion of light". In: *Science* 358.6365 (2017), pp. 896–901.

[132] H. Ren et al. "Metasurface orbital angular momentum holography". In: *Nature Communications* 10.1 (2019), pp. 1–8.

[133] T. Hou et al. "Deep-learning-assisted, two-stage phase control method for high-power mode-programmable orbital angular momentum beam generation". In: *Photonics Research* 8.5 (2020), pp. 715–722.

[134] D. Pohl. "Operation of a ruby laser in the purely transverse electric mode TE01". In: *Applied Physics Letters* 20.7 (1972), pp. 266–267.

[135] K. Yonezawa, Y. Kozawa, and S. Sato. "Generation of a radially polarized laser beam by use of the birefringence of a c-cut Nd:YVO4 crystal". In: *Optics Letters* 31.14 (2006), pp. 2151–2153.

[136] K. Yonezawa, Y. Kozawa, and S. Sato. "Compact laser with radial polarization using birefringent laser medium". In: *Japanese Journal of Applied Physics* 46.8R (2007), p. 5160.

[137] G. Machavariani et al. "Birefringence-induced bifocusing for selection of radially or azimuthally polarized laser modes". In: *Applied Optics* 46.16 (2007), pp. 3304–3310. DOI: 10.1364/AO.46.003304. URL: http://ao.osa.org/abstract.cfm?URI=ao-46-16-3304.

[138]   J.-F. Bisson et al. "Radially polarized ring and arc beams of a neodymium laser with an intra-cavity axicon". In: *Optics Express* 14.8 (2006), pp. 3304–3311.

[139]   Y. Kozawa and S. Sato. "Generation of a radially polarized laser beam by use of a conical Brewster prism". In: *Optics Letters* 30.22 (2005), pp. 3063–3065.

[140]   T Erdogan et al. "Circularly symmetric operation of a concentric-circle-grating, surface-emitting, AlGaAs/GaAs quantum-well semiconductor laser". In: *Applied Physics Letters* 60.16 (1992), pp. 1921–1923.

[141]   M. A. Ahmed et al. "Multilayer polarizing grating mirror used for the generation of radial polarization in Yb:YAG thin-disk lasers". In: *Optics Letters* 32.22 (2007), pp. 3272–3274.

[142]   M. Rumpel et al. "Circular grating waveguide structures for intracavity generation of azimuthal polarization in a thin-disk laser". In: *Optics Letters* 37.10 (2012), pp. 1763–1765.

[143]   M. A. Ahmed et al. "Radially polarized 3kW beam from a CO2 laser with an intracavity resonant grating mirror". In: *Optics Letters* 32.13 (2007), pp. 1824–1826.

[144]   T. Dietrich et al. "Thin-disk oscillator delivering radially polarized beams with up to 980 W of CW output power". In: *Optics Letters* 43.6 (2018), pp. 1371–1374.

[145]   F. Beirow et al. "Radially polarized passively mode-locked thin-disk laser oscillator emitting sub-picosecond pulses with an average output power exceeding the 100 W level". In: *Optics Express* 26.4 (2018), pp. 4401–4410.

[146]   Q. Zhan and J. R. Leger. "Microellipsometer with radial symmetry". In: *Applied Optics* 41.22 (2002), pp. 4630–4637.

[147]   Q. Zhan and J. R. Leger. "Interferometric measurement of the geometric phase in space-variant polarization manipulations". In: *Optics Communications* 213.4-6 (2002), pp. 241–245.

[148]   S. C. Tidwell, D. H. Ford, and W. D. Kimura. "Generating radially polarized beams interferometrically". In: *Applied Optics* 29.15 (1990), pp. 2234–2239.

[149]   N. Passilly et al. "Simple interferometric technique for generation of a radially polarized light beam". In: *Journal of the Optical Society of America A* 22.5 (2005), pp. 984–991.

[150]   V. Niziev, R. Chang, and A. Nesterov. "Generation of inhomogeneously polarized laser beams by use of a Sagnac interferometer". In: *Applied Optics* 45.33 (2006), pp. 8393–8399.

[151]   R. Yamaguchi, T. Nose, and S. Sato. "Liquid crystal polarizers with axially symmetrical properties". In: *Japanese Journal of Applied Physics* 28.9R (1989), p. 1730.

[152] M Stalder and M Schadt. "Linearly polarized light with axial symmetry generated by liquid-crystal polarization converters". In: *Optics Letters* 21.23 (1996), pp. 1948–1950.

[153] S. C. McEldowney, D. M. Shemo, and R. A. Chipman. "Vortex retarders produced from photo-aligned liquid crystal polymers". In: *Optics Express* 16.10 (2008), pp. 7295–7308.

[154] Z. Bomzon, V. Kleiner, and E. Hasman. "Formation of radially and azimuthally polarized light using space-variant subwavelength metal stripe gratings". In: *Applied Physics Letters* 79.11 (2001), pp. 1587–1589.

[155] G Machavariani et al. "Spatially-variable retardation plate for efficient generation of radially-and azimuthally-polarized beams". In: *Optics Communications* 281.4 (2008), pp. 732–738.

[156] A. K. Spilman and T. G. Brown. "Stress birefringent, space-variant wave plates for vortex illumination". In: *Applied Optics* 46.1 (2007), pp. 61–66.

[157] M. Beresna, M. Gecevičius, and P. G. Kazansky. "Polarization sensitive elements fabricated by femtosecond laser nanostructuring of glass". In: *Optical Materials Express* 1.4 (2011), pp. 783–795.

[158] M. Beresna et al. "Radially polarized optical vortex converter created by femtosecond laser nanostructuring of glass". In: *Applied Physics Letters* 98.20 (2011), p. 201101.

[159] D. Lin et al. "Cladding-pumped ytterbium-doped fiber laser with radially polarized output". In: *Optics Letters* 39.18 (2014), pp. 5359–5361.

[160] N. Baktash, S.-u. Alam, D. J. Richardson, et al. "106 W, picosecond Yb-doped fiber MOPA system with a radially polarized output beam". In: *Optics Letters* 43.20 (2018), pp. 4957–4960.

[161] A. Arbabi et al. "Dielectric metasurfaces for complete control of phase and polarization with subwavelength spatial resolution and high transmission". In: *Nature Nanotechnology* 10.11 (2015), pp. 937–943.

[162] F. Yue et al. "Vector vortex beam generation with a single plasmonic metasurface". In: *ACS Photonics* 3.9 (2016), pp. 1558–1563.

[163] T Grosjean, D Courjon, and M Spajer. "An all-fiber device for generating radially and other polarized light beams". In: *Optics Communications* 203.1-2 (2002), pp. 1–5.

[164] G. Volpe and D Petrov. "Generation of cylindrical vector beams with few-mode fibers excited by Laguerre–Gaussian beams". In: *Optics Communications* 237.1-3 (2004), pp. 89–95.

[165] T. Hirayama et al. "Generation of a cylindrically symmetric, polarized laser beam with narrow linewidth and fine tunability". In: *Optics Express* 14.26 (2006), pp. 12839–12845.

[166]   B. Sun et al. "Low-threshold single-wavelength all-fiber laser generating cylin-drical vector beams using a few-mode fiber Bragg grating". In: *Optics Letters* 37.4 (2012), pp. 464–466.

[167]   J Lin et al. "Tungsten disulphide based all fiber Q-switching cylindrical-vector beam generation". In: *Applied Physics Letters* 107.19 (2015), p. 191108.

[168]   A Leblanc et al. "Plasma holograms for ultrahigh-intensity optics". In: *Nature Physics* 13.5 (2017), pp. 440–443.

[169]   A Denoeud et al. "Interaction of ultraintense laser vortices with plasma mir-rors". In: *Physical Review Letters* 118.3 (2017), p. 033902.

[170]   A. Longman et al. "Off-axis spiral phase mirrors for generating high-intensity optical vortices". In: *Optics Letters* 45.8 (2020), pp. 2187–2190.

[171]   I. Moshe, S. Jackel, and A. Meir. "Production of radially or azimuthally po-larized beams in solid-state lasers and the elimination of thermally induced birefringence effects". In: *Optics Letters* 28.10 (2003), pp. 807–809.

[172]   C. Smith et al. "Amplification of a radially polarised beam in an Yb: YAG thin-slab". In: *Applied Physics B* 123.8 (2017), p. 225.

[173]   M. Fridman et al. "Fiber amplification of radially and azimuthally polarized laser light". In: *Optics Letters* 35.9 (2010), pp. 1332–1334.

[174]   M. A. Ahmed et al. "High-power radially polarized Yb: YAG thin-disk laser with high efficiency". In: *Optics Express* 19.6 (2011), pp. 5093–5103.

[175]   B. Trabold et al. "Amplification of higher-order modes by stimulated Raman scattering in H 2-filled hollow-core photonic crystal fiber". In: *Optics Letters* 38.5 (2013), pp. 600–602.

[176]   F. Beirow et al. "Amplification of radially polarized ultra-short pulsed radia-tion to average output powers exceeding 250 W in a compact single-stage Yb: YAG single-crystal fiber amplifier". In: *Applied Physics B* 126.9 (2020), pp. 1–10.

[177]   W. Clarkson and D. Hanna. "Effects of Transverse-mode Profile on Slope Ef-ficiency and Relaxation Oscillations in a Longitudinally-pumped Laser". In: *Journal of Modern Optics* 36.4 (1989), pp. 483–498. DOI: 10.1080/09500348914550561. eprint: https://doi.org/10.1080/09500348914550561. URL: https://doi.org/10.1080/09500348914550561.

[178]   J. Kim and W. Clarkson. "Selective generation of Laguerre–Gaussian (LG0n) mode output in a diode-laser pumped Nd:YAG laser". In: *Optics Communi-cations* 296 (2013), pp. 109 –112. ISSN: 0030-4018. DOI: https://doi.org/10.1016/j.optcom.2013.01.046. URL: http://www.sciencedirect.com/science/article/pii/S0030401813001284.

[179] R. L. Phillips and L. C. Andrews. "Spot size and divergence for Laguerre Gaussian beams of any order". In: *Applied Optics* 22.5 (1983), pp. 643–644. DOI: `10.1364/AO.22.000643`. URL: `http://ao.osa.org/abstract.cfm?URI=ao-22-5-643`.

[180] J. W. Kim et al. "High power Er:YAG laser with radially-polarized Laguerre-Gaussian (LG01) mode output". In: *Opics Express* 19.15 (2011), pp. 14526–14531. DOI: `10.1364/OE.19.014526`. URL: `http://www.opticsexpress.org/abstract.cfm?URI=oe-19-15-14526`.

[181] D. J. Kim et al. "Influence of a ring-shaped pump beam on temperature distribution and thermal lensing in end-pumped solid state lasers". In: *Optics Express* 25.13 (2017), pp. 14668–14675. DOI: `10.1364/OE.25.014668`. URL: `http://www.opticsexpress.org/abstract.cfm?URI=oe-25-13-14668`.

[182] L. Cini and J. Mackenzie. "Analytical thermal model for end-pumped solid-state lasers". In: *Applied Physics B* 123.12 (2017), p. 273.

[183] *ISO 11146-1:2005 Lasers and laser-related equipment — Test methods for laser beam widths, divergence angles and beam propagation ratios — Part 1: Stigmatic and simple astigmatic beams*. International Organization for Standardization. 2005.

[184] R. Uren. "Developments in the generation and measurement of vortex modes in solid-state lasers". PhD thesis. University of Southampton, 2019. URL: `https://eprints.soton.ac.uk/437582/`.

[185] A. A. Malyutin and V. Ilyukhin. "Generation of high-order Hermite–Gaussian modes in a flashlamp-pumped neodymium phosphate glass laser and their conversion to Laguerre–Gaussian modes". In: *Quantum Electronics* 37.2 (2007), p. 181.

[186] T. Ohtomo, S.-C. Chu, and K. Otsuka. "Generation of vortex beams from lasers with controlled Hermite-and Ince-Gaussian modes". In: *Optics Express* 16.7 (2008), pp. 5082–5094.

[187] S.-C. Chu and K. Otsuka. "Doughnut-like beam generation of Laguerre–Gaussian mode with extremely high mode purity". In: *Optics Communications* 281.6 (2008), pp. 1647–1653.

[188] Q. Liu et al. "Efficient generation of nanosecond LG01 mode pulses with high purity". In: *The 8th EPS-QEOD Europhoton Conference on Solid-State, Fibre and Coherent Light Sources*. 2018.

[189] J. Simmons and K. Kirkham. *White Paper - ISO compliance of non-contact, real-time beam analysis*. Tech. rep. Ophir, Apr. 2019.

[190] Y.-a. Yu et al. "Real-time laser beam quality measurement technique". In: *Chinese Journal of Lasers* 34.2 (2007), p. 255.

[191]   Ophir. *BeamSquared® Beam Propagation Analyzer*. 2020. URL: https://www.ophiropt.com/laser--measurement/beam-profilers/products/M2-Beam-Propagation-Analysis/BeamSquared (visited on 06/04/2020).

[192]   L. Huang et al. "Adaptive mode control of a few-mode fiber by real-time mode decomposition". In: *Optics Express* 23.21 (2015), pp. 28082–28090. DOI: 10.1364/OE.23.028082. URL: http://www.opticsexpress.org/abstract.cfm?URI=oe-23-21-28082.

[193]   T. Qiu et al. "Adaptive Mode Control in 4- and 17-Mode Fibers". In: *IEEE Photonics Technology Letters* 30.11 (2018), pp. 1036–1039.

[194]   C. Jollivet et al. "Mode-resolved gain analysis and lasing in multi-supermode multi-core fiber laser". In: *Optics Express* 22.24 (2014), pp. 30377–30386. DOI: 10.1364/OE.22.030377. URL: http://www.opticsexpress.org/abstract.cfm?URI=oe-22-24-30377.

[195]   L. Huang et al. "Modal Analysis of Fiber Laser Beam by Using Stochastic Parallel Gradient Descent Algorithm". In: *IEEE Photonics Technology Letters* 27.21 (2015), pp. 2280–2283.

[196]   C. Schulze et al. "Mode resolved bend loss in few-mode optical fibers". In: *Optics Express* 21.3 (2013), pp. 3170–3181. DOI: 10.1364/OE.21.003170. URL: http://www.opticsexpress.org/abstract.cfm?URI=oe-21-3-3170.

[197]   D. Flamm et al. "Modal characterization of fiber-to-fiber coupling processes". In: *Optics Letters* 38.12 (2013), pp. 2128–2130. DOI: 10.1364/OL.38.002128. URL: http://ol.osa.org/abstract.cfm?URI=ol-38-12-2128.

[198]   L. Huang et al. "Mode instability dynamics in high-power low-numerical-aperture step-index fiber amplifier". In: *Applied Optics* 56.19 (2017), pp. 5412–5417. DOI: 10.1364/AO.56.005412. URL: http://ao.osa.org/abstract.cfm?URI=ao-56-19-5412.

[199]   F. Stutzki et al. "High-speed modal decomposition of mode instabilities in high-power fiber lasers". In: *Optics Letters* 36.23 (2011), pp. 4572–4574. DOI: 10.1364/OL.36.004572. URL: http://ol.osa.org/abstract.cfm?URI=ol-36-23-4572.

[200]   J. W. Nicholson et al. "Spatially and spectrally resolved imaging of modal content in large-mode-area fibers". In: *Optics Express* 16.10 (2008), pp. 7233–7243. DOI: 10.1364/OE.16.007233. URL: http://www.opticsexpress.org/abstract.cfm?URI=oe-16-10-7233.

[201]   J. Demas and S. Ramachandran. "Sub-second mode measurement of fibers using C2 imaging". In: *Optics Express* 22.19 (2014), pp. 23043–23056. DOI: 10.1364/OE.22.023043. URL: http://www.opticsexpress.org/abstract.cfm?URI=oe-22-19-23043.

[202] N Andermahr, T Theeg, and C Fallnich. "Novel approach for polarization-sensitive measurements of transverse modes in few-mode optical fibers". In: *Applied Physics B* 91.2 (2008), p. 353.

[203] Y. Ma et al. "Fiber-modes and fiber-anisotropy characterization using low-coherence interferometry". In: *Applied Physics B* 96.2-3 (2009), pp. 345–353.

[204] T. Kaiser et al. "Complete modal decomposition for optical fibers using CGH-based correlation filters". In: *Optics Express* 17.11 (2009), pp. 9347–9356.

[205] M. Lyu et al. "Fast modal decomposition for optical fibers using digital holography". In: *Scientific Reports* 7.1 (2017), pp. 1–9.

[206] R. Brüning et al. "Comparative analysis of numerical methods for the mode analysis of laser beams". In: *Applied Optics* 52.32 (2013), pp. 7769–7777.

[207] R. W. Gerchberg. "A practical algorithm for the determination of phase from image and diffraction plane pictures". In: *Optik* 35 (1972), pp. 237–246.

[208] O. Shapira et al. "Complete modal decomposition for optical waveguides". In: *Physical Review Letters* 94.14 (2005), p. 143902.

[209] L. Li et al. "Multimode fiber modal decomposition based on hybrid genetic global optimization algorithm". In: *Optics Express* 25.17 (2017), pp. 19680–19690.

[210] L. Huang et al. "Real-time mode decomposition for few-mode fiber based on numerical method". In: *Optics Express* 23.4 (2015), pp. 4620–4629.

[211] A. Krizhevsky, I. Sutskever, and G. E. Hinton. "Imagenet classification with deep convolutional neural networks". In: *Advances in neural information processing systems*. 2012, pp. 1097–1105.

[212] T. Baumeister, S. L. Brunton, and J. N. Kutz. "Deep learning and model predictive control for self-tuning mode-locked lasers". In: *Journal of the Optical Society of America B* 35.3 (2018), pp. 617–626. DOI: 10.1364/JOSAB.35.000617. URL: http://josab.osa.org/abstract.cfm?URI=josab-35-3-617.

[213] A. Sinha et al. "Lensless computational imaging through deep learning". In: *Optica* 4.9 (2017), pp. 1117–1125. DOI: 10.1364/OPTICA.4.001117. URL: http://www.osapublishing.org/optica/abstract.cfm?URI=optica-4-9-1117.

[214] B. Rahmani et al. "Multimode optical fiber transmission with a deep learning network". In: *Light: Science & Applications* 7.1 (2018), pp. 1–11.

[215] Y. Rivenson et al. "Deep learning microscopy". In: *Optica* 4.11 (2017), pp. 1437–1443. DOI: 10.1364/OPTICA.4.001437. URL: http://www.osapublishing.org/optica/abstract.cfm?URI=optica-4-11-1437.

[216] H. Tünnermann and A. Shirakawa. "Deep reinforcement learning for coherent beam combining applications". In: *Optics Express* 27.17 (2019), pp. 24223–24230. DOI: 10.1364/OE.27.024223. URL: http://www.opticsexpress.org/abstract.cfm?URI=oe-27-17-24223.

[217]   A. Liu et al. "Analyzing modal power in multi-mode waveguide via machine learning". In: *Optics express* 26.17 (2018), pp. 22100–22109.

[218]   Y. An et al. "Learning to decompose the modes in few-mode fibers with deep convolutional neural network". In: *Optics express* 27.7 (2019), pp. 10127–10137.

[219]   T. L. Jefferson-Brain et al. "Alignment of Higher-Order Mode Solid-State Laser Systems with Machine Learning Diagnostic Assistance". In: *2019 Conference on Lasers and Electro-Optics Europe and European Quantum Electronics Conference*. Optical Society of America, 2019, CAp48. URL: http://www.osapublishing.org/abstract.cfm?URI=CLEO_Europe-2019-ca_p_48.

[220]   K. Simonyan and A. Zisserman. "Very deep convolutional networks for large-scale image recognition". In: *arXiv preprint arXiv:1409.1556* (2014).

[221]   A. E. Siegman and S. W. Townsend. "Output beam propagation and beam quality from a multimode stable-cavity laser". In: *IEEE Journal of Quantum Electronics* 29.4 (1993), pp. 1212–1217.

[222]   D. P. Kingma and J. Ba. "Adam: A method for stochastic optimization". In: *arXiv preprint arXiv:1412.6980* (2014).

[223]   P. Shardlow et al. "Hybrid Ho: YAG laser with 50W radially-polarised output". In: *The European Conference on Lasers and Electro-Optics*. Optical Society of America. 2019, ca_1_2.

[224]   M. Sakakura et al. "Ultralow-loss geometric phase and polarization shaping by ultrafast laser writing in silica glass". In: *Light: Science & Applications* 9.1 (2020), pp. 1–10.

[225]   G. R. Sims, F. Griffin, and M. P. Lesser. "Silicon CCD optimized for near infrared (NIR) wavelengths". In: *New Methods in Microscopy and Low Light Imaging*. Vol. 1161. International Society for Optics and Photonics. 1989, pp. 55–60.

[226]   L.-Q. Meng et al. "Suppressing the influence of charge-coupled device vertical blooming on the measurement of laser beam quality factor (M2) of a near-infrared laser". In: *Applied Optics* 57.2 (2018), pp. 130–137. DOI: 10.1364/AO.57.000130. URL: http://ao.osa.org/abstract.cfm?URI=ao-57-2-130.

[227]   D Findlay and R. Clay. "The measurement of internal losses in 4-level lasers". In: *Physics Letters* 20 (1966), pp. 277–278.

[228]   W. W. Rigrod. "Saturation effects in high-gain lasers". In: *Journal of Applied Physics* 36.8 (1965), pp. 2487–2490.

[229]   C. R. Smith et al. "Thermally guided Yb-doped fiber-rod amplifier and laser". In: *Applied Physics B* 125.2 (2019), p. 32.

[230]   C. R. Smith. "Power Scaling Architectures for Solid-State and Fiber Lasers". PhD thesis. University of Southampton, 2017.

[231] D. C. Brown and H. J. Hoffman. "Thermal, stress, and thermo-optic effects in high average power double-clad silica fiber lasers". In: *IEEE Journal of quantum electronics* 37.2 (2001), pp. 207–217.

[232] T Toyoda and M Yabe. "The temperature dependence of the refractive indices of fused silica and crystal quartz". In: *Journal of Physics D: Applied Physics* 16.5 (1983), p. L97.

[233] *The Necronomicon*.

[234] R Paschotta. *Fiber Amplifiers: More ASE for Larger Core with Higher NA?* 2007. URL: https://www.rp-photonics.com/spotlight_2007_08_06.html (visited on 09/08/2020).